Gallium Arsenide Based Metal-Semiconductor-Metal Devices and Detectors

A Thesis

Submitted to the Faculty

of

Drexel University

by

Eric Michael Gallo

in partial fulfillment of the

requirements for the degree

of

Doctor of Philosophy in Electrical and Computer Engineering

September 2010

Dedications

I would like to dedicated this work to Gavin, Riley, Ethan, Greg and Jesjka for inspiring me to continue to strive to be someone to look up to.

Acknowledgments

This work would not have been possible without the generous support of my advisor Dr. Jonathan Spanier. His patience with me has been infinite and his ability to help get to the root of research problems has been invaluable. I would also like to thank Dr. Bahram Nabet for his advising and guidance early in graduate career and for presenting me with the opportunity to learn and pursue many different aspects of device physics.

Much of the work presented is the result of long standing collaborations with several researchers. I would like to acknowledge Adriano Cola and Fabio Quaranta for fabrication and measurements on the 2DEHG devices, Marc Currie of NRL for high speed optical characterization measurements, Nico Lovergine, Paula Prete and the rest of their lab for growth of the GaAs nanowire structures.

I would like to acknowledge those who contributed to this work at Drexel including my labmates: Dr. Xia Zhao and Dr. Xiying Chen both of whom contributed heavily to the work presented and were strong mentors to me as a young graduate student. I would like to thank Sean Chen for his tireless hours of work on the nanowire devices along with his tireless hours of discussion with me on the results and the philosophy of science. I would also like to thank my other labmates for their contributions in device fabrication and characterization: Oren Leaffer, Terrence McGuckin, Stephanie Johnson, Brian Beatty, Mike Coster, Jennifer Atchison, Joan Burger, Rob Crow, Ron Martin, Sourav Das, Lee Laim, Linyou Cao, Zakiya Carter, Bora Garipcan and Stephen Nonnenmann.

I would also like to acknowledge Yale Goldman, Joseph Forkey, Moshe Kam, Allen Rothwarf, Tim Kurzweg, Eli Fromm, Robert Quinn, Kevin Scoles, Roberto Cingolani, Alan MacDiarmid, Charlie Johnson and Ed Gerber for mentoring me during my years as a graduate student. Their guidance and encouragement has helped me grow not

only as a researcher but also as a member of the academic community.

Most importantly I would like to acknowledge the support of my family and friends, who maintained constant faith that I would finish even when I didn't believe it myself. Thanks to my mother, Diane Gallo and my father, Frank Gallo for being incredibly supportive in my work and life. To my grandparents, Charles and Doris Makinson and Jean Gallo, for convincing me I was destined for great things. And to the rest of my family: Marj, Alana, Justin, Jon, Matt, Dave, Nick, Gavin, Ethan, Riley, Gregory, Jesjka, Baby, Maya and Harley for believing in me and loving me unconditionally. I would also like to thank the Mullay Family: Kim, Nick, Carol, Vince and Steve for their support and inspiration. You are my hero Steve and continue to be an inspiration in all parts of my life.

I would like to thank Linda Keglovits, Nancy Fritz and Glen Wallingford for instilling within me the confidence to pursue higher education. Their words and guidance still motivate me almost 20 years later.

The path to a PhD has been a long and treacherous one for me and I could not have made it without the support of Simone Allender, who has been an amazing mentor and friend through the entire journey. Leah D'Agostino, Courtney McCarron and Kimberly Shannon have been and continue to be amazing and tolerant friends and insisting on taking care of me even when I don't believe I need it. I would also like to specifically thank: Adam O'Donnell, Michelle Sipics, Charlotte Lee, Denise McKellick, Marybeth Chew, Nicole VanNortwich for their unending support.

I owe a debt of thanks to all of the individuals who kept life fun and interesting in Philadelphia: Adam Mancini, Jula Nawrocki, Bryan Allen, Eric Cronin, Carrieann Nielsen, Sean Fenton, Makaria Tsapatoris, Jason Haraldsen, Jenny Corbin, Jestis Deuerlein, Johna Winters, Joe McCleery, Rayna Bondy, Nick Kirsch, Margot Quinlan, Gudrun Lubbe, Sue Oleykowski, Andrew Burnheimer, Markos Kapes, Shannon

Quinn, Shakey Lyman, Rich Mulhearn, Danno, Jon Eskow, Kristin Hanson, Decker, Mitch, Patti, Sky, Dawn, Stirling, Sienna, Elena, Ben, Aaron Henry, Monique Harris, Erika Hubbard, Nikoia Greene and everyone else that has made my life in Philadelphia one to brag about. I would also like to add a special thank you to Doobies and Intermezzo.

Last but not least, thank you to Andy and Henry for giving me that final push and helping me see everything there was to look forward to afterward.

My career as a graduate student was supported by the National Foundation Graduate Student Fellowship, The Koerner Family Fellowship, The NSF GK-12 Graduate Fellowship and the Simone Allender Student Housing Fellowship. The nanowire work was supported by NSF-ECCS-0702716 and NSF-DMR-0722845 as well as US Army Research Office under the DURIP program in the form of instrumentation

Table of Contents

List of Tables

List of Figures

Abstract

Gallium Arsenide Based Metal-Semiconductor-Metal Devices and Detectors

Eric Michael Gallo

Advisor: Jonathan Spanier, Ph.D.

Each year the creation and refinement of new material growth techniques give rise to novel material systems for electronic device exploration. A metal-semiconductor-metal (MSM) device is the simplest electronic device possible, consisting of two metal contacts on a semiconducting channel. Despite their simplicity, these devices can operate as high performance detectors as well as enable rapid characterization of novel electronic materials. This thesis will discuss the fabrication and characterization of MSM devices on a two-dimensional electron hole gas (2DEHG) and GaAs-based nanowires. 2DEHG structures consist of two spatial separated quantum wells of opposite charge. These devices exhibit a high-speed photo-response, a two plateau varactor response and give rise to several unexplained photoluminescence peaks. GaAs-based nanowire MSMs offer the opportunity to fabricate many of the well known bulk III-V semiconductor devices on the nanoscale. Accomplishing this requires quality ohmic contacts. Several fabrication methods to create ohmic contacts on GaAs nanowires are described, as well as characterization of the light response of these devices and results demonstrating ambipolar transport in a wide bandgap material. The devices offer promise as high speed on-chip interconnects for digital circuits.

1. Gallium Arsenide Based Electron Devices

The advent of nanotechnology has created many new and exciting avenues to design and fabricate semiconducting based devices that offer the opportunity to not only improve upon those fabricated in bulk materials but to enable new functionalities and technologies not accessible in planar and bulk materials. In this context several routes present themselves as paths to exploring and seeking out these new possible devices.

A large research effort has been put towards the investigation of new and non-traditional material systems. The most significant of these platforms being carbon nanotubes and graphene. These systems have shown promise in a wide range of device applications and have also served as a nano-scale test bed for many new and exciting physics not possible in bulk systems [1; 2; 3; 4; 5].

Significant energy has also gone into other novel materials such as polymers and oxides [6; 7; 8; 9]. New fabrication and measurement techniques have opened up applications for these materials that were traditionally reserved for silicon and other 'standard' semiconductors [10; 11; 12]. These materials have also opened up functionalities that have typically not been available to semiconductor devices [13; 14; 15].

1.1 GaAs-Based Nanostructures

Precise growth techniques have also allowed the possibility of nano-structured devices in semiconductors [16]. In fact some of the earliest and most accessible nano-scaled devices could be found at the interfaces between different semiconductors grown with atomic precision [17]. The formation of quantum wells, where charge carriers are confined within the material to regions on the nanometer scale, allowed not

only the exploration of interesting physics such as quantum hall effect, but also the creation of devices with superior performance over existing technologies [18]. High electron mobility transistors, fabricated using semiconducting heterostructures containing quantum wells, continue to be hold the benchmark for high speed transistor operation [19; 20; 21]. The same devices, with the advent of nanoscale electrode fabrication, have also shown to be excellent detectors of a wide array of stimuli [22; 23; 24; 25; 26; 27; 28; 29; 30; 31; 32; 33]. These devices have most recently been shown as potential detectors of terahertz radiation, a difficult to access but very useful portion of the electro-magnetic spectrum. The small energy of terahertz photons (less than thermal energy at room temperature) makes them difficult to detect using absorption, as is done with higher energy infrared radiation, while the high speed makes antenna based detection inaccessible as well. The large concentration and confinement of the carriers at the interface allows this radiation to be detected using the properties of the plasmon that is created within it [28].

These new functionalities encourage the exploration and characterization of new systems at the nanoscale. Using traditional semiconductors such as Si, Ge and GaAs allows the designer to pull from an existing toolbox of well established fabrication techniques that can now be applied to these nanoscale systems. Initially this allows traditional devices such as diodes and transistors to be simply shrunk in size, to make improvements by reducing carrier transit times and power consumption. However, novel structures also allow these same materials to be fabricated in such a way that new functionalities can be discovered and further improvements can be made that may not be accessible in bulk devices.

The work discussed here will be on fabricating and characterizing devices on two new GaAs material systems. The initial motivation behind the design was the improvement of existing GaAs based photodetectors. GaAs is chosen due to its band

gap that falls in the range for fiber optic communication, as well as its bulk electrical properties such as high electron mobility. With these benefits however come several known tradeoffs. GaAs is often plagued by surface states and Fermi level pinning, a trait that poses a considerable problem for operation of nano-scale devices. As the surface to volume ratio is increased, surface effects can be amplified and even become dominant in devices. The high electron mobility also comes with an order of magnitude smaller hole mobility. For optical detection, which necessarily involves electrons and holes due to the formation of electron-hole pairs, this small hole mobility can present the limiting factor in the time response of these devices.

1.2 Quantum well based material system

The first material system presented is an attempt to deal with the problem of low hole mobility by creating a detector incorporating both an electron and hole quantum well to improve the mobility and collection of holes generated by incident radiation. In this design, along with improving upon single well detectors, several other interesting qualities were uncovered including a capacitance voltage relationship not seen in existing devices and photoluminescence peaks that suggest a complex internal potential landscape. The structure also promises improved diffusion due to charge separation created by the large electric field between the wells and high mobility channels for both carriers. These properties are uncovered in a sequence of measurements on two terminal Schottky contacted devices.

1.3 Nanowire based material system

The second material system is GaAs-based nanowires. These devices, as has been shown in a wide variety of other nanowire devices, offer possibilities for improvement not only to optical detection but to other devices as well. GaAs-based optical

detectors are strong candidates for a much sought after device, on-chip optical interconnects. They also present the possibility for use as chemical/particle detectors, ambipolar transistors and possibly high speed optical detectors.

To initially investigate the properties of these devices, a metal-semiconductor-metal configuration is used. This device design presents a simple but useful platform to explore issues related to fabrication optimization and to initial characterization of the material. The devices are often used as the first step in fabricating complex, high performance devices using new material systems. The configuration also has many uses in a final form, particularly for light detection where metal-semiconductor-metal based detectors are often used commercially for high performance devices and ease of fabrication and integration. For that reason, they were the basis for all devices fabricated for this work.

1.4 Objective and Scope of the Dissertation

This dissertation will discuss metal-semiconductor-metal (MSM) structures on GaAs-based material systems in the planar geometry and nanowire geometry. The goal is to demonstrate the possible functionality of each system for use as an MSM detection device, primarily as optical detectors. Chapter 2 will introduce the basics of MSM operation. Chapters 3 will detail measurements on a dual quantum well structure, with an electron and hole well separated by 110nm. This structure presents several interesting behaviors and the possibility to serve as the basis for a high-speed photodetector as well as several other potential devices. Results from the DC and AC electrical characterization will be presented, comparing the material to other systems and examining the effects of a built in Bragg reflector on the devices. Results from high speed optical testing will be presented, including a comparison to previous reported results from similar structures. Photoluminescence measurements will also be

discussed, revealing many interesting features not seen in other heterostructure systems. The photoluminescence results serve to further characterize the material system and reveal additional interesting behaviors arising from the presence of the dual well structure. Chapters 4 will discuss GaAs nanowire based devices. The discussion here will center on fabrication and characterization of different device designs. The first fabricated ohmic contacts to undoped wires will be reported, as well as contacts to core-shell wire configurations. The surface effects of the devices will be investigated including the effects of sulfur passivation. Photoresponse will also be detailed with the core-shell devices exhibiting strong promise as photodetectors. Observed ambipolar transport within the wires when gated with high κ dielectric will also be detailed.

2. Metal-Semiconductor-Metal Devices

2.1 Metal-Semiconductor-Metal Structure

New semiconducting materials and structures are emerging each year with new growth techniques and discoveries concerning the properties of interfaces of particular materials. In order to characterize these new materials for use in practical electronics they must be fabricated into operational devices that allow for the evaluation of their functionality and electrical properties. The simplest form of a semiconducting device is a metal-semiconductor-metal (MSM) structure. The device consists of two contacts on a semiconducting channel that allow a variety of electrical and optical characterizations to be carried out. This device configuration allows for quick and, possibly, simple characterization of bulk and nanostructured semiconducting materials and is an often-used design for detectors of electromagnetic radiation at various frequencies.

An MSM is a simple device consisting of two metal contacts on a piece of semiconducting material, typically with two back-to-back Schottky contacts. In this work however, we will use a more literal definition and include all contact types such as ohmic, blocking (Schottky) and all those that fall between. The simple criteria is that no external doping methods are used other than metal deposition and annealing.

2.2 MSM Band Diagram

An examination of the simple band structure typically discussed for MSM structures shows two Schottky contacts on either side of a semiconducting channel. The contacts can be symmetrical or asymmetrical depending on the fabrication process or the semiconducting material itself. A simple band diagram is shown in The Schottky contacts create a barrier to carriers moving through the interface. This barrier can

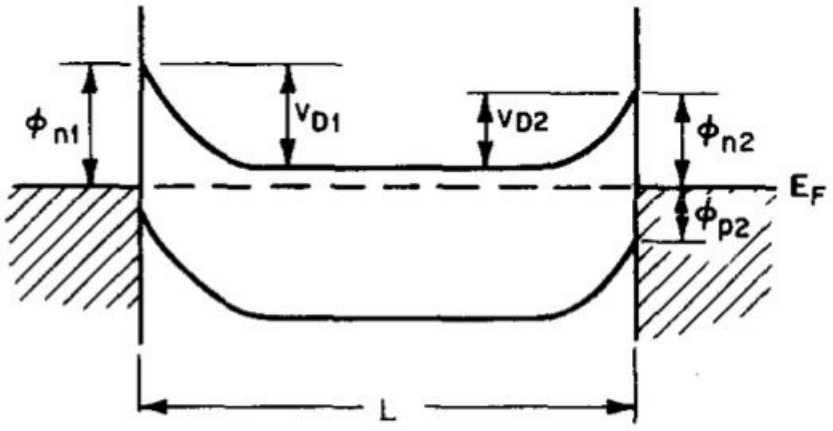

Figure 2.1: Energy band diagram of a Schottky contacted metal-semiconductor-metal device, denoting the barrier heights and built in voltages at each contact [Reprinted from Solid State Electronics, Vol. 14, S.M.Sze et.al. "Current transport in metal-semiconducting-metal structures",1971, with permission from Elsevier][34]

simply be the height of the Schottky barrier as shown in the figure for electons or can be modified by band bending within the material as seen for holes. The barrier seen by holes is increased due to the bending within the material created by the n-type doping in the semiconducting channel.

2.3 Transport models

The most cited analysis of transport in these structures was done by Sze et.al. [34] The analysis reveals several interesting results that provide general insight into MSM device behavior. The structure is two back-to-back Schottky contacts, as shown in Fig 2.1. When a bias is applied, one contact will be in reverse bias while the other will be in forward bias. The reverse bias contact will initially dominate behavior by limiting the current and absorbing most of the potential drop across the device. It is

interesting to note here the assumption that the majority carrier dominates current, particularly at low bias. A Schottky barrier that is reversed bias for electrons, is forward biased for holes. The concept of majority and minority carriers plays an important role in classical semiconductor physics models. This issue however becomes complicated in many material systems that are either undoped or have both carriers at majority carrier levels. For now however, we will assume that electrons are the majority carrier and in fact dominate conduction at low biases. As the applied bias is increased the total area depleted by the contacts will also increase until eventually the depletion regions will meet in a condition referred to as reach through. Once this condition is met the device behavior can be strongly modified. As the bias continues to increase beyond this condition the barriers seen by minority carriers may be strongly influenced and in some cases lowered due to the band bending within the structure. At this point minority carriers can begin to play a dominant role in conduction, giving rise to interesting behaviors and knees in the IV trace as seen in Fig 2.2. This condition can vary depending on the doping and carrier concentration within the semiconducting channel.

It is important to note that one cannot simply analyze the device as two back to back Schottky diodes, as the interaction between the two and the channel itself can create new and interesting behavior. The sequence of energy band diagrams under varying bias conditions is shown in Fig 2.3, demonstrating the changes that take place and the onset of minority carrier current increase due to band bending at the contacts. A simple comparison can be made to help understand the possible behavior of MSM devices by considering the well know bipolar transistor. A bipolar transistor is two back-to-back PN junctions, with a thin base region. These structures do not produce the behavior that would be expected of two diodes back-to-back in a breadboarded circuit, due to the interaction between the two interfaces. For a

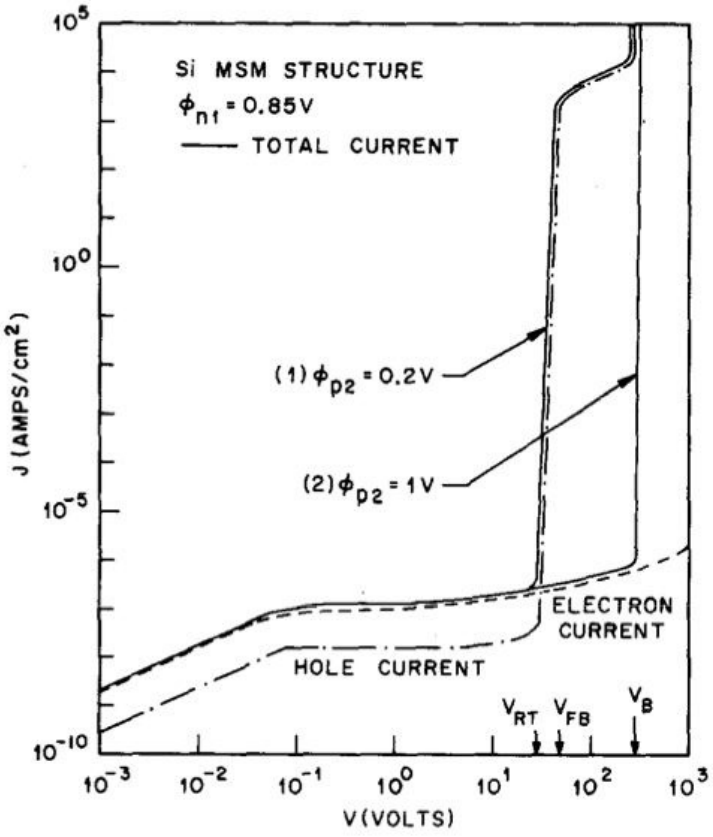

Figure 2.2: IV Trace of MSM device showing two barrier heights [Reprinted from Solid State Electronics, Vol. 14, S.M.Sze et.al. "Current transport in metal-semiconducting-metal structures",1971, with permission from Elsevier][34]

bipolar junction transistor the interaction happens immediately due to the interface proximity, but conditions can occur within an MSM devices that create base-like effects in semiconducting channel as well. This is particularly highlighted when we consider the behavior of the devices under optical stimulus, i.e. a phototransistor.

2.4 Sources of MSM Characteristics

The model presented by Sze et.al. provides a strong initial basis for understanding the behavior of MSM devices, however it usefulness is limited due to the somewhat

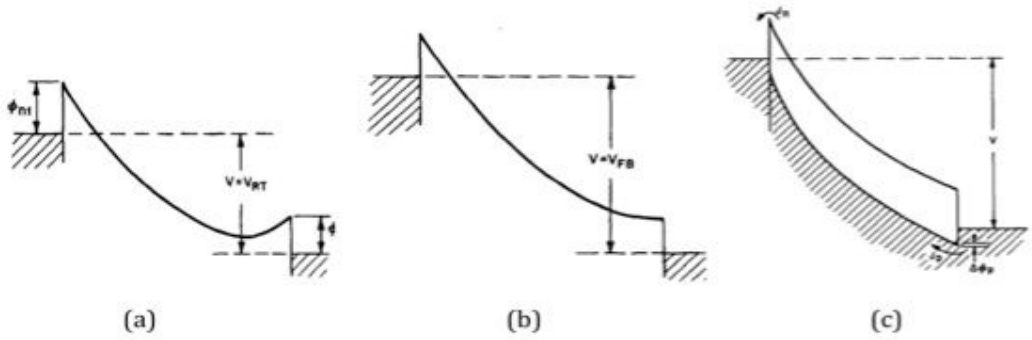

Figure 2.3: Band Diagram of MSM under different bias conditions. a) Reach through, when depletion regions of two contacts meet b) Flat band - when the bands bend to eliminate the internal barrier at the forward biased junction c) Onset of hole current increase [Reprinted from Solid State Electronics, Vol 14, S.M.Sze et.al. "Current transport in metal-semiconducting-metal structures", 1971 with permission from Elsevier] [34]

ideal conditions assumed in the analysis. Practical MSM devices can be influenced by several factors, which will be discussed in the following section. Researchers, in order to explain the unique behaviors seen in more exotic MSM devices, have put forth several more specialized theories, particularly for nanowire-based devices [35; 1; 36]. Fig 2.4 shows a simple schematic of an MSM device and highlights areas of interest to this work.

2.4.1 Semiconducting Material

The material properties of the semiconducting channel will obviously strongly influence the observed behavior of the MSM device. Carrier mobility and concentration play a strong role and under the right conditions these values can be qualitatively evaluated using an MSM two terminal device [37]. The material quality, such as defect concentration and unintentional doping can drastically alter behavior by changing the

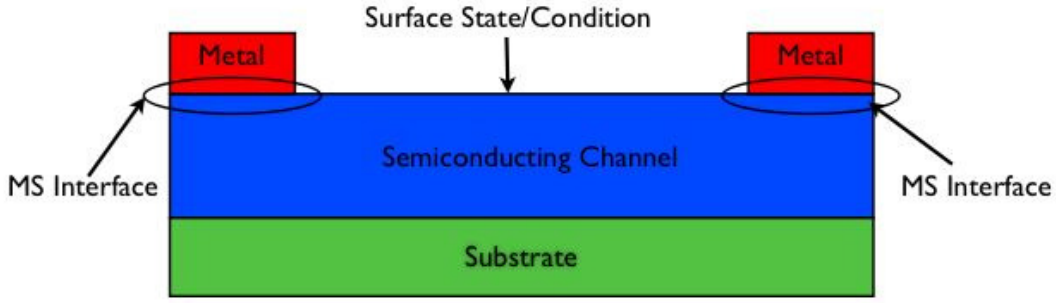

Figure 2.4: Simple diagram of an MSM device highlight the MS interface and the surface of the semiconducting channel

distribution of the potential drop along the biased device. The materials interaction with the deposited metal, i.e. diffusion coefficients, can also affect device performance. In devices at the nanoscale the distribution of dopants and small inhomogeneities can greatly influence the material properties that would normally be averaged out in larger bulk devices. Detector devices are generally more sensitive when fabricated on undoped materials, thereby allowing easier detection of fluctuations in carrier density and conductance of the material. The low doping levels of these materials however make them even more susceptible to large differences when unintentional dopants are not homogeneously distributed.

Additionally, MSM devices based on heterostructured material can add internal electric fields and otherwise create a complex potential landscape before contacts are even added. The built in band diagram then interacts with a contact to often create interesting behaviors not seen in bulk or homogenous materials and potentially significantly change the band diagram shown previously [38]

2.4.2 Metal-Semiconductor Interface

Contacts often play a dominant role in the behavior of MSM devices. The complexity of interfaces and the different chemical reactions that can take place when two materials come in contact can create a variety of different behaviors. Schottky or blocking contacts are typically the expected result of simply depositing metal electrodes on a semiconducting material without any post processing [39; 40]. Several theories have been presented that attempt to predict how a particular metal will behave in contact with a particular semiconductor but despite decades of research no predictive theory exists [41; 40]. Typically devices are designed using empirical data from previous work and a large variation in the measured Schottky barrier can be seen in the literature for many materials. This variation becomes even more prominent when contacting nanoscale materials, as the small contact area can easily introduce large variations from device to device that would otherwise be averaged out in a bulk contact [42; 43; 44]. Tunneling can also play a stronger role in these barriers and must be considered to accurately model the devices, particularly at the nanoscale [45; 46; 47; 48; 49; 50]. The theory presented by Sze assumed purely thermionic emission and does not account for tunneling or thermally assisted tunneling. Finally electrode geometry can also play a dominant role in device behavior, allowing electric fields created between the contacts to influence the behavior of a device beyond the expected depletion length of the interface [51].

Raymond Tung proposed an simple theory to explain the behavior seen in Schottky contacts on an atomistic scale [52; 53; 54]. Tungs theory and explanation lay out a scenario where the observed barrier is created by the chemical bonds at the interface. The most important contribution of his work is the description of Schottky barriers at this scale and with a distribution of inhomogeneous barrier heights. He demonstrates that simply using an average barrier height to model the behavior

of a device is not accurate. If barrier height variation occurs over a short distance, shorter than the depletion length in the material, neighboring barriers can strongly influence each other, creating a complex potential landscape along the interface and into the semiconducting channel. An understanding of these results is important in the examination of Schottky barriers in MSM devices, particularly on the nanoscale where a small contact area can lead to large variation in the observed barrier height from device to device if the heights are inhomogenously distributed. Tungs model is a more accurate description but difficult to formulate and computationally intensive making it cumbersome to apply in a quantitative manner.

Alternatively, if contacts are ohmic, or semi-ohmic as is often the case, the analysis becomes even more difficult as regrowth, surface modification and dopants introduced during annealing can further complicate the model of the interface. For this reason, modeling and discussion of the contacts is limited to a qualitative examination in many cases for MSM devices. Several nano-scale devices however have emerged that take advantage of these contact properties, for instance the Schottky barrier transistor on a carbon nanotube [1]

2.4.3 Semiconductor Surface

MSM devices on a smaller scale can be heavily influenced by surface states and the resulting Fermi level pinning. In devices where the active region is smaller than the typical depletion length of the material, the state of the surface can extend its influence deep into the channel. The surface can also greatly influence the behavior of the contacts before and after metal deposition by modifying the surface very near to the contacts, one can change the carrier concentration at the contact edges and possibly significantly change the device characteristics. If we take for example an undoped GaAs channel of 100nm thickness, we can approximate the depletion depth

using the following:

$$d = \sqrt{\frac{2\epsilon_o \epsilon_r V_s}{qN_a}} \tag{2.1}$$

Where d is the depletion depth,ϵ_o is the permittivity of free space, ϵ_r is the relative dielectric constant of GaAs, 12.9, V_s is the surface potential, q is the charge on an electron and N_a is the doping concentration, for unintentionally doped GaAs it is assumed to be $5 * 10^{14}/\text{cm}^3$. With such a small carrier concentration, the entire channel can be depleted with a surface potential of only 10s of mV, making the channel very susceptible to Fermi level pinning at the surface. This issue becomes of great importance in nanowire devices, where the surface to volume ratio is very large. It can also be exploited to create functional devices [55]

2.4.4 Substrate

In each of the material systems studied in this dissertation, an initial substrate will be used to produce devices or materials. When this substrate becomes part of the device itself, its properties can also influence the observed behaviors. Optical absorption in the substrate of a detector can at times dominate the measured response; while using the substrate as a gate can be a method to further control and alter the properties of devices.

2.5 MSM Detectors

Research groups have fabricated a variety of MSM detectors. Often with new materials and structures this configuration is the first type of device fabricated for testing. Many mature material systems also use this configuration for the design of detectors. Some relevant MSM detectors will be discussed here and in the chapters that follow.

2.5.1 Photodetectors

Several research groups, including ours, have reported on MSM photodetectors [56; 23; 57; 24]. These devices offer several advantages over other photodetectors such as PIN and phototransistor detectors. MSM devices are planar, so they can be monolithically integrated into chips with other devices. The best example of this is MSM detectors using AlGaAs/GaAs material. These detectors, incorporating a quantum well at the interface of the AlGaAs and GaAs offer high-speed detector with low dark currents and the possibility of integration with high electron mobility transistor circuits [24]. Our group has demonstrated several of these devices that will be discussed in Chapter 2. Fig 2.5a shows a typical design of a detector of this type. Along with photodetectors, the devices also demonstrate a strong varactor character. The capacitance of the device changes greatly depending on the applied voltage and the incident optical excitation. The capacitance as a function of voltage for a two-dimensional hole gas (2DHG) MSM is shown in Fig 2.5b. These devices offer another possible circuit element to be integrated with HEMT circuits for use on a single chip for high speed and frequency modulation purposes [58].

2.5.2 Molecular and Biological Species Detectors

Many research groups have also implemented nanostructures into MSM devices. Nanowires in particular offer a strong candidate for detection in this configuration. A group at Harvard lead by Charles Lieber published an excellent example of the potential of nanowire detectors [55]. Using a silicon nanowire based MSM device they were able to functionalize the surface and detect chemical and biological species by monitoring the change in conductivity of the device. Fig 1.6 shows the configuration and results of such a detector device. When a biomolecule, in this case biotin-streptavidin, attaches to the functionalize groups on the nanowires surface in 2.6a, the attachment

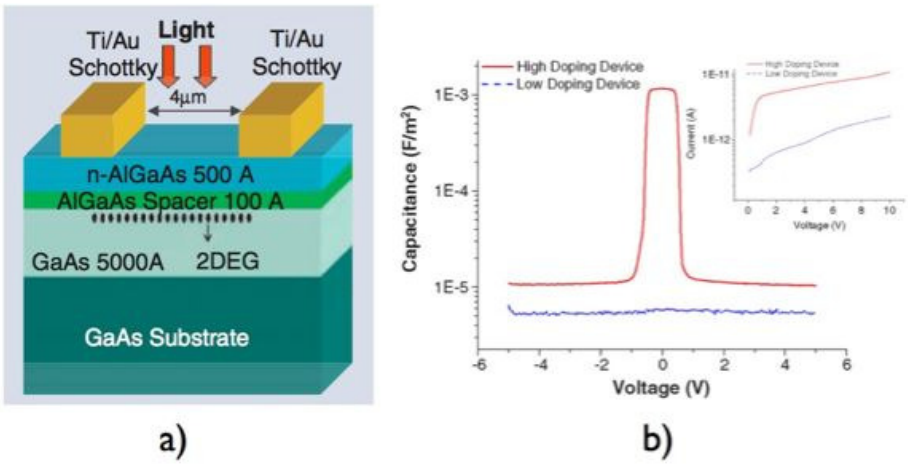

Figure 2.5: a) Schematic of heterostructure quantum well based detector [24] b) Measured capacitance as a function of applied voltage of a two-dimensional hole gas based MSM structure and a structure without a two-dimensional hole gas in the same layered material [58]

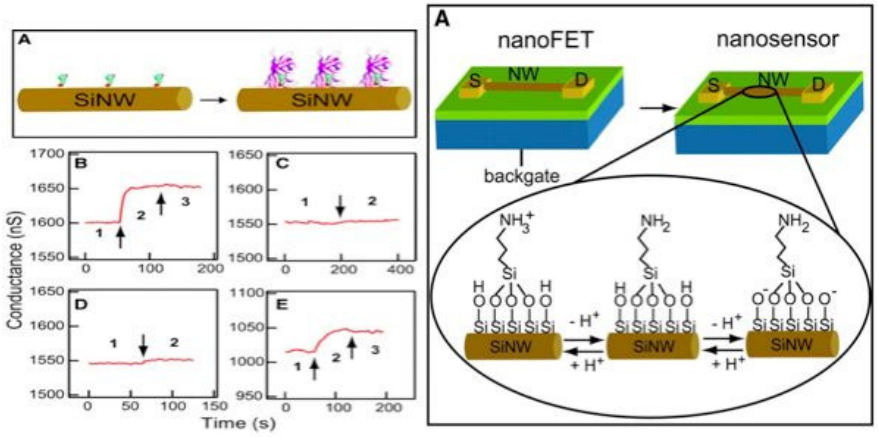

Figure 2.6: Silicon NW based detector. a) A single nanowire detecting Biotin-Streptavidin by attaching to functional groups on the nanowire surface b) pH detection in a nanowire utilizing a surface functionalization that creates charge transfer due to protonization and deprotonization [From [55]. Reprinted with permission from AAAS]

creates a shift in the charges at the nanowire surface, changing the internal potential and charge distribution and resulting in a change in the electrical characteristics of the device. The large surface to volume ratio enables high sensitivity to the surface states, making nanowires a promising platform for detection of chemical and biological agents. Fig 2.6b shows that his can also be done by changing the pH of a solution, thereby changing the charges present and with the correct functionalization this can also lead to a change in the device conductivity.

Many other groups have fabricated and tested a large number of MSM devices with different functionalities and using different material systems. Often the most difficult part of testing these devices is designing and testing fabrication methods to make good contact to the material, control the surface states and control the material properties during growth.

3. Two Dimensional Electron-Hole GaAs

3.1 Heterostructure MSM

Planar heterostructured materials provide an excellent platform for a wide array of devices and detectors. Precision growth techniques allow the incorporation of different band offsets and junction types, as well as introducing strained layers for enhanced properties. Optimizing the internal electric landscape enables different layered structures to provide a specified behavior to suit a particular application. Heterostructures have been shown to be strong detectors of a wide array of radiation from X-ray [22], UV [23], and IR[24] to THz [25; 26; 27; 59; 29] and even microwave radiation [30] as well as charged particles[31]. They have also demonstrated the ability to operate as gas, molecular and biological sensors using surface functionalization [32; 33] and high performance varactors [60; 61; 62] in additional to the commercially used high electron mobility transistors and laser

In detection of electromagnetic radiation, heterostructures offer the unique opportunity to engineer absorption at different energy levels in the same substrate by using semiconductors with different bandgaps. Engineering quantum wells into these devices produces materials capable of very high speed operation and long carrier lifetimes, produced by the use of modulation and delta doping techniques that separate ionized dopants from the carriers and increase mobility of electrons and holes in the wells[63; 17]. The ability to grow wide bandgap material on lower band gap material also provides an opportunity to design devices with reduced dark currents, strong gate coupling with low leakage and even heterodimensional contacts[64; 24; 65].

A heterostructure MSM photodetector is an excellent platform to create a high speed, low noise and high responsivity device in the 830nm range when using GaAs as

the absorption material. Using Schottky contacts situated on an AlGaAs barrier layer provides a large barrier to incoming carriers and reduces the dark current of these devices[66]. Typically however, long tails plague the high-speed response of these detectors [24]. The origin of this tail is still under debate with theories proposing that they are attributed to minority carriers generated deep within the material, which require a long circuitous path to reach the contacts and be collected and optical gain to due surface states being filled near the contacts, thereby lowering the contact barrier. Other published work has also suggested that the electron-hole plasma created due to electron-hole pair formation alters the internal landscape of the devices.

3.2 Two Dimensional Electron-Hole Gas Structure

Dual wells in a heterostructure present a unique and interesting platform for the creation of novel detectors. Initially the devices discussed here were designed for improvement on existing single quantum well based high-speed photodetectors. The structure, however, presented many interesting qualities and characteristics that will be discussed here. A dual quantum well device consists of two quantum wells spatially separated by a barrier layer that effectively separates charges. The devices are difficult to design, as shifting the Fermi level from the conduction band to valence band must induce a very large internal electric field over a short distance if the wells are to be closely spaced. The benefits of such a structure though are several fold. Particularly in quantum well photodetectors, minority carriers that are often pushed deep within the detector by the electric field created by the modulation doping dominate the time response. In the case of a Two-Dimensional Electron-Hole Gas (2DEHG) however, both carrier types have a high mobility, high carrier concentration quantum well to travel in effectively, eliminating a minority carrier all together as both electrons and holes are present and participate in conduction. The presence of both carriers and

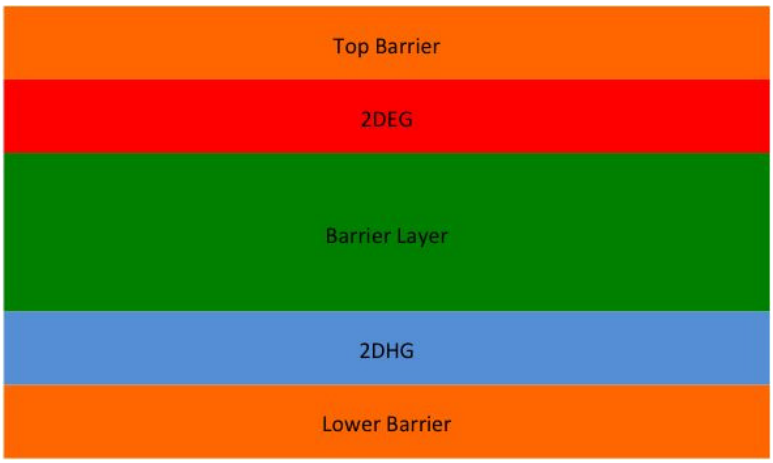

Figure 3.1: Simple Schematic of the structure of a dual electron-hole quantum well

the potential for them to interact creates significant difficulties in the analysis of the internal potential of the structure. A simple diagram of a 2DEHG structure is outlined in Fig 3.1

3.2.1 Coulomb Drag and Plasmonic Interaction

Previous work on 2DEHG structures has primarily been to explore the unique physics associated with two spatial separated but interacting quantum wells. Much of the work has concentrated on minimizing the distance between the wells, making it smaller than the inter-particle spacing within each individual well. The difficulty lies in accommodating the necessary electric field between the layers, which is approximately 108 V/cm for a 10-20nm spaced system [67].

The system was first studied in by Sivan et. al.[68] Several groups have fabricated 2DEHG systems by various methods, including using standard photolithography methods [69] and systems have been made in silicon based structures as well as GaAs[70]. Several groups have used gating to create the populated wells [71; 72; 68] while optical generated 2DEHG devices have also been reported [73]. These create

structures with independently tunable carrier densities in each well.

Published work has concentrated on coulomb drag experiments [74; 75; 76]. Several groups have published work that explores the effect of current in one well on the behavior of carriers in another well. In these experiments the wells are contacted separately, inducing a current in one does not create a current in the other. Then at cryogenic temperatures, current is passed through one well and the voltage induced across the neighboring well is measured, this induced voltage is created by coulomb drag. Simply stated, the coulombic interaction between the wells creates momentum transfer from the well with current to the well that is not biased. The value of this induced voltage has a strong relation to the interaction forces between the carriers in the separate wells. Other work has shown that the plasmonic frequencies within the wells can be altered and affected by events within the neighboring wells [77; 78] The plasmonic frequency of the wells is created by the collective oscillation of carriers and this property has been exploited in terahertz detectors based on high electron mobility transistors and double quantum well structures [28; 29].

The structure most resembling that which will be presented here was done by Eberl et.al. [79]. As shown in the Fig 3.2, a 2DEHG was created using specifically placed delta-doping layers in an AlGaAs barrier between two square GaAs quantum wells. The wells were spaced at a distance of about 200nm and experiments demonstrated that despite the large distance the wells indeed demonstrated coulombic interactions at low temperatures. Interestingly, in this work the group outlines the difficulty in producing such a structure. The method used here however does not lend itself to producing a practical detector based on this design. The AlGaAs barrier is a low mobility, large band gap material not suitable for most detector applications, except perhaps at shorter wavelengths. Additionally, the presence of the delta doping layers within the barrier could potentially degrade performance. The literature presents

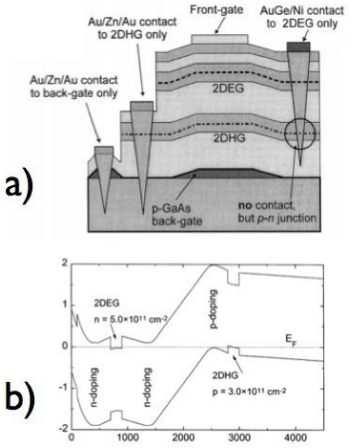

Figure 3.2: 2DEHG structure used for the study of Coulomb Drag a) Describes physical device structure b) Energy band structure [Reprinted from Materials Science and Engineering, Vol B51, H.Rubel et.al. "Fabrication of independently contacted and tuneable 2d-electron-hole systems in GaAs/AlGaAs double quantum wells", 1998 with permission from Elsevier][79]

very little characterization of these structures at room temperature, providing no information on their use as practical electronic devices. Characterization of these materials and devices based on these structures can provide information on possible applications and may also reveal interesting and new behaviors not observed in single carrier quantum well devices. This work will concentrate on room temperature characterization, though low temperature measurements will be used to investigate and identify thermal signatures of some observed behaviors.

3.3 Design and Structure of the 2DEHG

The objective in the design of the 2DEHG material discussed here was to create a structure that could improve the performance of quantum well based photodetectors by improving the collection of the minority carriers within the device. To accomplish

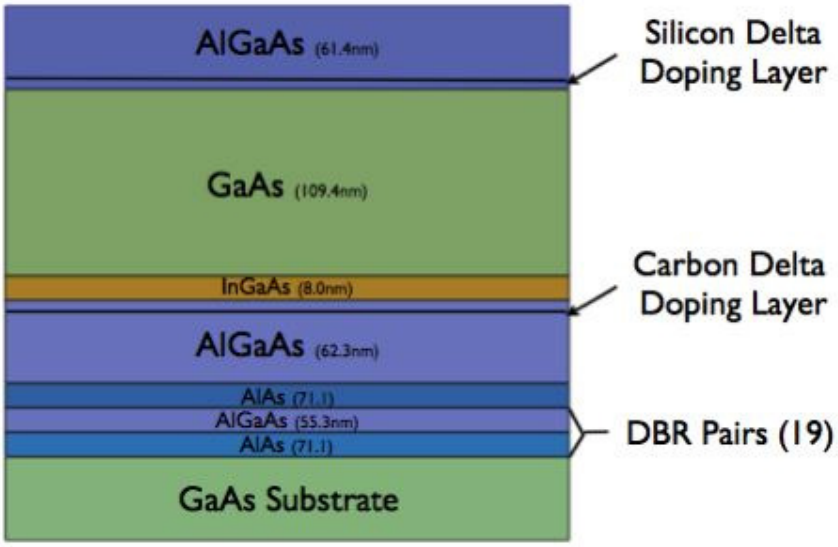

Figure 3.3: Structure of 2DEHG wafer

this structure was designed to eliminate majority and minority carriers and have both carriers participate in conduction. A schematic of the grown structure is shown in Fig 3.3. The sample was grown on a semi-insulating GaAs substrate using metal-organic chemical vapor depostion, utilizing AlGaAs barrier layers with an aluminum content of 30% to maximize the band offset without introducing deep level trap states [41]. In order to create a hole well at the bottom edge of the GaAs absorption region a pseudomorphic InGaAs layer was introduced. This layer enables the formation of a hole well due to the reduced band gap compared to GaAs. For the electron well a Si delta-doping layer was used, separated by a 5nm spacer layer [63; 17]. The electron well is a notch well, created at the upper interface between the AlGaAs upper barrier and the GaAs absorption region. In the lower barrier a C delta doping layer, separated by 5nm from the InGaAs 8nm layer, provides the carriers to populate

the hole well. The design includes a thin (5nm) n+ doped capping layer to serve as protection to the $Al_{0.3}Ga_{0.7}As$ and also for the formation of ohmic contacts to the structures. In one sample a Distributed Bragg Reflector (DBR) structure was grown beneath the lower barrier. This structure is made up of 20 quarter-wavelength stacks of AlAs and $Al_{0.3}Ga_{0.7}As$ and tuned to a wavelength of 850nm. In designing the Bragg reflector three requirements had to be met. The material had to have a large refractive index, be lattice matched to GaAs and have a bandgap greater than GaAs to prevent absorption of the optical signals.

The complete structure of the wafer from surface to substrate is as follows: 3nm GaAs cap with $n + 3 * 10^{18}/cm^3$ doping, 56.4nm $Al_{0.3}Ga_{0.7}As$ upper barrier layer, Si delta doping layer of $6 * 10^{12}/cm^2$, 5nm $Al_{0.3}Ga_{0.7}As$ upper spacer layer, 109.4nm GaAs absorption layer, 8nm $In_{0.2}Ga_{0.8}As$ strained 2DHG channel, 5nm $Al_{0.3}Ga_{0.7}As$ lower spacer layer, C delta doping $2.5 * 10^{12}/cm^2$, 57.3nm $Al_{0.3}Ga_{0.7}As$ lower barrier layer, (Bragg sample only 19 Layers of 51.1nm AlAs/62.3nm $Al_{0.3}Ga_{0.7}As$,) 200nm GaAs buffer layer on a semi-insulating GaAs substrate

3.4 Simulated Band Structure

The band diagram is simulated using a Poisson Schrodinger solver designed by Greg Snider at the University of Notre Dame [80]. The simulator uses the method of finite differences to calculate the one-dimensional band structure of an arbitrary semiconductor structure. The simulation is done assuming a Schottky contact at the surface with a barrier level of 0.87eV, a typical value for Ti contacts on GaAs. A comparison of the simulated band structure of the device with and without Bragg is shown in Fig 3.4 (the entire Bragg reflector is simulated but not shown). The two structures reveal only subtle differences with small variations in the bending in either well. Overall the simulation shows the formation of two wells at either side of the

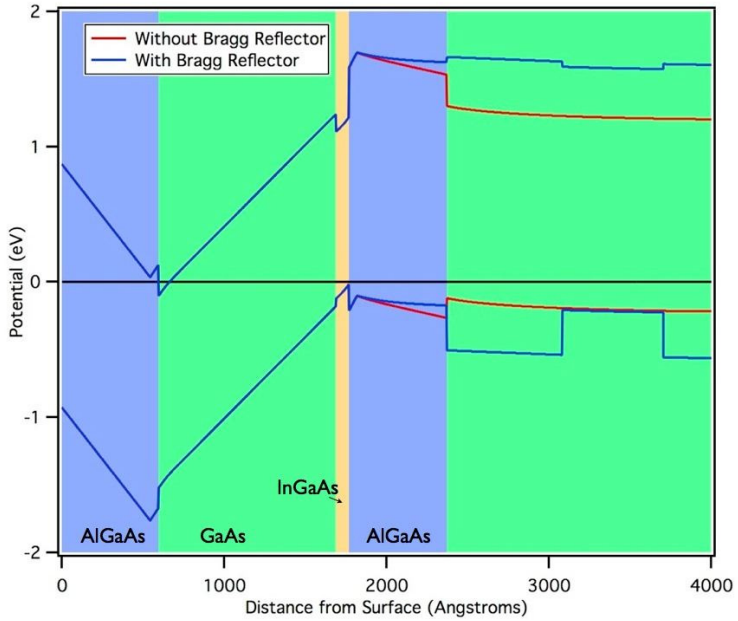

Figure 3.4: Simulated Band Diagram for 2DEHG device with Bragg and without (Entire Bragg region not shown)

GaAs absorption layer. The InGaAs also becomes triangular due to the large electric field but it is not distorted enough to prevent the formation of confined states as shown in Fig 3.5. The InGaAs band gap is estimated based on published literature of similarly grown strained InGaAs layers [81; 82]. A Schrodinger solution to the areas around the GaAs absorption regions edges provide the wavefunctions and energy of the confined states created due to the narrow potentials. The simulation also shows that the presence of one well depopulates the other when the separate delta doping layers are not included.

3.4.1 Confined States

A zoomed in view of the GaAs absorption region is shown in Fig 3.5 In the electron well there are two confined states located slightly above the Fermi level, labeled e1

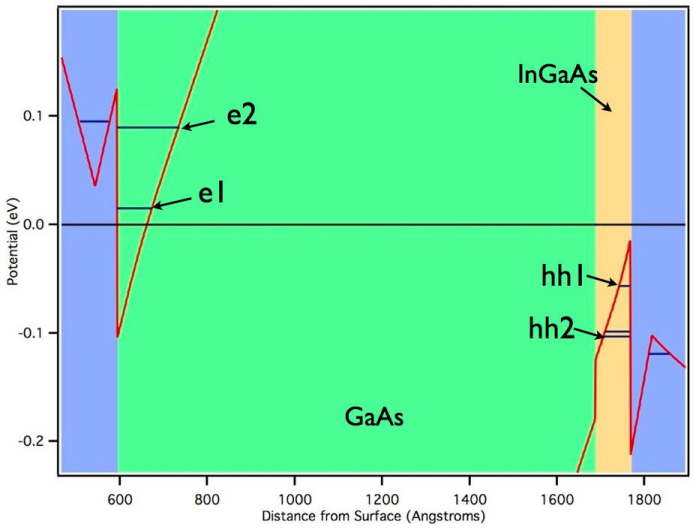

Figure 3.5: Energy Levels in the Electron and Hole wells within the GaAs absorption region

and e2 in the figure. In the hole well the heavy hole 1(hh1), heavy hole 2(hh2) and light hole 1(lh1) state are shown. Higher energy states exist within the InGaAs well, which are not shown. Also of interest is the formation of confined states in the delta doping layers.

3.4.2 Carrier Concentrations and Built in Electric Field

Fig 3.6a shows a simulated plot of the electric field distribution and Fig 3.6b the carrier concentrations within the heterostructure. Of interest, the electric field is approximately 125kV/cm in the absorption region with a slightly higher field in and around the quantum well regions. This is a very strong internal field, dropping approximately 1.3V across 100nm. We also see a slight but possibly significant difference in the electric field in the lower barrier between the Bragg sample and the sample without a Bragg reflector. Calculation of carrier concentrations find a sheet

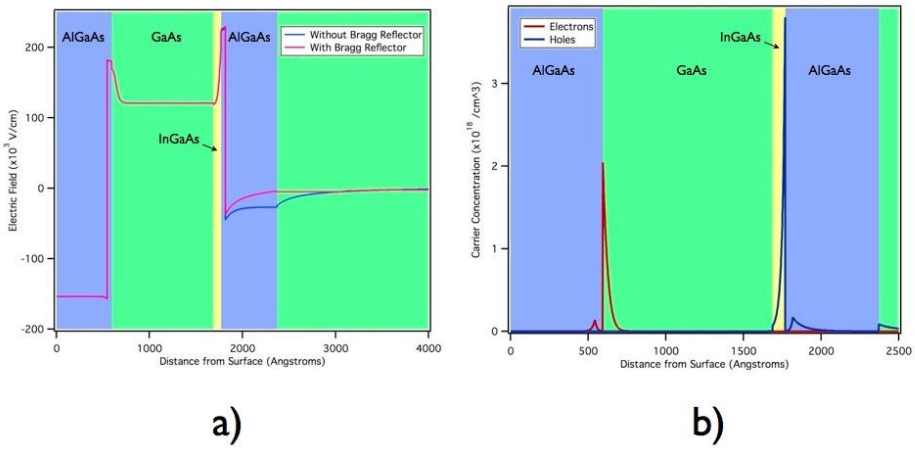

Figure 3.6: a) Simulated electric field distribution in the 2DEHG wafer b)Simulated carrier concentration in 2DEHG wafer

carrier density in the range of $5 * 10^{10}/\text{cm}^2$ for both electrons and holes. These densities are, as expected, low for a two-dimensional carrier gas. Further simulation work demonstrated the strong pinning effect of the delta doping layers on the band structure, applying a bias and changing the Schottky barrier energy level at the surface only modifies the potential in the upper barrier, having only a small effect on the absorption region and wells. The delta doping layers are likely to screen any possible surface potential effects within the device. Finally, of important note is the observed barrier that the Bragg reflector creates to holes generated within the substrate, while providing a much smoother potential for electrons to travel across.

3.5 MSM Fabrication

MSM devices reported here were fabricated using photolithography. The GaAs capping layer was removed using a citric acid/hydrogen peroxide selective etch, that removes the GaAs layer without etching the underlying AlGaAs Layer[83]. In the case of photoluminescence measurements the GaAs cap was removed using a digital etch

technique utilizing hydrochloric acid and hydrogen peroxide in separate steps [84]. For devices a silicon nitride layer is then deposited using plasma-enhanced chemical vapor deposition. The silicon nitride layer serves to isolated the contact pads from the underlying substrate to improve the dark current and noise levels of the device. After nitride deposition the entire structure is mesa isolated using either a wet etch piranha solution (sulfuric acid/hydrogen peroxide/water) or reactive ion etching. The mesa etching serves to isolate neighboring devices from one another and ensure that electron-hole pairs generated by incident light are created near electrodes for faster collection. The nitride layer above the active area of the device is removed and interdigitated titanium/gold electrodes deposited, along with large pads for probing on the neighboring silicon nitride coated areas. Titanium is known to make a Schottky contact with a large barrier (0.87eV for electrons) and good stability on AlGaAs. A scanning electron micrograph of a fabricated device is shown in Fig 3.7.

A variable set of geometries was fabricated on the same chip, with electrode finger widths of 1 and 2um and finger spacings of 1, 2 and 4um. The active area of each device was 40um x 40um. The inset of the figure shows the Bragg layers present in one of the samples. A higher etching rate on the AlAs layers creates a corrugated sidewall in the Bragg region allowing them to be imaged directly.

3.6 Electrical Characterization Setup

Electrical characterization was done using two separate probe stations. An Agilent parameter analyzer with tungsten probes and a Lakeshore Cryogenic probe station using Au/Be probes, a Keithley picoammeter and a self-written automation system using GPIB communication. Measurements were primarily done in ambient conditions.

Dark measurements on the devices revealed an average current near 1nA at 10V

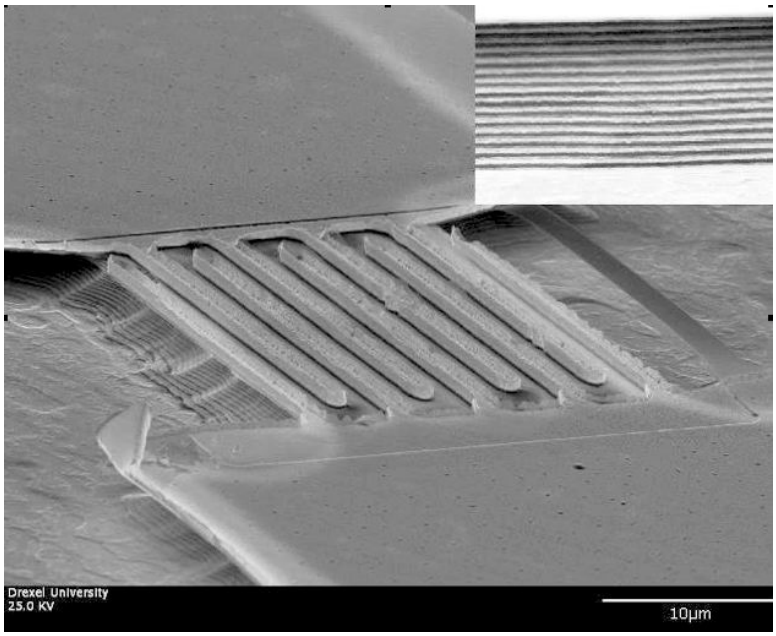

Figure 3.7: SEM micrograph of fabricated 2DEHG MSM on substrate with Bragg reflector. Inset shows the etched Bragg reflector region

for devices without a Bragg reflector and a 2V knee in the traces. The dark current for the Bragg devices was an order of magnitude lower, falling between 10 and 100pA at 10V, with a knee in the current-voltage trace at near 2.5V. This measurement reveals the first difference between the two devices that would not be predicted by the band diagram and expected barriers. The difference could originate from several sources. Differences both in substrate growth and in device processing could be responsible, though the precision of the crystal growth and the fabrication of multiple device sets on the samples would indicate that it would not lead to an order of magnitude difference in the dark current. The other possibility is the change in the potential landscape beneath the contact, which may create additional conduction paths in the devices without a Bragg reflector. More of this topic will be discussed in the following sections.

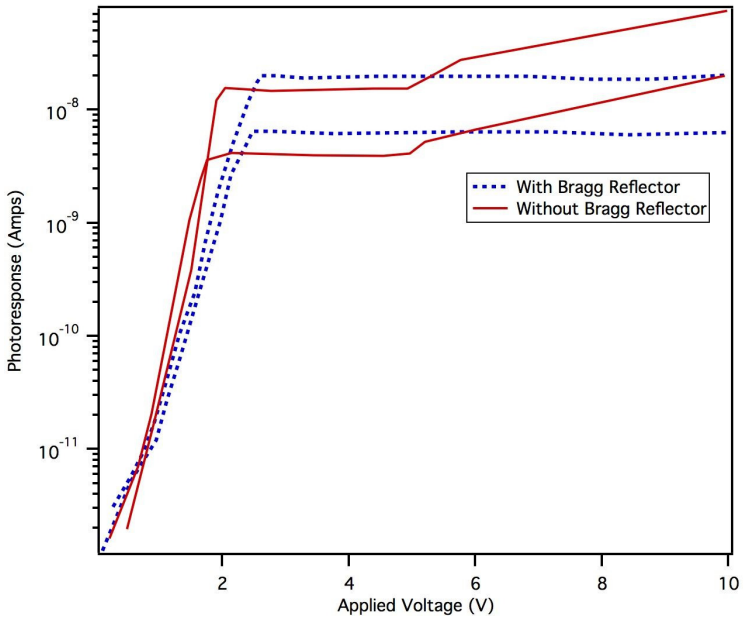

Figure 3.8: DC Photoresponse of 2DEHG devices. Traces taken at 850nm with powers of 8.2uW and 4.1uW each

3.7 Photoresponse

3.7.1 DC Photoresponse

Fig 3.8 shows representative photoresponses from both device types at two different powers. Both devices show a strong increase in current with applied bias followed by saturation near 2V, with the voltage knees being comparable to those seen in the dark current traces. Above 5 V however a significant difference is seen in the traces, as the Bragg sample maintains saturation and the device without a Bragg reflector begins to increase in current again, increasing its responsivity beyond that of the Bragg reflector. This can be seen even more clearly in Fig 3.9. Fig 3.9a shows the photoresponse as a function of intensity at 850nm at 4V bias, the responsivity of both devices remains close over a broad range of intensities, while at 10V the device without a Bragg reflector demonstrates a clearly larger responsivity across all intensities.

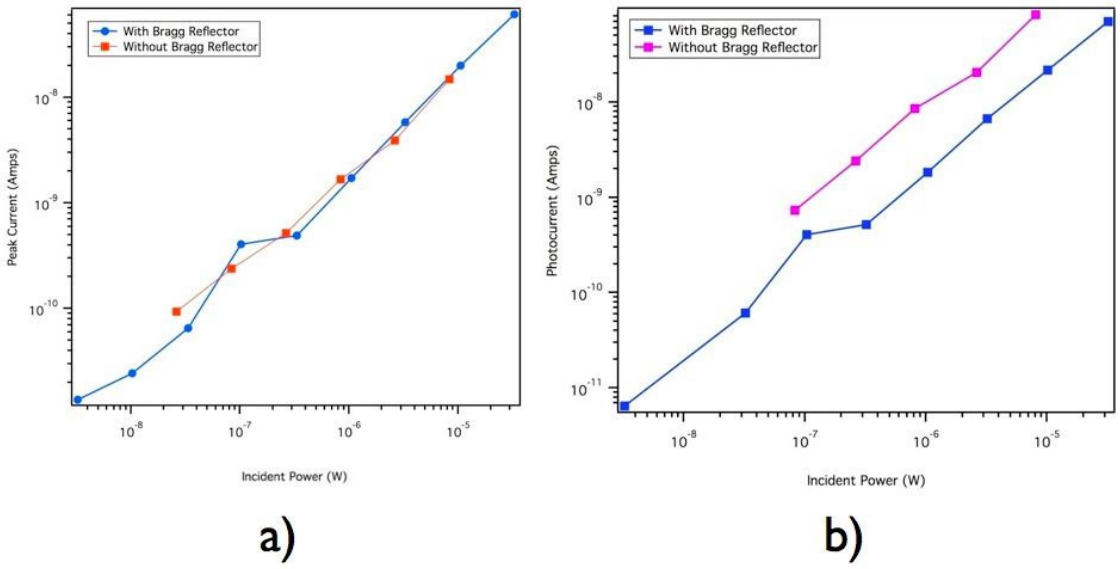

Figure 3.9: Photocurrent as a function of 850nm incident laser power for a)4V bias and b)10V bias

The Bragg reflector is included in the device to improve performance by re-circulating incident light within the absorption region. The larger response in the device without a Bragg reflector indicates absorption and therefore collection of photo-generated carriers in the substrate region of the device or possibly a gain mechanism that is occurring to increase the resulting current. This result will have relevance in the discussion concerning the high speed optical response of the devices.

3.7.2 Photocurrent Dependence on Wavelength

Fig 3.10 shows the photoresponse as a function of incident wavelength for the Bragg devices. The response shows a clear peak at 846nm at all applied bias values. Also visible are two separate peaks near 900nm and 950nm, possibly originating from the InGaAs region. These two peaks will be discussed further in a later section.

Fig 3.11 shows the response of the device without a Bragg reflector as a function

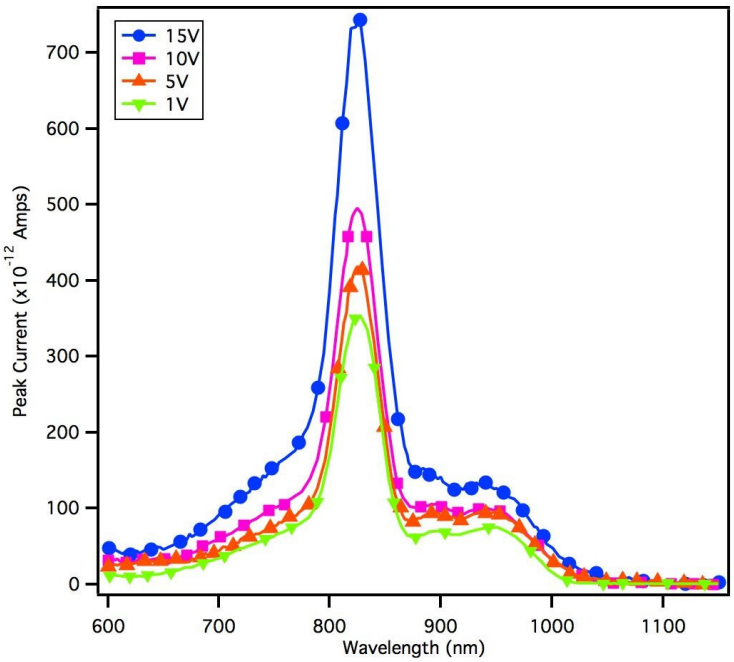

Figure 3.10: Photoresponse of the Bragg device under different wavelengths at varying device bias

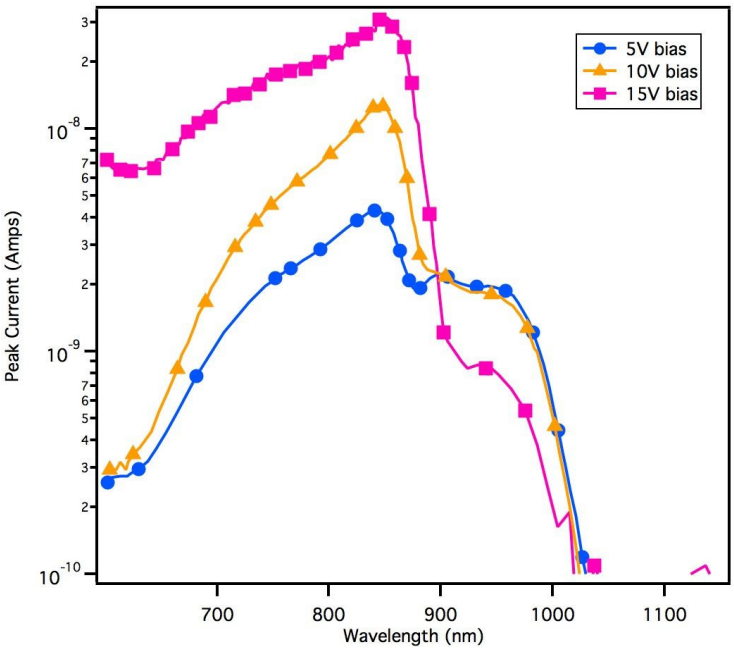

Figure 3.11: Photocurrent as a function of wavelength in a device without a Bragg reflector at varying biases.

of incident intensity. At 5V, the trace looks similar to that of the Bragg device, with the peak at 900nm being slightly sharper and the peak at 850 broadening, primarily due to the absorption spectrum of GaAs and no Bragg to narrow the absorption. The response changes significantly however at 10V with the lower wavelength peaks becoming considerably less prominent and the 850nm peak dominating the trace. This response again indicates the possibility of carriers being generated and collected from the substrate and GaAs buffer layer. Of significant interest is the signal at 15V, here the photoresponse in the 900-950nm wavelength range actually decreases compared to lower bias and the overall shape of the spectral response changes. This provides some indication that the InGaAs well region is not participating in conduction at this bias value.

3.8 Capacitance-Voltage Measurements

Schottky contacted heterostructure MSM devices are know to produce a strong varactor response [85; 86]. Several publications have examined the origin of these effects and the usefulness of these devices as varactors in practical circuits.

Fig 3.12 shows a trace of the measured capacitance as a function of applied voltage in dark conditions and under illumination. The illumination is provided by a broad spectrum lamp. The measurements have however been replicated with a tunable, controllable source and produced similar results. The dark trace is typical for a heterostructured MSM device, with a peak voltage at zero applied bias and a steep decrease in capacitance as the absolute value of the bias increases and then saturating at a minimum value. Under illumination however the device reveals a unique shape that is not seen in typical MSM devices. The illuminated CV shows two capacitive plateaus reaching a minimum value at a bias near 3.5V. The first plateau is approximately 3.5pF and this value holds relatively constant until the bias reaches of value

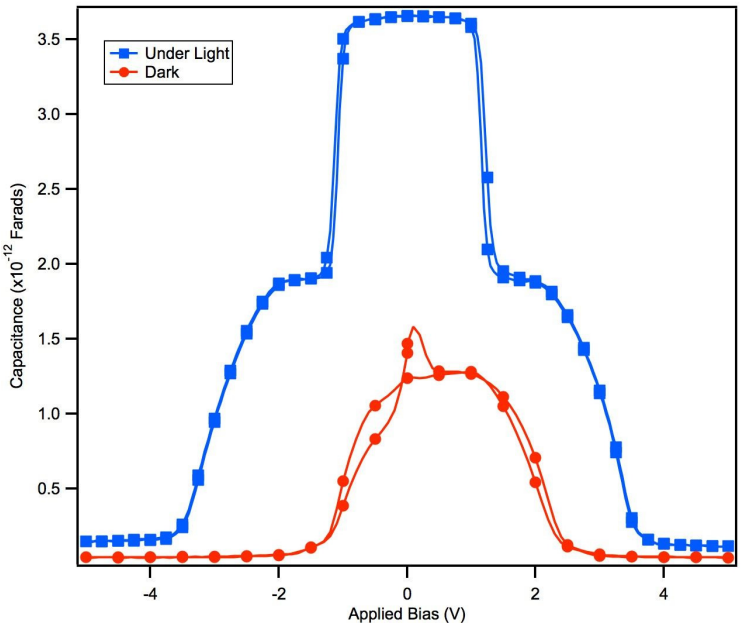

Figure 3.12: Capacitance as a function of applied bias on a device without a Bragg reflector, a finger width of 2um and a finger gap of 2um. Illumination is broad band lamp light

of around 1.75V, it then abruptly falls to 2pF and slowly decays until falling to a minimum value around 200fF. Interestingly the 2V transition knee also occurs in the photoresponse.

Fig 3.13 shows the results for a Bragg device in dark conditions. There is a strong frequency dependence, some of which may be a result of the probe station itself, though it has been calibrated across the full frequency range. Interestingly is that at higher frequency, the dark trace also begins to develop the dual plateau shape, though considerably narrower than seen under light. The plateaus have approximately the same capacitance values as those under light.

Fig 3.14 shows the same device under full lamp light. The lower frequency traces develop very interesting features, especially the formation of wings between 2 and 3V absolute bias. The value at 0V bias appears unchanged across all frequencies however

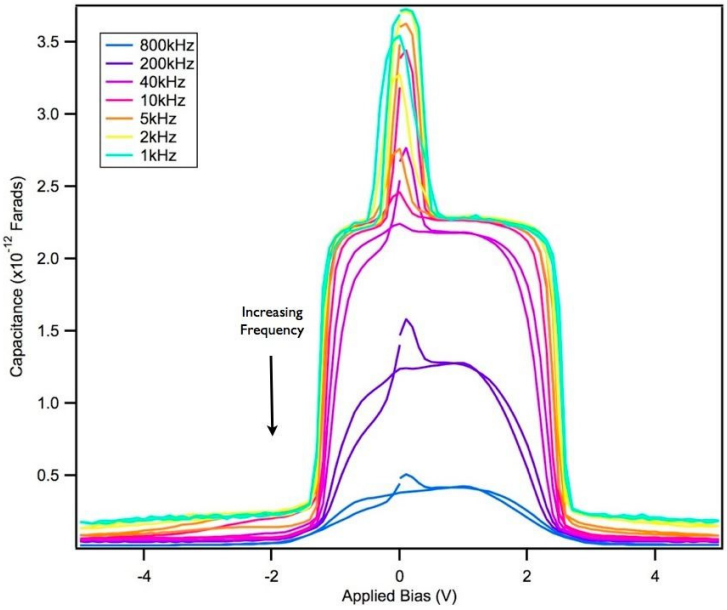

Figure 3.13: Capacitance as a function of applied bias for a 2um finger width, 2um gap device with a Bragg reflector under dark conditions and varying measurement frequency

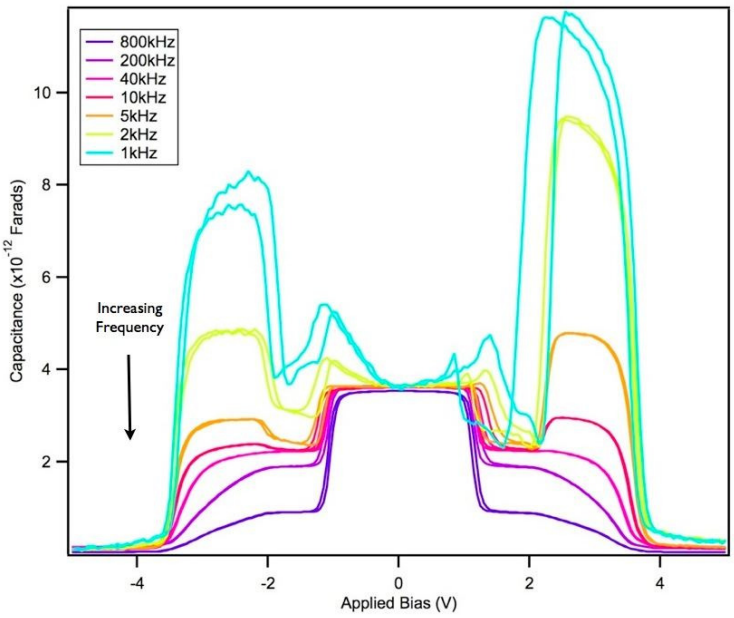

Figure 3.14: Capacitance as a function of applied bias for a 2um finger width, 2um gap device with a Bragg reflector under broad band lamp light and varying measurement frequency

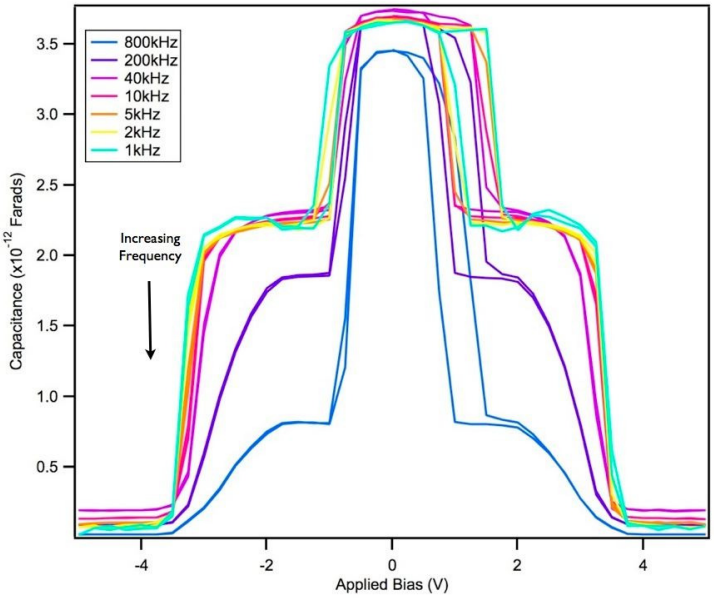

Figure 3.15: Capacitance as a function of bias for a Bragg device at different frequencies and under half power lamplight

and has a similar value to the dark trace 2nd plateau at higher frequency. The knee voltages also appear to shift, with the device losing much of the asymmetry seen in the dark traces under light.

Fig 3.15 provides the same set of traces under 1/2 the incident power. At high frequency there is a hint of the development of wings but the traces instead look similar to the dark set. Again with similar capacitance plateau values. More evident here is the increase in the transition voltages at which capacitance changes take place. The knee voltage also increases with decreasing measurement frequency. This feature may be a result of the onset of wings.

Fig 3.16 and Fig 3.17 show a comparison of the three measurement states: dark, light and half light at two different measurement frequencies: 800kHz and 1kHz. The differences are substantial. At 800kHz the light and half light traces are very similar with just small changes in magnitude and knee voltages. At 1kHz however the half

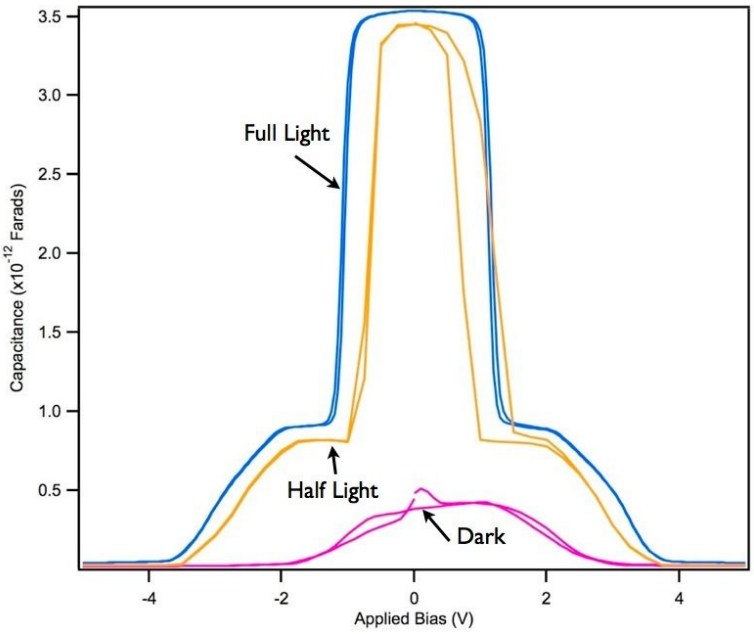

Figure 3.16: Capacitance as a function of voltage at 800kHz in dark, light and half light

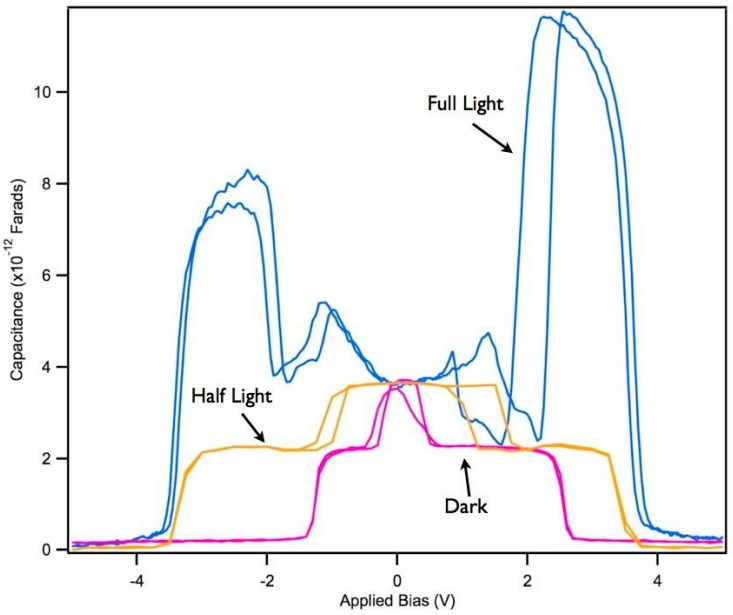

Figure 3.17: Capacitance as a function of voltage at 1kHz in dark, light and half light

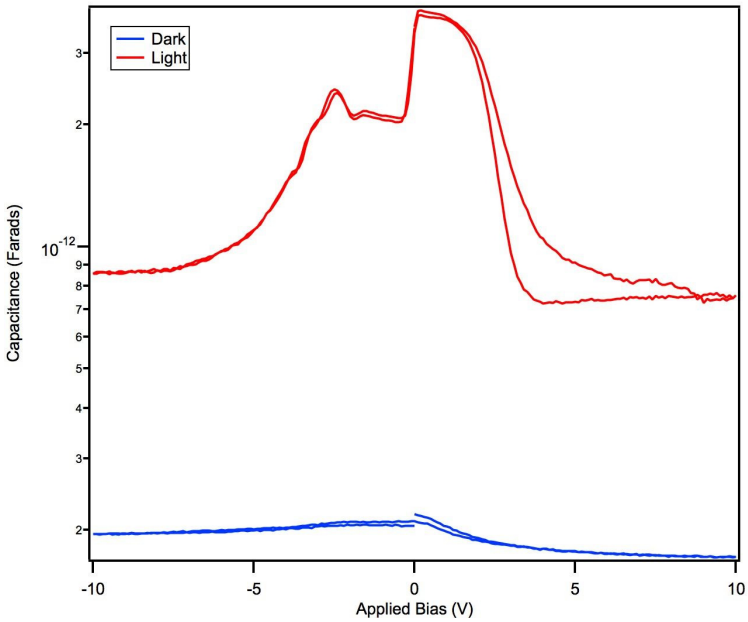

Figure 3.18: Capacitance as a function of voltage measured between the Source contact and the substrate

light more resembles the dark trace with widened plateaus. An understanding of the origin of the wings seen in full light many shed some light on some of the other behaviors seen in these devices.

Measurements were also taken between the contacts and the substrate, contacted with a layer of silver paste. In this configuration, the large substrate contact area should create an asymmetric device that is dominated by the contact on the top surface.

Fig 3.18 shows the results of such a measurement at a 10kHz. There is a definite asymmetry present in the response with a very low dark capacitance. There remains a response at both voltage polarities however, indicating that both carrier types may be participating in the capacitance measurement. The positve bias side has a shape not too dissimilar from the dark trace seen between the two top contacts. This provides some indication that the channel is dominating the capacitance under light.

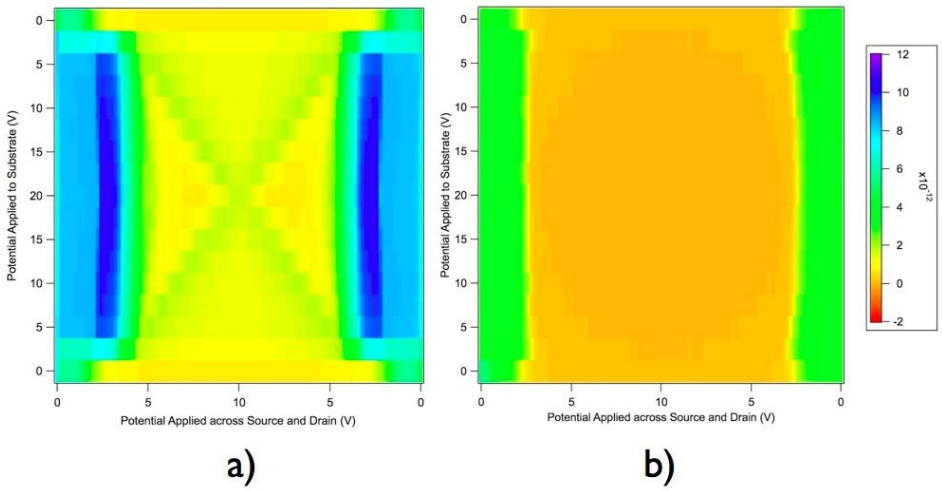

Figure 3.19: Gated Capacitance Map of device with a Bragg Reflector. Horizontal access is bias applied across source and drain, vertical axis is the device applied to the substrate. Capacitance is measured across the source and drain contacts. a) Under Light b)Dark

The measurement from contact to substrate should only include the area beneath the pad, which is shielded from incident light. If this measurement shows a response similar to the dark across pads, then one can expect that the carriers generated in the channel are creating the observed effects and it is not a result of a change in carrier concentration beneath the contact pads.

Even more interesting results occurred when looking at gated capacitance. The capacitance measurement is taken across the source and drain electrode while a bias is applied to the substrate.

Fig 3.19 is two 2D images of capacitance as a function of applied bias and gate bias. The dark response is again fairly flat as expected, the light response becomes much more complicated with observable peaks changing voltage position as a function of applied gate. This work is still preliminary and considerably more data needs to be generated to draw strong conclusions.

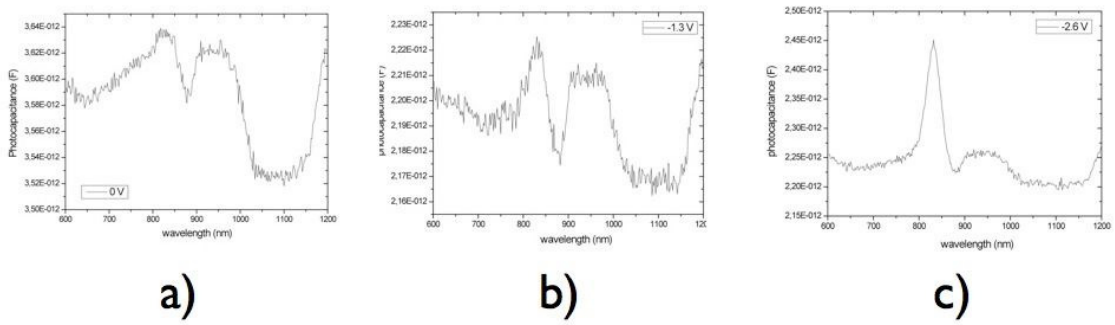

Figure 3.20: Capacitance as a function of incident wavelength at a) 0V b) -1.3V and c)2.4V

3.8.1 Capacitance Dependence on Wavelength

Further investigation by varying the wavelength of incident light and measuring the capacitance at different biases reveals that there is a strong wavelength selectivity to the measured capacitance.

Fig 3.20 shows three plots, at different biases, of the capacitance as a function of incident wavelength. At 0V and -1.3V, we see two peaks in the 830nm and 950nm range. At 2.4V however, 830nm appears to strongly affect the capacitance, implying that absorption in the GaAs layer is responsible for the capacitance at 2.4V applied bias. This bias is the region of wing formation, implying that carriers in the InGaAs well do not participate in creating the observed effects.

3.9 High Speed Photoresponse

A substantial amount of research has been published on the time response of MSM detector structures. Monte Carlo simulations on this devices reveal several response limiting factors including minority carrier transit time and barrier lowering due to charge build up [87]. Measurements have been performed on a wide array of

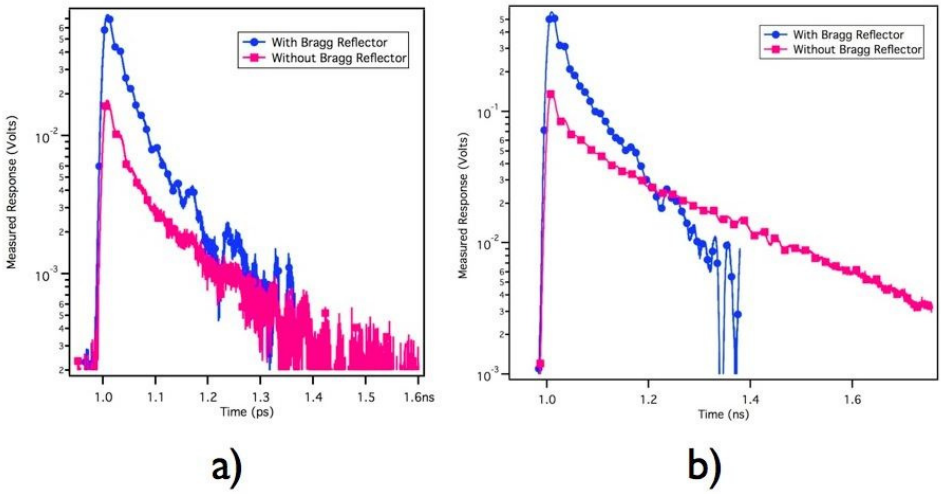

Figure 3.21: Time response of a Bragg device and a device without Bragg. The devices have a gap of 2um and finger width of 2um, the incident wavelength is 830nm. a) Incident power of 50uW b) Incident power of 500uW

heterostructured substrates, typically with interdigitated finger electrodes and narrow absorption regions [65; 88]

3.9.1 Measurement Setup

Time response measurements are taken at the Naval Research Laboratory, Washington DC in the lab of Dr. Marc Currie. The laser used for the optical signal was a 720nm-980nm tunable Ti-Sapphire laser with a 150fs pulse width and a 76MHz repetition rate. The response is measured using microwave probes with a frequency rating of 60GHz and a SD-32 50GHz sampling oscilloscope. The AC response is separated out using a bias-T with a frequency response up to 50GHz. Power measurements are taken as a DC averaged value and the measurements are taken in ambient conditions.

3.9.2 Low Power Time Response

Fig 3.21 shows the high-speed response traces of both wafers at two different powers with an applied bias of 10V. The Bragg peak at similar powers is significantly higher, contrary to the DC Photoresponse. At the lowest powers both traces return to zero signal at close to the same rate. As the power is increased however, the fall time of the device without a Bragg reflector begins to increase considerably, developing a longer tail that decreases its overall frequency response as seen in Fig 3.21b with an order of magnitude increase in incident power. This is an effect often seen in single well detectors as well.

3.9.3 Bandwidth of Measurement Setup

It is important at this point to indicate some of the drawbacks of the high-speed measurement setup used. The speed of the detectors approaches the limits of detection in the setup and the traces on the shorter timescale are strongly influenced by the sampling period used for the measurement. For this reason the full width half max values shown can vary. A system calibration may have prevented this and allowed more accurate readings at the short time scale but was not performed. For this reason the full width half max values will not be discussed and be considered to be more a measurement of the system response itself. The long time scale features, the ones that this work is primarily interested in, however, are consistent between measurements at different time scales and can be considered indicative of the device behavior itself. To create an accurate bandwidth of the measurement system test structures would have had to be created on the substrate for calibration. Without this calibration the system bandwidth is undefined and can possibly vary from sample to sample. The ringing seen in the traces is attributed to LRC resonance and signal reflections within the bond pads. This effect can influence the observed behaviors

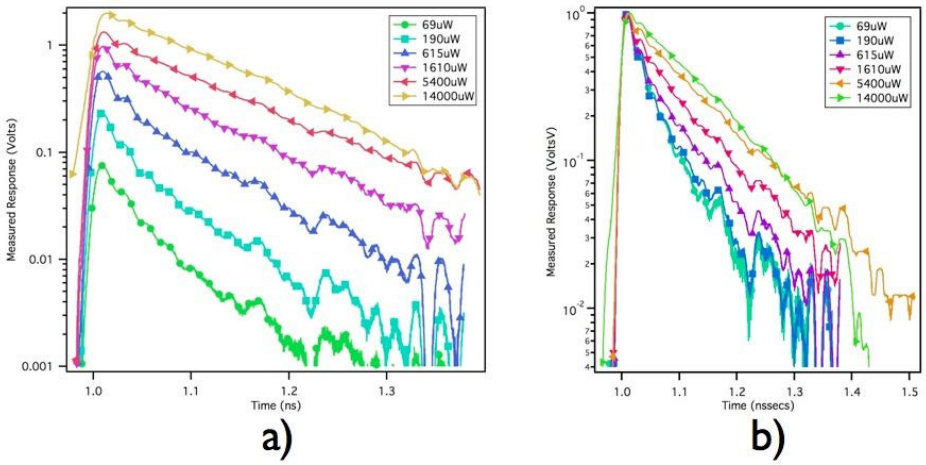

Figure 3.22: Time response of the Bragg device as a function of incident power, the incident wavelength was 830nm a) As-measured response b) Normalized Response

greatly but still allows for qualitative evaluation of fall times and the long time scale time response using fitting routines.

3.9.4 Higher Power Time Response

Fig 3.22a) and b) shows the as-measured and normalized response of the Bragg Reflector device with increasing incident power respectively. The response remains uniform and the increase power increases the overall peak height and lengthens the response time but does not change the overall shape of the response curve. The story for the device without a Bragg reflector however is significantly different.

As shown in Fig 3.23, as the incident power increases the response develops a knee, which forms into a long tail. Fig 3.23a shows the as-measured response curves, while Fig 3.23b provides normalized traces to more easily distinguish the change in the response shape. Deceiving is the fact that this tail develops at approximately 20% of the peak value, meaning reporting the full width half max value of this device would not indicate its true speed.

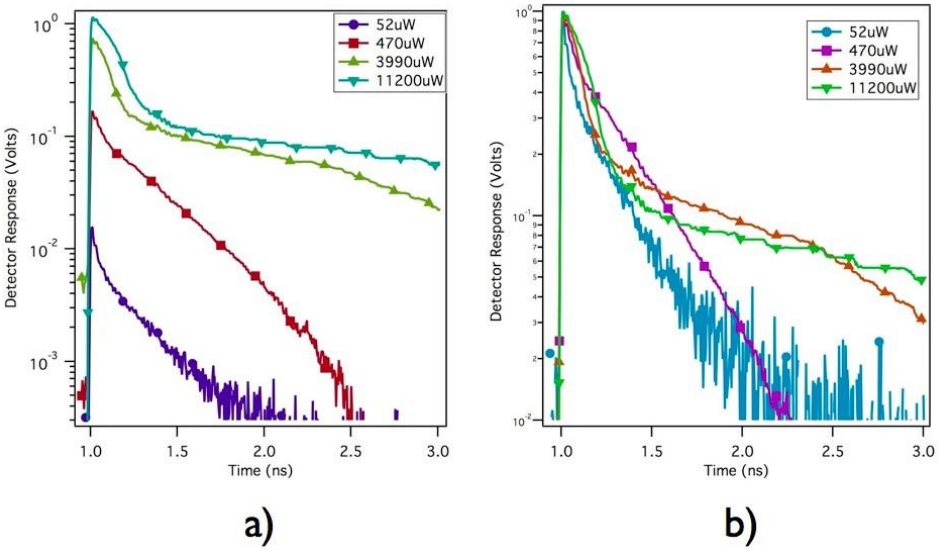

Figure 3.23: High speed response of device without Bragg reflector a) as measured b) normalized

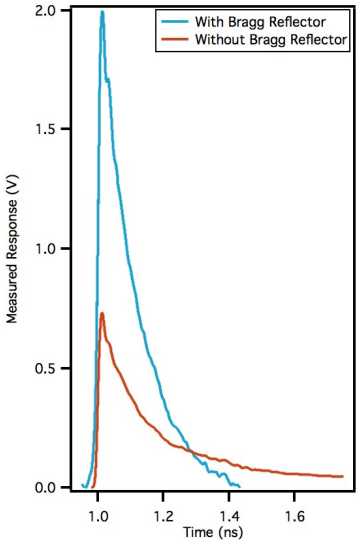

Figure 3.24: High Power response of devices a) Linear Vertical Scale b) Log Vertical Scale

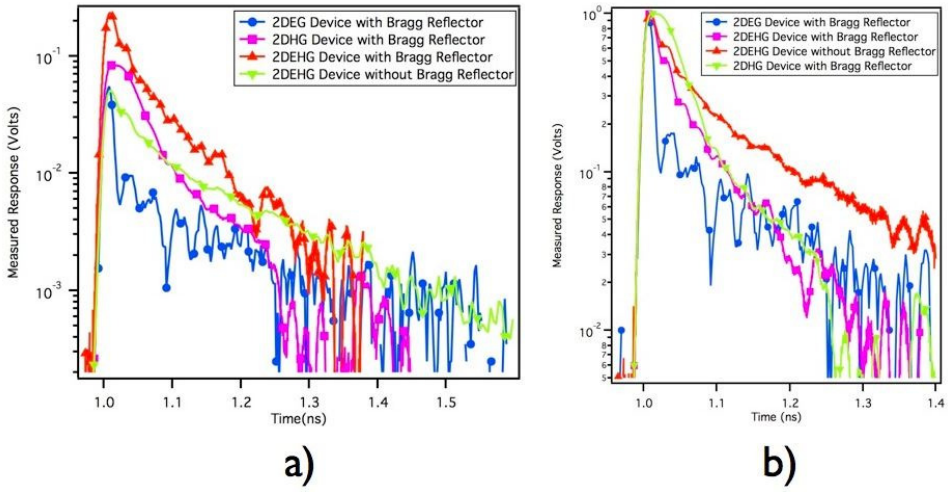

Figure 3.25: High speed response of several photodetector types a) As Measured b) Normalized

Fig 3.24 shows comparison of the responses at higher powers, clearly indicating the difference in the responses. Despite the large peak value of the Bragg device, the fall time to zero remains considerably faster. In order to understand the origin of this difference we can look at similar devices with quantum wells and incorporated Bragg reflectors.

Fig 3.25 shows a set of traces from several different high-speed photo detector devices that have been fabricated and tested in a similar way to the devices presented here. The devices include a two-dimensional electron gas based MSM and a two-dimensional hole gas based MSM. At low power all responses appear somewhat similar in shape, the variation in peak height can be attributed to the slightly different incident powers for each trace, no low power traces of identical power for each device type were available. Fig 3.25b shows the normalized traces, showing some variation, particularly in the 2DEG device, however qualitatively they are very similar in shape and response. Fig 3.26 shows only the 2DEHG with and without Bragg and a 2DEG with Bragg device. Here we can begin to see the benefit added due to both the

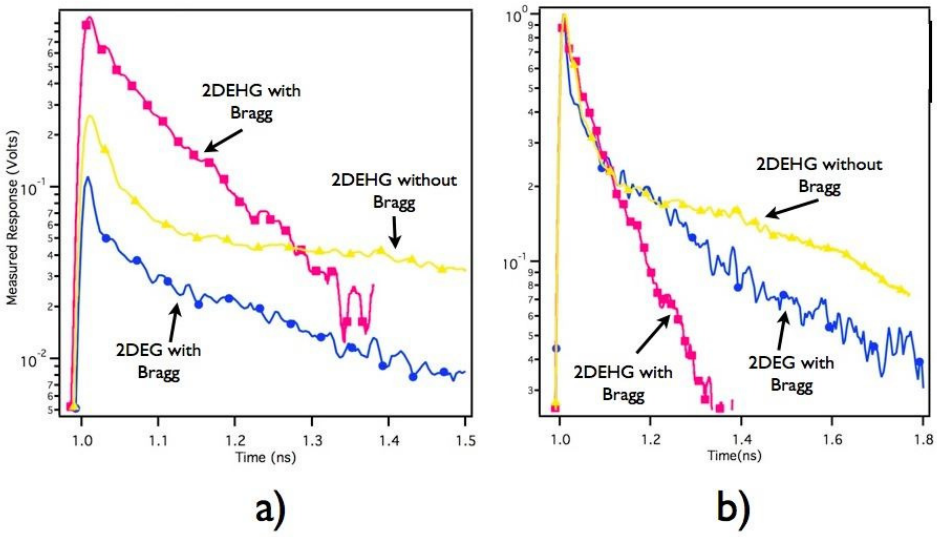

Figure 3.26: Comparison of the high speed response at higher powers of 2DEHG with Bragg, 2DEHG without Bragg and 2DEG with Bragg a) As measured b) Normalized to peak

presence of the 2DEHG and the Bragg reflector. The 2DEHG without a Bragg reflector shows the longest tail, though its slope indicates that it has a fall to zero time on the same order of the 2DEG device shown. The 2DEHG with Bragg clearly shows the fastest fall time and no shape change at higher power. This is a strong indication that the increased speed is not only attributed to the presence of the Bragg reflector, as the 2DEG also contains a Bragg with similar materials. Instead it demonstrates strong evidence that the combination of the Bragg with the dual quantum well structure offers the possibility to eliminate the long tails in the photodetector response.

3.9.5 Response Dependence on Wavelength

Fig 3.27 shows the detector peak height as a function of the incident wavelength. The device without a Bragg reflector shows a somewhat uniform response across all wavelengths measured, while the Bragg device shows a distinct peak at 836nm in

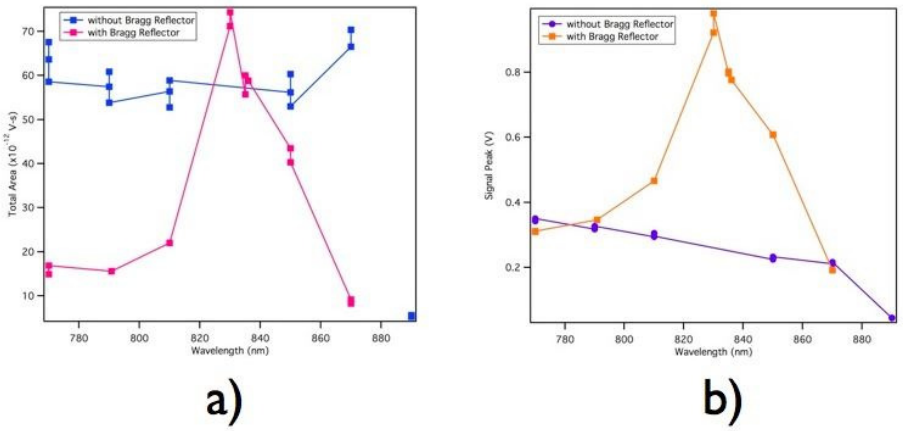

Figure 3.27: a) Total area under response curve as a function of incident wavelength b) Peak value of response as a function of incident wavelength

both the total area under the response trace and the peak value of the response. This peak is 10nm different from that found in the DC Photoresponse results. This discrepancy may be due to poor calibration on one or more setups, though from the data the suspicion is on the source for the DC measurements. The 850nm laser showed a smaller response of the Bragg devices, which is confirmed here. At this wavelength the peak height in the Bragg device is significantly larger, while the total area under the trace is smaller than that of the device without a Bragg reflector, confirming the results shown earlier for the DC photoresponse. For the DC response, the total generated current is measured which is comparable to the area beneath the high-speed trace.

3.9.6 Analysis of Fall Times

Fig 3.28 plots two separate metrics for evaluation of the fall time of the devices. For each trace the fall time to 20% of the peak value and fall time to 5% of the peak value is plotted as a function of incident power. The Bragg reflector shows a

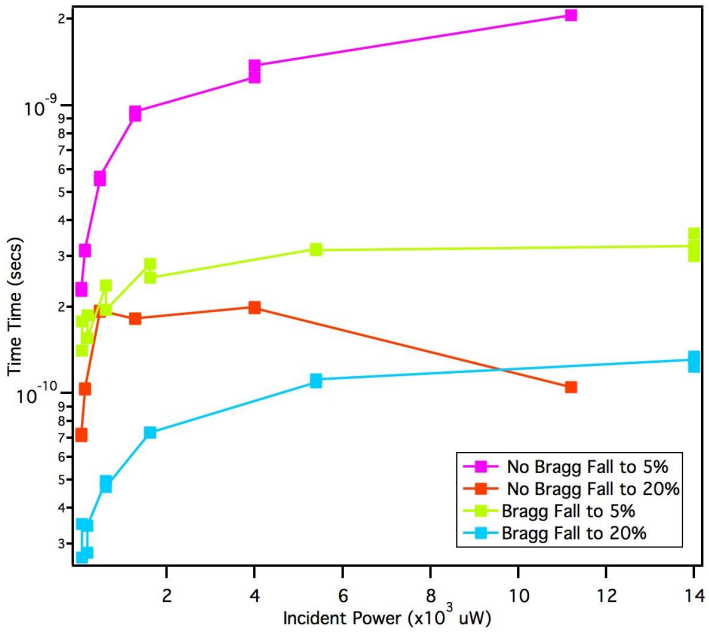

Figure 3.28: Fall times as a function of incident power for the Bragg device and the device without a Bragg reflector

consistent and slow increase of these parameters while the device without a Bragg shows a distinctly different behavior. The fall time to 20% actually decreases above a certain power, at higher powers showing a faster fall time than the Bragg devices. The fall time to 5% however, a measure of the tail length continues to increase to roughly 4 times that of the Bragg device at 11mW of incident power.

3.9.7 Effects of Geometry

Previously we have reported on the effect of geometry of the interdigitated fingers on the time response. In 2DEG and 2DHG devices it has been reported that only a small difference can be seen in the response of the fingers separated by 2um and 4um, indicating that the time response may not be time transit time limited in these devices[89] . Fig 3.29 shows a plot of time response at similar powers for 5 different

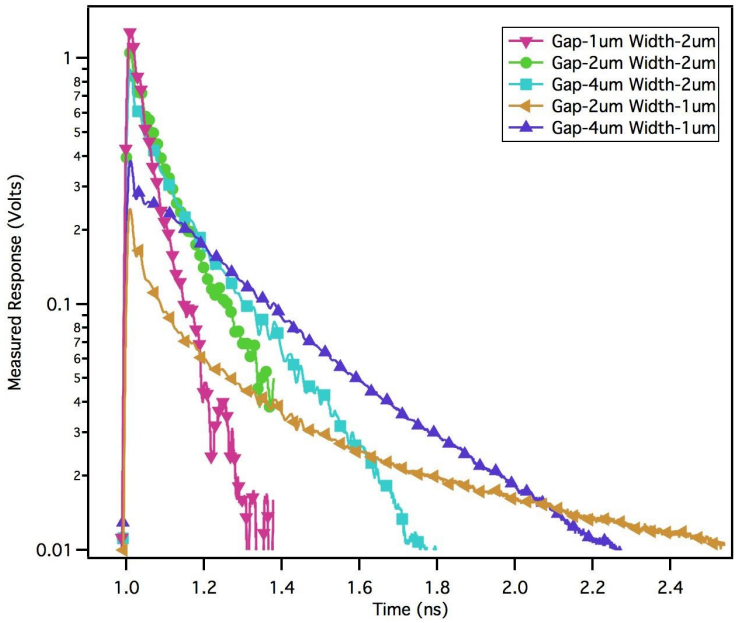

Figure 3.29: High-speed response of different geometries on a Bragg device. Incident wavelength is 830nm and incident power is 1mW

device geometries on the Bragg device. In these devices a clear difference can be seen in response times. The two devices with narrower fingers (1um) show a smaller peak and a long tail, similar to that seen in the non-Bragg and non-2DEHG devices. The device with 2um fingers and 1um finger spacing, clearly shows the highest peak and fastest fall times. The two devices with 2um and 4um finger spacing then show a similar response, suggesting that beyond a certain spacing these devices may not longer be transit time limited, as observed with previous device sets.

Fig 3.30 shows that the overall area beneath the trace, a measure of the amount of total charge collected as a result of the incident laser pulse, for different geometries in the 2DEHG devices. At higher powers the devices without a Bragg reflector are collecting more charges, possibly due to collection of carriers absorbed in the substrate.

Fig 3.31 shows the fall time to 10% of the peak value for several different geometries

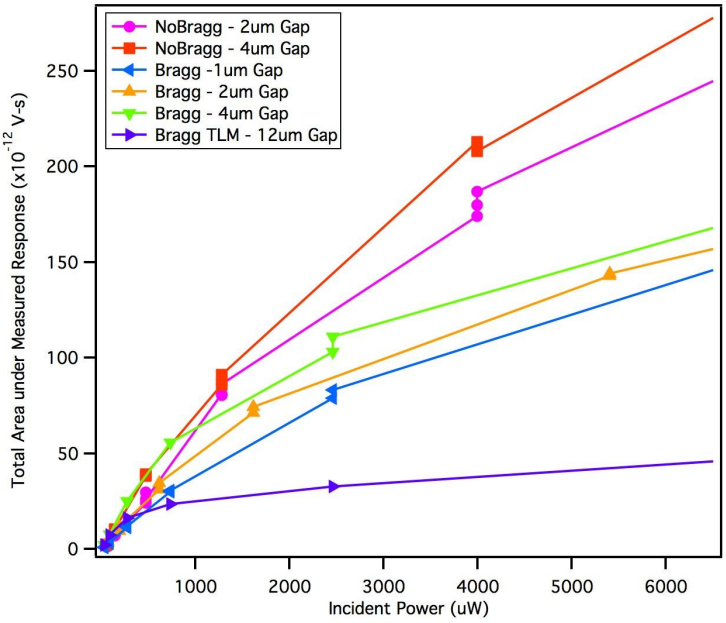

Figure 3.30: Total area under response as a function of incident power for different device geometries

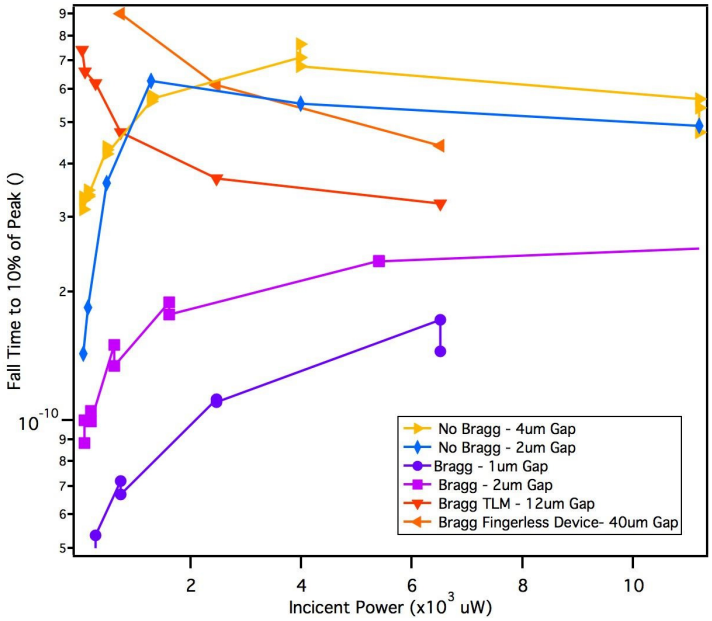

Figure 3.31: Fall time to 10% as a function of incident power for different geometries

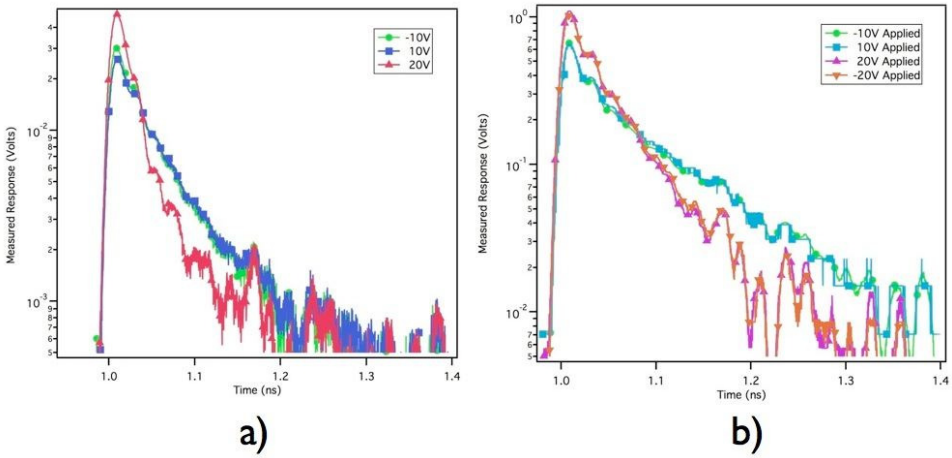

Figure 3.32: Time response of a Bragg device at different bias values for a) 2um gap device b)4um gap device

with and without a Bragg reflector. The smaller gap Bragg devices show the behavior seen previously, a slow increase in the fall time as power increase. The larger gap devices (TLM 12um, CZ4 40um) actually show a decrease as the power increases. The devices without Bragg again show an increase initially and then begin to decrease at higher powers, similar to the fall to 20% shown previously indicating again a narrowing of the initial pulse at higher powers and an increase in the long tails portion of the collected carriers.

3.9.8 Effect of Bias

The effect of the applied bias was also investigated for these devices, with the expectation that increasing the bias should create a faster response by increasing the electric field within the device.

Fig 3.32 shows the high-speed results under varying bias for two Bragg Device geometries. In both cases the higher absolute value of bias increase the peak value and decreases the fall time indicating the response is heavily dependent on the field

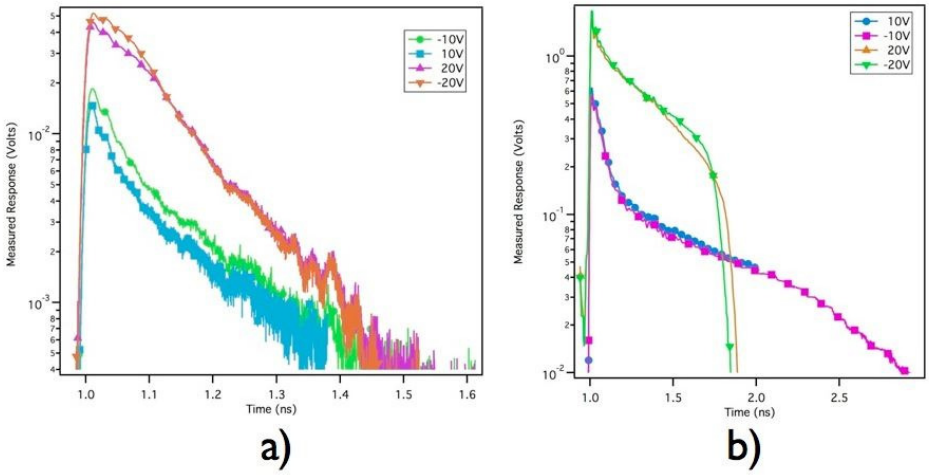

Figure 3.33: Time response of a device without a Bragg reflector at different bias values a)2um gap device b)4um gap device

generated by the applied bias.

Fig 3.33 however shows the effect of bias on the response of the device without a Bragg reflector. In this case the peak value increases substantially with increased bias but so does the fall time and the total area beneath the trace, unlike with the Bragg devices. These results again present strong evidence that the higher bias is allowing carriers generated in the substrate to be collected, increasing the area under the response as the internal field extends further into the substrate. Fig 3.33b is even more interesting. The abrupt change in shape and elimination of the tail may be correlated to the results seen in the photocurrents wavelength dependence, Fig 3.11. In these results, it appeared that at 15V bias the InGaAs no longer participated in conduction, seen by the loss of photoresponse in the 900-950nm region.

3.9.9 Discussion of Results

The high-speed results provide substantial evidence that both the Bragg reflector and the 2DEHG structure are enabling faster response times in the photodetectors.

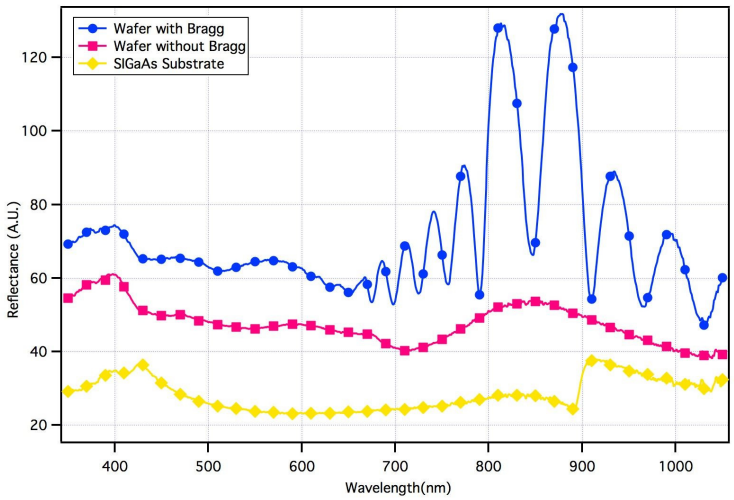

Figure 3.34: Reflectance measurements on 2DEHG with Bragg, 2DEHG without Bragg and semi-insulating GaAs. Traces are offset for ease of viewing.

The origins of the slower response in the 2DEG and the device without Bragg are not completely clear though considerable evidence suggests a contribution from the substrate. The 1um gap, 2um finger Bragg device had the fastest response of any device studied so far, including 2DEG and 2DHG devices reported previously.

3.10 Optical Characterization

In order to gain more insight into the possible origins of the different behaviors seen in the two structures, the wafers were interrogated optically with reflectance and photoluminescence measurements. Optical spectroscopy offers insight into the band diagram and location of carriers within the structure.

3.10.1 Reflectance

Fig 3.34 shows the reflectance of the 2 wafers along with that of a semi-insulating GaAs substrate. The Bragg wafer demonstrates the expected oscillating peaks due

to the presence of the Bragg reflector. It shows a Bragg reflector tuned to near 840nm and several other frequencies that may exhibit a Bragg resonance. The Bragg effect clearly dominates the resulting reflectance. For the device without a Bragg reflector we see a somewhat unusual result. There is a broad reflectance peak at around 840nm and no indication of the onset of absorbance, as seen near 880nm in the semi-insulating GaAs reflectance. The device without a Bragg shows a rather flat reflectance with a somewhat unusual character to it.

3.10.2 Calculation of Expected Radiative Transition Energies

Radiative recombination occurs within the semiconductor structures as a result of the excitation of electron-hole pairs within the material. This excitation is an incident laser with energy larger than the band gap of the material. Based on the energy band diagram we can make a prediction of the peaks that may be present in a photoluminescence (PL) signal by observing the possible radiative transitions that are possible within the material. We can also make some predictions on the expected shape and relative magnitude of these peaks by anticipating where photo-generated carriers will collect within the device before they recombine. The presence of electric fields separate electron-hole pairs within the absorption region and moves them to their respective wells. This creates a situations where the electrons and holes are spacially separated, thereby reducing the probability of recombination. The magnitude of the photoluminescence signal will depend on the number of minority carriers present or passing through the region of the quantum wells. The position of a photoluminescence peak can be predicted using a simulated energy band diagram. The line shape and relative height of a peak can be predicted by understanding what determines the probability that an electron and hole will recombine in a particular layer, which is determined by the density of both carriers in that particular region.

Using the Fermi level and density of states we can make a prediction of what the relative height and width of a particular peak may be. The photoluminescence line shape can be described by:

$$I(h\nu) = A \times g(E) \times f_h(E) \times f_e(E) \tag{3.1}$$

where the response, I, is given as a function of energy. A is the optical matrix describing the allowed optical transitions, g(E) is the joint density of states, f(E) describes the hole and electron distributions as a function of energy. Table 3.1 shows a list of

Peak	Position	Shape
InGaAs hh1	1.29eV	Gauss
InGaAs hh2	1.33eV	Gauss
AlGaAs bulk	1.80eV	Gauss - broadened
AlGaAs e1	1.85eV	Gauss - broadened
GaAs bulk	1.42eV red shifted	Lorentzian
GaAs e1	1.47eV	Gauss - broadened
GaAs e2	1.55eV	Gauss broadened

Table 3.1: Calculated photoluminescence Emission Peaks

possible and expected peaks based on the energy band diagram of the structures. We assume that the first two energy levels in each well may participate in recombination, with the predicted peak from the InGaAs wells near energies of 1.29eV and 1.33eV. The larger energy well should be significantly smaller in height in non-saturation conditions due to the position of the Fermi level within the material. With the GaAs we can expect 4 possible peaks. The first two arise from the first two energy levels within the electron well, with values of 1.47eV and 1.55eV. The third peak may arise from carriers combining within the GaAs absorption region. Within this region is a

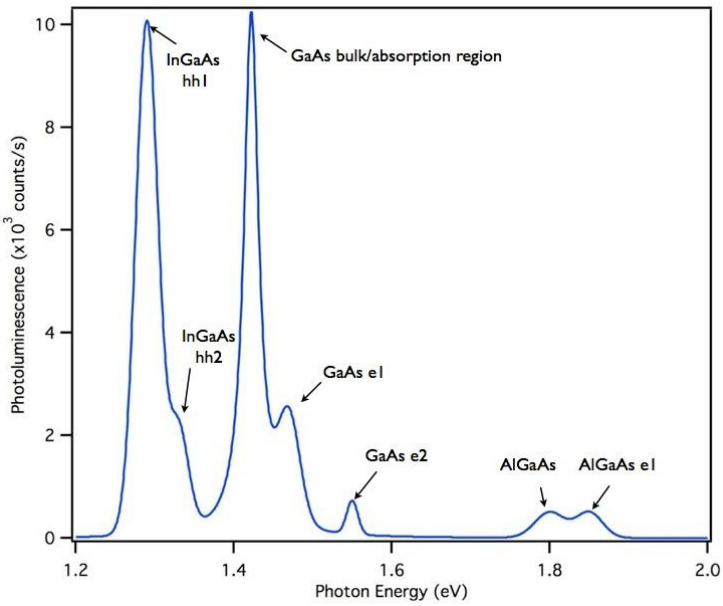

Figure 3.35: Predicted photoluminescence spectrum based on simulated band structure

very large electric field that is expected to red shift (decrease in energy) the photoluminescence emission [41]. This effect is due to the strong bending of the bands. The final possible peak is from the GaAs substrate, which at room temperature can be expected to be 1.42eV, the band gap of GaAs. For the AlGaAs, there are also two possible peaks. One for the bulk AlGaAs with a Al content of 30% and one from the confined states within the delta doping regions. Both of these states would shift the AlGaAs emission to 50meV higher energy. An ad hoc preliminary prediction of the measured photoluminescence spectrum is shown in Fig 3.35 The prediction is based on the simulated band diagram for peak position and the literature and a qualitative use of Equation 1 to predict the widths and shapes of the peaks. The energy separation of the wells is twice that of kT at room temperature, so we can expect to be able to distinguish individual peaks even at non-cryogenic temperatures.

3.10.3 Optical Measurement Setup

The photoluminescence data was taken on a home built system. The illumination is provided by a Argon-ion laser using the 488nm laser line unless otherwise stated. For some measurements a tunable Ti-Sapphire laser was used, with a tunable range of 950 to 750nm. The laser is focused through an objective into a temperature controlled vacuum chamber that contains the sample to be measured. The sample can lie flat or be tilted relative to the incident beam in order to reduced Rayleigh scattering and remove the laser line from the measured spectra. The photoluminescence signal is collected through the same objective in a backscatter geometry and focused onto the collection device. Spectra were collected with a Comet Spectrometer, with a full range of 1100nm to 200nm and an array of CCD detectors providing approximately 1nm resolution and also with a U100 Yobin Jvon double monochromator with a range of 900-300nm using a water-cooled photomultipier tube for collection. The resolution of the monochromator varies depending on the operating conditions but was also used with a minimum resolution of 0.1nm. The samples were cooled with liquid nitrogen and liquid helium, with a built in stage heater allowing continuous control of the sample temperature from 4.2K to 325K. The spot size of the laser is measured to be approximately 25um in diameter at its minimum. The importance of the beam focus will be discussed in a later section.

3.10.4 Photoluminescence Results on Sample without Bragg

A comparison of the actual measured photoluminescence signal to the predicted signal is shown in Fig 3.36. The measurement was taken at an incident power of 50mW at room temperature. The actual and predicted photoluminescence spectra match up fairly well at first glance. Using the peak fitting routine in Wavemetrics IGOR data analysis program, we can fit the predicted peaks to the actual measured

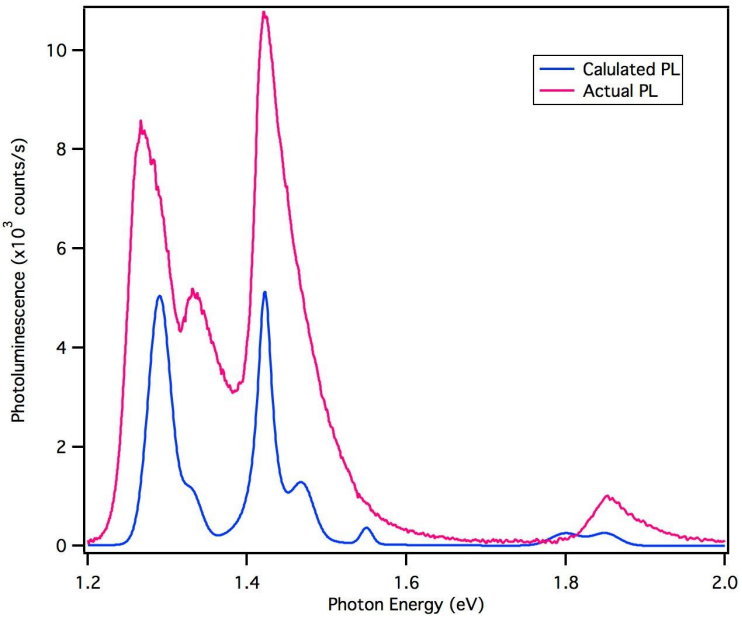

Figure 3.36: Comparison of calculated and measured photoluminescence peaks on the substrate without a Bragg reflector at 50mW incident power

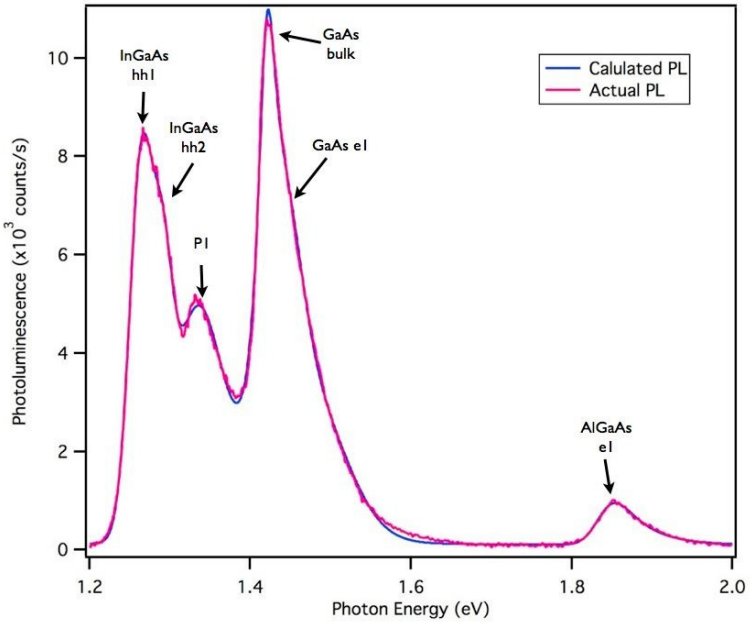

Figure 3.37: Calculated and fitted photoluminescence spectrum for the wafer without a Bragg reflector. Peaks derived from the energy band simulation are marked accordingly

photoluminescence spectra. The fitted spectrum is shown in Fig 3.37. In fitting the data a new peak arises that was not in the prediction, which we will label as P1. This peak lies near the predicted InGaAs peaks but is larger than what would be expected if it was attributable to a higher energy level in the InGaAs well. A stronger possibility is a momentum-assisted recombination of carriers from the GaAs recombining with holes in the InGaAs well. The measured energy, 1.33eV is close to the expected value of this phonon-assisted transition after the band diagram has been adjusted to match the measured InGaAs values. The predicted and actual peak values are shown in Table 3.2. These transitions are illustrated in Fig 3.38. An electron from the GaAs

Peak	Simulated Position	Actual Position
InGaAs hh1	1.29eV	1.27eV
InGaAs hh2	1.33eV	1.29
AlGaAs bulk	1.80eV	-
AlGaAs e1	1.85eV	1.85eV
GaAs bulk	1.42eV red shifted	1.42eV
GaAs e1	1.47eV	1.46eV
GaAs e2	1.55eV	-
P1	-	1.33eV

Table 3.2: Calculated and Measured photoluminescence Peak Energies for Sample without a Bragg Reflector

region recombines with the a hole in the InGaAs well. Several factors would indicate that this is a probable transition. Due to the thickness of the InGaAs layer confined states exist in both the valence band and the conduction band. The conduction band has one energy level that due to the strong electric field in the region lies close to the GaAs conduction band edge. This decreases the barrier for electrons to escape from the well. Also with a single energy level, at the higher energy illumination the well

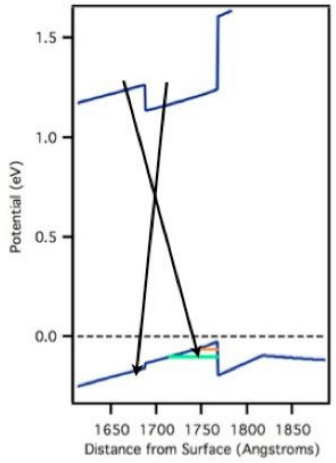

Figure 3.38: Possible phonon assisted transitions between the GaAs and InGaAs regions

may become saturated, easily allowing electrons to spill into the GaAs and providing an opportunity for recombination as they are swept to the electron well by the built in field. The electric field also shifts the wave functions of the confined carriers, decreasing the spatial overlap of electrons in the InGaAs conduction band and holes in the InGaAs valence band.

Another interesting observation is that there is no detectable red shift in the GaAs photoluminescence emission, as would be expected if emission was originating from the GaAs absorption region where a strong electric field is present. There are two possible explanations for this observation, the first being that the shift is not strong enough to distinguish under room temperature conditions. The other explanation is that the signal originates solely from the substrate. The latter explanation may provide some insight into the results of the high-speed measurements.

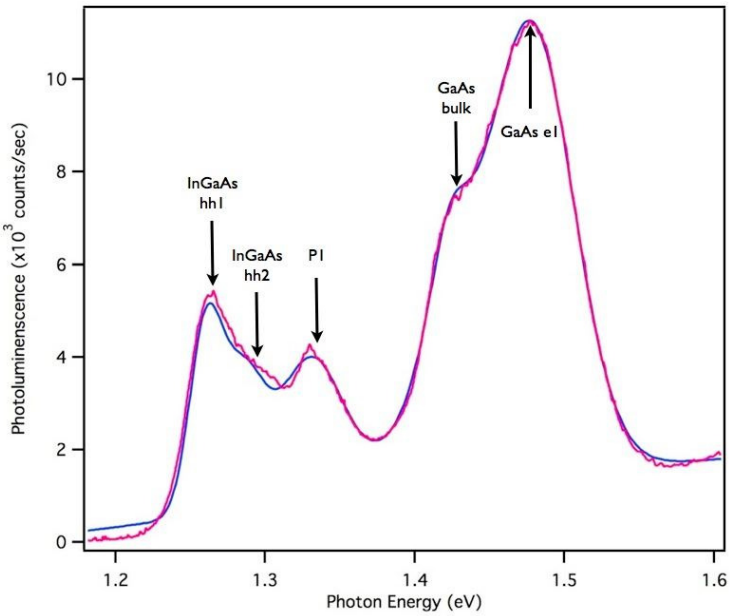

Figure 3.39: Curve fitting on photoluminescence from substrate with Bragg Reflector

3.10.5 Photoluminescence Results on Sample with Bragg

The same routine was than carried out for the measured photoluminescence of the sample with a Bragg reflector at under equal conditions. The results are shown in Fig 3.39.

The InGaAs peaks remain at the same position and approximately equal intensities, as well as peak P1 that was seen in the wafer without the Bragg reflector. There is a significant difference however in the peaks attributed to transitions within the GaAs region. In the device with the Bragg we see a dominant peak at the e1 energy level and a shoulder created by bulk GaAs peak. This peak lies at 1.48eV or 838nm. The high-speed measurements indicated the highest Bragg efficiency at 836nm, near the energy of the observed peak. These traces do not include the AlGaAs peak shown in the substrate without a Bragg reflector. If we expand the energy plot to include the expected AlGaAs energies, we can see the effect of the Bragg reflector on the

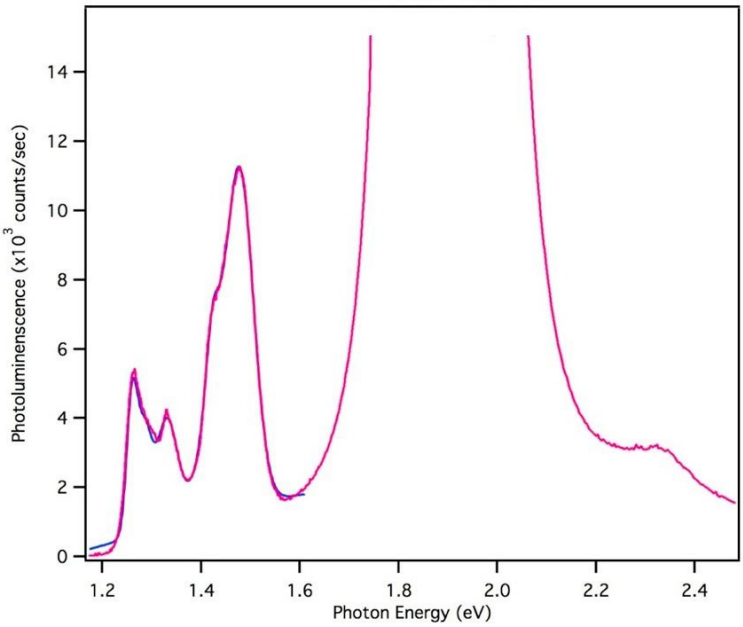

Figure 3.40: Fitted Bragg results showing full spectrum, fitting to the AlGaAs peak is not possible due to the saturation of the detectors

photoluminescence signal, Fig 3.40

The AlGaAs peak dominates the entire signal. 488nm is equivalent to 2.54eV, allowing absorption for the AlGaAs layers within the Bragg reflector. Carriers generated within the Bragg layers are not subjected to an electric field and confined to the AlGaAs layers by the neighboring AlAs. The electron-hole-pairs generated are left to recombine emitting 1.8eV photons. The 20 Bragg layers make AlGaAs the dominant material by volume within the growth region. Also present is a higher energy shoulder at 2.3eV, which may be attributed to phonon-assisted recombination between the AlAs conduction band and the AlGaAs valence band. Table 3.3 shows the predicted and measured peak values.

Fig 3.41 shows the AlGaAs peak as a function of power for the Bragg wafer. The peak dominates the photoluminescence spectrum at all incident powers. The emergence of the peak at 1.48eV (838nm) also matches well with the measured reflectance

Peak	Simulated Position	Wafer without Bragg	Wafer with Bragg
InGaAs hh1	1.29eV	1.27eV	1.27eV
InGaAs hh2	1.33eV	1.29eV	1.29
AlGaAs bulk	1.80eV	-	-
AlGaAs e1	1.85eV	1.85eV	1.85eV
GaAs bulk	1.42eV (red shifted)	1.42eV	1.42eV
GaAs e1	1.47eV	1.46eV	1.48eV
GaAs e2	1.55eV	-	-
P1	-	1.33eV	1.33eV
AlGaAs Shoulder	-	-	2.33eV

Table 3.3: Tabulated predicted and measured peak values for substrate without Bragg and with Bragg

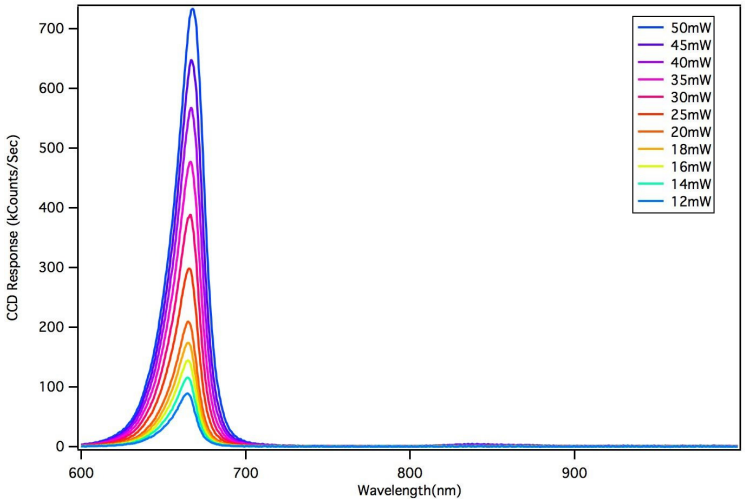

Figure 3.41: Photoluminescence of Bragg Device as a function of intensity

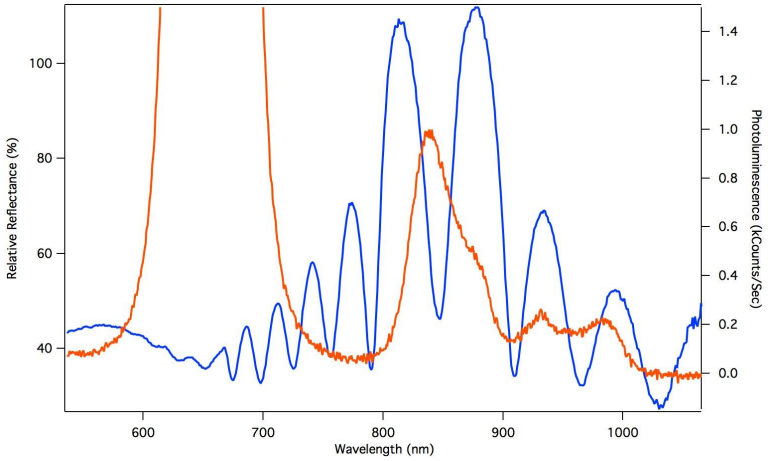

Figure 3.42: Simultaneous plot of reflectance and photoluminescence from the Bragg substrate

data of the Bragg substrate. The GaAs emission peak falls into one of the sidebands of the reflection, indicating that no Bragg enhancement occurs, as shown in Fig 3.42.

The electron well e1 peak signal collection is possibly enhanced by the presence of the Bragg reflector. This enhancement is further verified by collecting photoluminescence spectra at different sample angles. The Bragg reflectors wavelength peak is a function of the incident angle. Collecting photoluminescence at different angles demonstrated a noticeably shifted peak. This will be seen more clearly in the photoluminescence under varying temperature data that will be presented in a later section. The alternative possibility is that since emission from the absorption region comes from the electron well in the GaAs, the carriers absorbed in the Bragg reflector move into the GaAs region and recombine while in the electron well.

Alternatively, carriers in the substrate without a Bragg remain and recombine in the substrate. This is doubtful however as no change is seen in the InGaAs peaks.

Fig 3.43a shows a plot of the collected photoluminescence signal from a Bragg

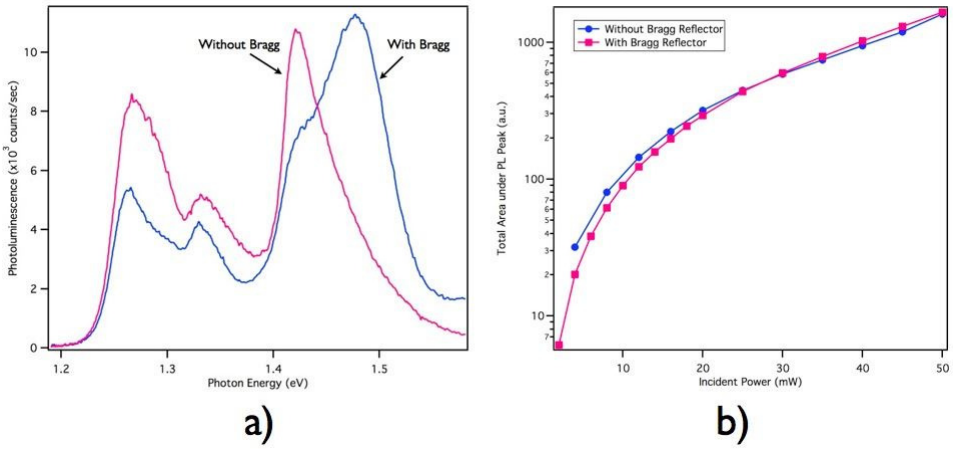

Figure 3.43: a) Photoluminescence trace from the Bragg and without Bragg substrate b) Area under the photoluminescence trace as a function of power for both substrates

substrate and one without a Bragg reflector. The peak positions in the InGaAs well, P1 and the bulk GaAs emission line up well. Interestingly, the total number of collected photons remains very close for both samples, as seen in Fig 3.43b. This implies that the samples are absorbing a similar amount of energy near the surface and recombination is occurring in different regions of the sample. Also of interest is the relative heights of the bulk GaAs peak, the sample without a Bragg reflector is only slightly higher, suggesting not all of the signal is originating from the substrate. As a comparison, Fig 3.44 shows the two photoluminescence plots with the addition of a photoluminescence response from a simpler heterostructure containing an electron quantum well at the interface between $Al_0.3Ga_0.7As$ and GaAs. The plot matches well with the GaAs peak for the substrate without a Bragg reflector. It also illustrates the level of complexity introduced by the addition of the hole well within the sample.

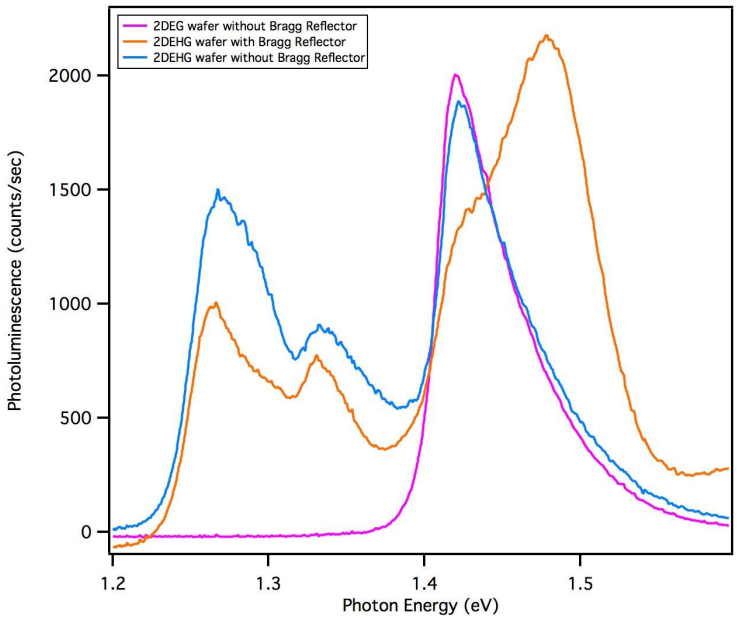

Figure 3.44: Photoluminescence response of 2DEHG with and without Bragg and 2DEG wafer

3.10.6 Analysis of Photoluminescence with Varying Incident Power

The aim of this work was to interrogate the substrate at higher powers and room temperatures, comparable to the conditions experienced during the high speed testing. Fig 3.45 provides a plot of the curve fit peak energies as a function of the incident intensity.

The relatively flat bands imply that the laser is not heating the substrate significantly, with the InGaAs hh1 peak decreasing in energy 5meV at the highest incident power. Fig 3.45b shows the close up of the AlGaAs peak energy as a function of incident power. As an isolated peak it gives the cleanest fit and best indication of total substrate heating. Fig 3.45d,c also provides a comparison of the plot positions of the two wafers, showing that despite differences in amplitude, the peak positions are relatively similar. The curve fitting allows us to plot several aspects of the col-

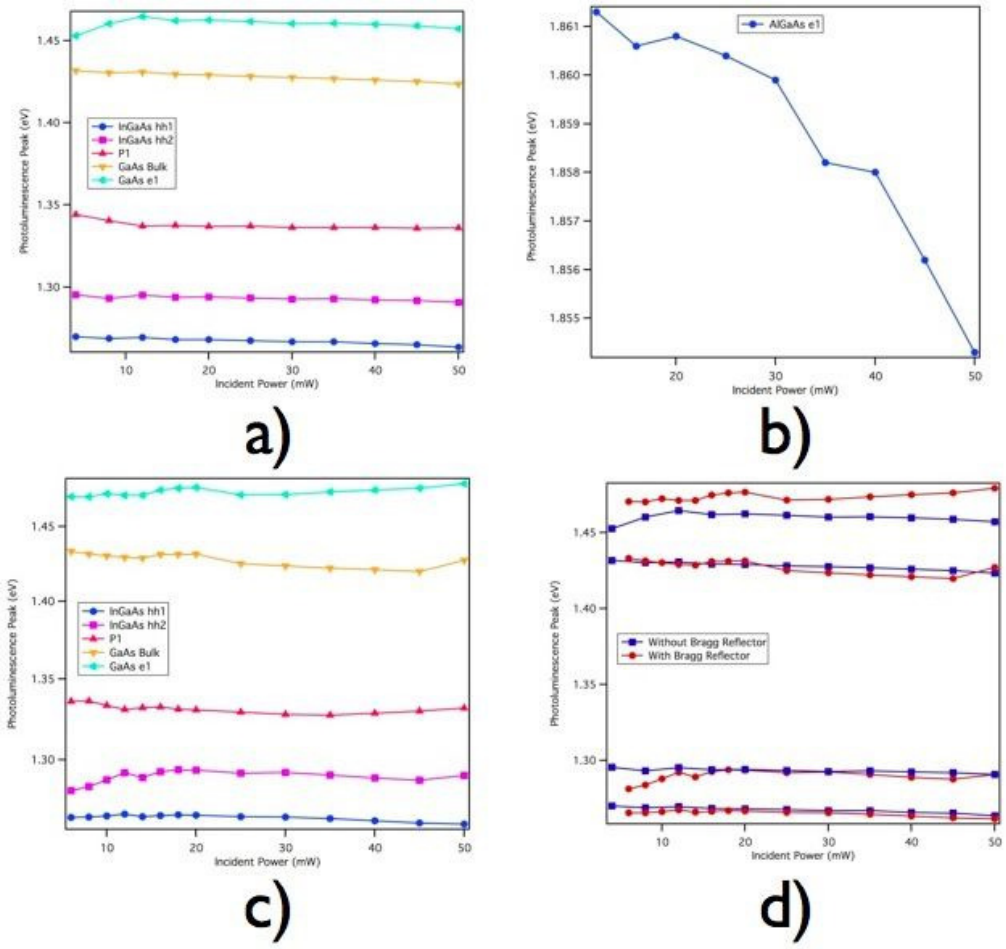

Figure 3.45: Peak energies as a function of incident power for a)substrate without Bragg b) AlGaAs peak energy in Device without a Bragg Reflector c)substrate with Bragg d)comparison

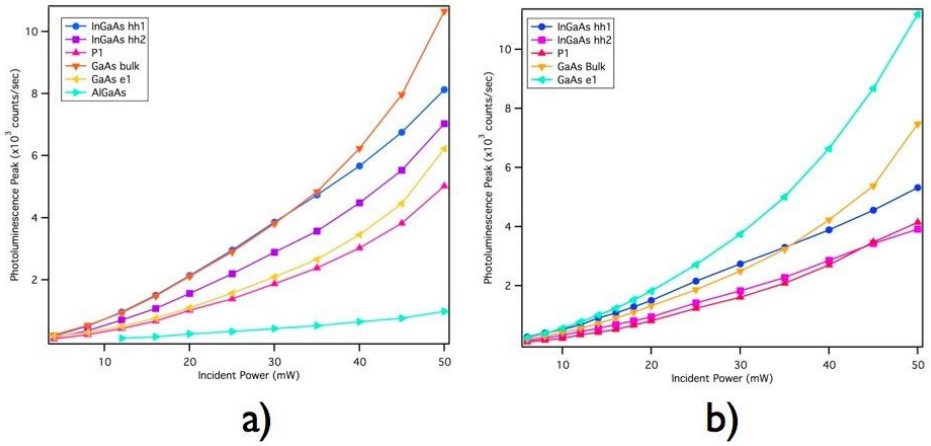

Figure 3.46: Individual peak heights as a function of power for a) sample without Bragg b)sample with Bragg

lected photoluminescence signals and compare how the signal changes as a function of power.

Fig 3.46 shows a plot of the height of the observed peaks as a function of incident power for the sample without Bragg (Fig 3.46a) and with Bragg (Fog 3.46b). All peaks increase at a relatively uniform rate in both substrates with the GaAs peaks beginning to increase faster at higher powers in the Bragg sample.

3.10.7 Analysis of Photoluminescence at Varying Temperature

In order to investigate the origin of the unknown peaks, the photoluminescence was taken as a function of temperature. Different recombination processes should show different temperature signatures and this method should distinguish between peaks enhanced by the Bragg reflector and peaks generated as a result of recombination within the material. Phonon assisted recombination should also decrease with temperature, as the phonon density declines therefore becoming less likely to participate in a recombination process.

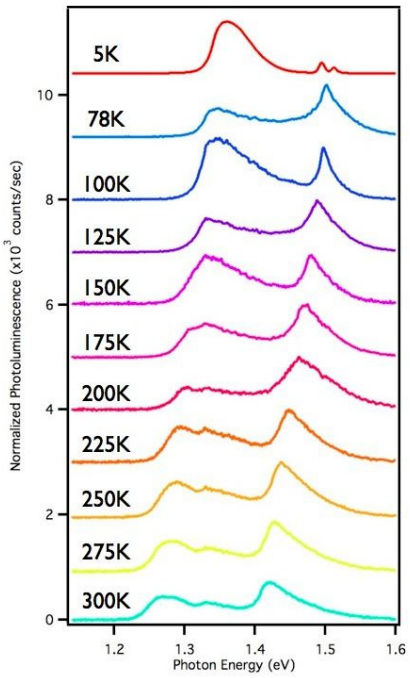

Figure 3.47: Photoluminescence traces at varying temperature for wafer without a Bragg reflector

Fig 3.47 plots the measured photoluminescence traces at decreasing temperature for the wafer without a Bragg reflector. The figure shows a consistent shift of the GaAs peak and the InGaAs well peak. Interestingly, the P1 peak does not appear to shift with temperature and joins with and becomes indistinguishable from the InGaAs peaks around 175K. This is an unexpected result. A phonon-assisted recombination should decrease in intensity as a function of temperature, but as the band gaps of the GaAs and InGaAs increase, so should the peak position. The peak positions as a function of temperature are plotted in Fig 3.48 at 40mW and 10mW incident power. Guidelines of the expected GaAs and InGaAs bandgaps are included as a reference. The peaks at 40mW show even more interesting results. The P1 peak appears to be very slowly varying with temperature. Plotting its behavior becomes difficult with the emergence of a new peak at 250K, with an energy around 1.4eV.

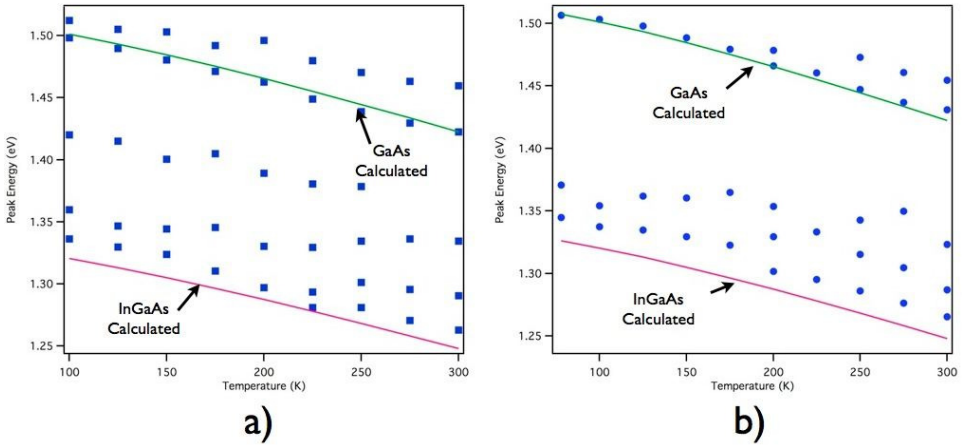

Figure 3.48: Peak energies as a function of temperature for wafer without Bragg. The solid lines are predicted band gap values for InGaAs, GaAs and AlGaAs

An artifact of the curve fitting can often be a perceived shifting of peak energy due to a change in the peak shape. While one can clearly see the curve fit is close and the P1 peak is easily visible in the photoluminescence traces shown previously, there is the possibility of generating slightly misleading data using this technique. The peak positions were also extracted by hand and produced very similar results however. A flat temperature response from the P1 peak and the emergence of a new peak, P2 at temperatures below 275K. The GaAs peak, InGaAs peaks and AlGaAs peaks follow an expected increase with decreasing temperature as shown in the figure. This same measurement was also performed on the Bragg wafer, with similar results.

Fig 3.49 shows a cascade plot of the collected photoluminescence as a function of temperature. The Bragg reflector substrate also shows the P1 peak flat temperature response, seen in Fig 3.50, as well as a somewhat flat response for the GaAs e1 emission peak position.

In this sample, P2 shows a similar flat response to temperature as well. With neighboring peaks, the problems with curve fitting can be increased significantly.

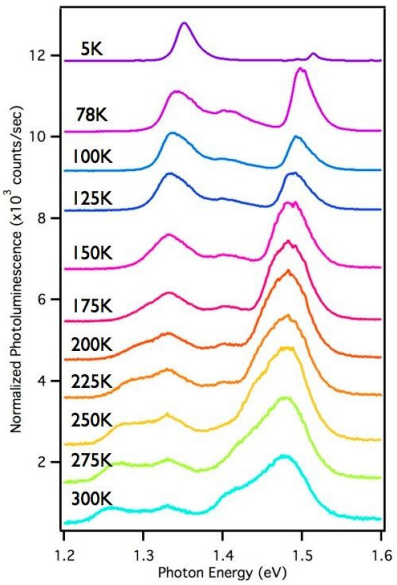

Figure 3.49: Photoluminescence traces at varying temperatures from Bragg wafer

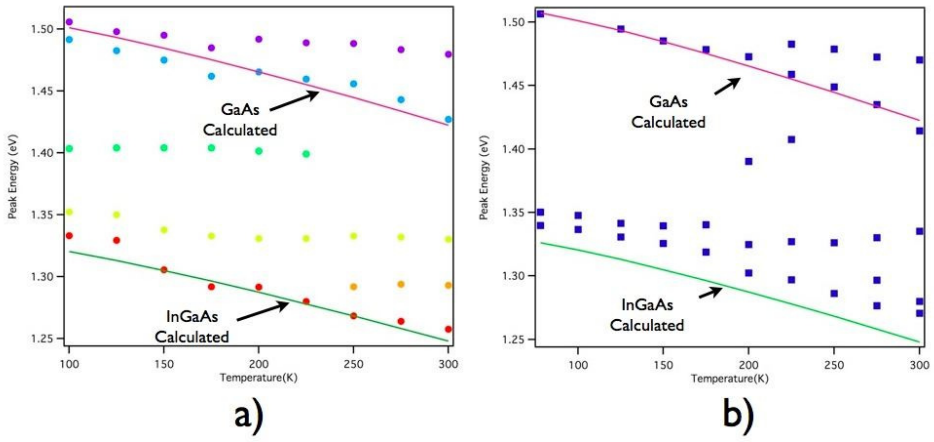

Figure 3.50: Peak energies as a function of temperature for wafer with Bragg. The solid lines are predicted band gap values for InGaAs and GaAs. a) 40mW incident power b)10mW incident power

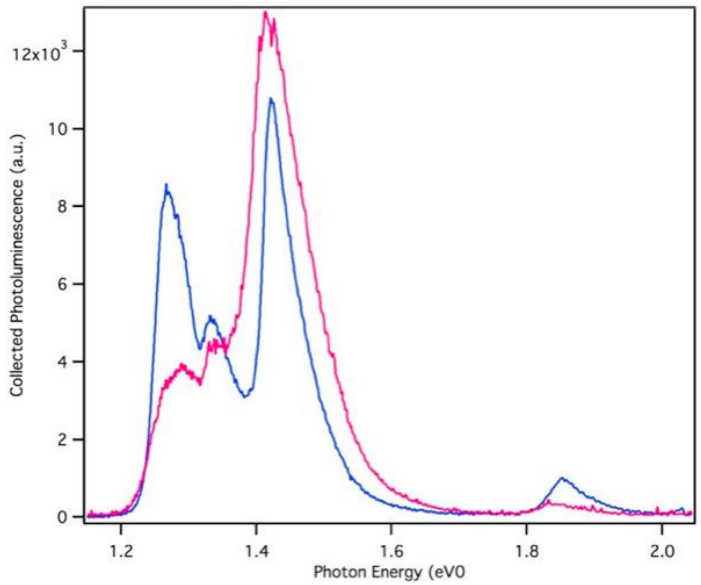

Figure 3.51: Photoluminescence response at two separate focal positions on wafer without Bragg. Incident power was 50mW

We can see some noise in the peak positions plot introduced as two peak energies approach each other due to the increased number of acceptable peak fits possible with the overlapping signals.

3.10.8 Photoluminescence Dependence on Focal Position

Thus far, we have only spoken of incident power and not the typically discussed intensity. At minimum focus the spot size is about 25um, with its size and shape varying greatly as a function of focal position. In the course of measurement of these samples, it was determined that focus played an extraordinarily large role in the photoluminescence spectrum collected. Not simply in the strength of the signal as might be expected but in the ratio of peak heights and at times the existence of peaks.

Fig 3.51 shows two photoluminescence spectra collected on the same sample, at

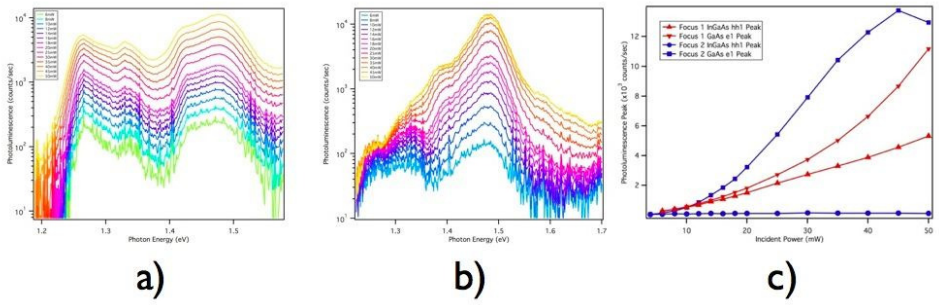

Figure 3.52: Photoluminescence response with increasing power at two different focal positions and 50mW powers. a) Focal Position 1 b) Focal Position 2

the same position but at two different focal positions. One can immediately see that the peak positions appear to remain the same but the ratio of the peak heights can become drastically different. The area under the traces also remains very similar at the same power. This role of the beam focus cannot simply be explained as a changing intensity on the wafer.

Fig 3.52a) and b) are plots of photoluminescence at varying incident power at two separate focal positions on the Bragg sample. In Fig 3.52a there is a uniform increase in the photoluminescence intensity across all wavelengths. In Fig 3.52b, the GaAs peaks increase at a much higher rate than the InGaAs peaks. Fig 3.52c plots these peak heights for both focal positions as a function of incident power, highlighting the large difference in behaviors.

At lower temperatures this effect can be even more striking, allowing focus to determine which peak dominates the photoluminescence signal. Fig 3.53 a and b are additional plots of photoluminescence spectra with increasing intensity at two different focal points. In a the InGaAs peak dominates, though the increase in photoluminescence remains somewhat uniform. In b the GaAs peak dominates and interestingly the P2 peak is also visible. At this focal position the InGaAs peak is largest at lower

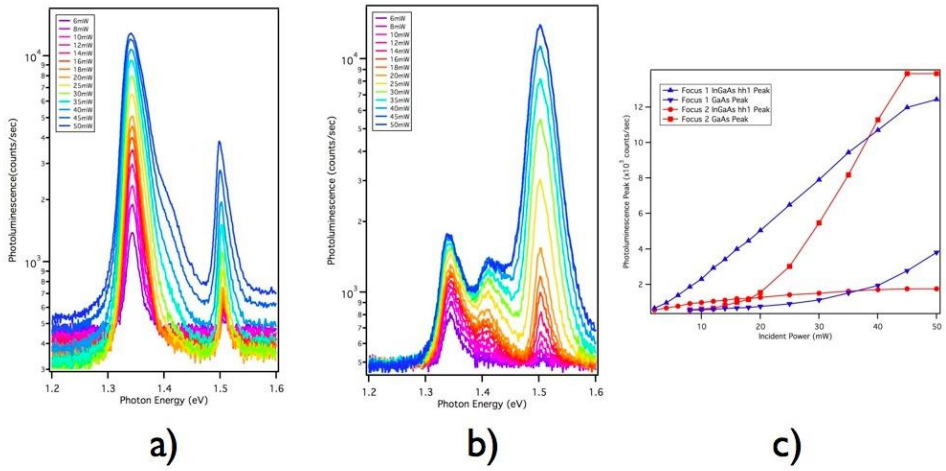

Figure 3.53: Photoluminescence response with increasing power at two different focal positions and 50mW incident power. The substrate was held at 78K. a)Focal Position 1 b) Focal Position 2

powers and the GaAs peak quickly grows to almost an order of magnitude larger than the InGaAs as power is increased from 6mW to 50mW. This can be more clearly seen in Fig 3.53c, which plots the peak heights as a function of power for both focal points

The sample without a Bragg reflector shows similar results, eliminating the Bragg reflector as a potential source of the behavior. Fig 3.54 provides plots of photoluminescence at 3 different focal positions. Once again with Fig 3.54a showing uniform intensity increase with increased power and on the other extreme Fig 3.54c showing an initially dominant InGaAs peak that is quickly overtaken by the GaAs peak. In Fig 3.54c, at peak power the emission becomes almost flat from 1.3eV to 1.45eV.

Fig 3.55 plots the peak heights of the GaAs and InGaAs peaks as a function of incident power for all three focal positions. In these cases, the area beneath the photoluminescence spectra does not remain similar, as shown in Fig 3.56. The total collected photoluminescence spectra is considerable larger for the focal position Fig

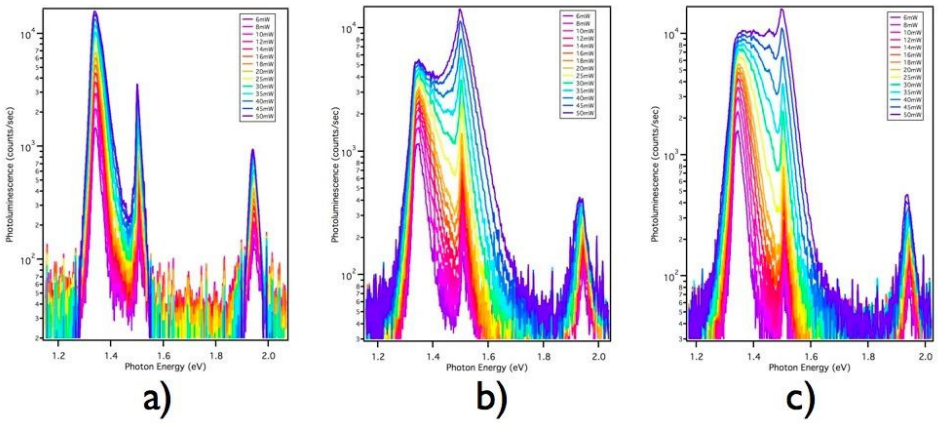

Figure 3.54: Photoluminescence response at varying temperature for substrate without a Bragg reflector at 78K with 50mW incident power at 3 different focal positions a), b) and c)

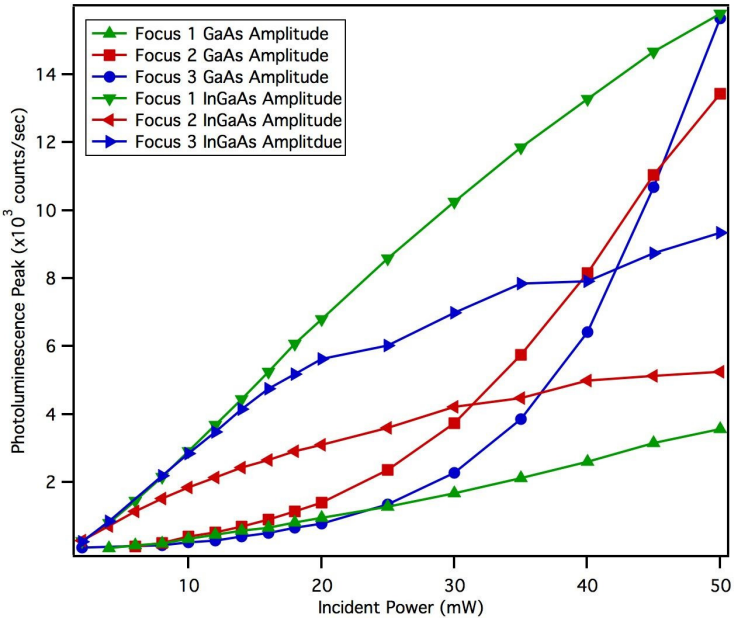

Figure 3.55: Actual Peak heights as a function of incident power for 3 separate focal positions on the wafer without a Bragg reflector at 78K and incident power of 50mW

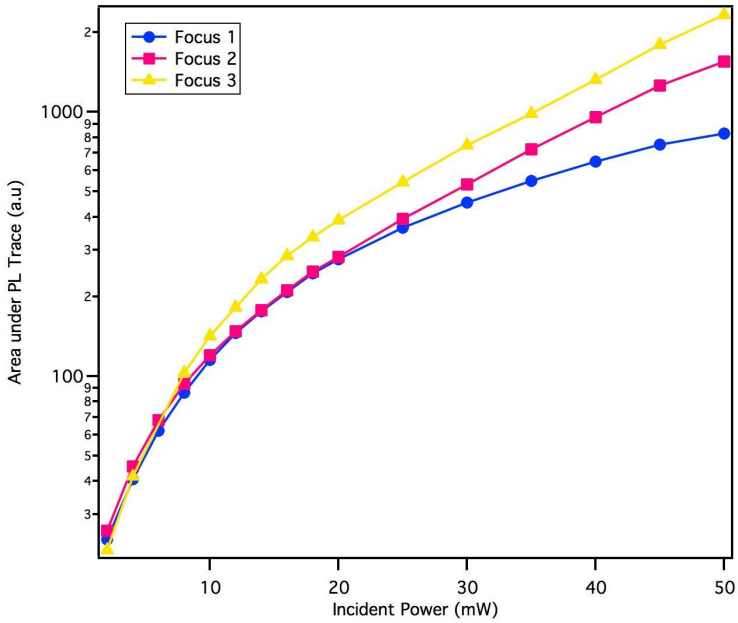

Figure 3.56: Total area beneath photoluminescence trace as a function of intensity for the 3 focal positions shown in Fig 3.54

3.54c. The 2DEHG sample has many unique properties, the most obvious being the presence of two quantum wells of opposite carriers. The quantum wells separate carriers into their respective wells and provide a high mobility channel for them to travel in. Previous research has indicated the large role that diffusion and drift away from the illumination point have on the collected signal from a wafer under photoluminescence testing. Carriers separated by the built in electric field have a path to diffuse away from the point of illumination. The limiting factor is the speed of the slowest carrier in the device. As carriers move away, if slower carriers are left behind an electric field builds up, slowing the diffusion. In the 2DEHG devices, both carriers have a high-speed channel in which to diffuse away from their generation points and experience reduced recombination due to separation.

Fig 3.57 provides a simple schematic of this process. The focus issue raises the question of whether diffusion is playing a large role in the observed photoluminescence

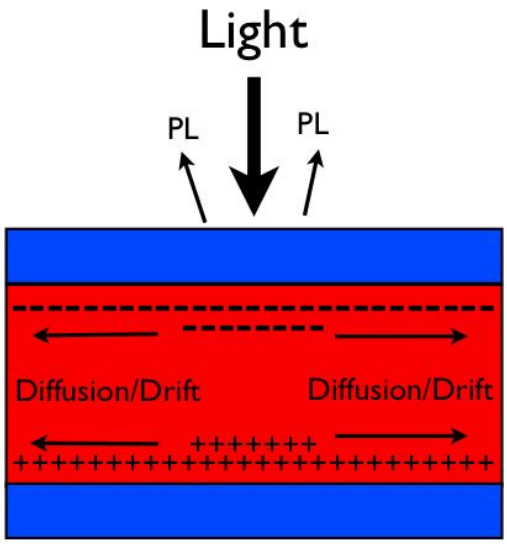

Figure 3.57: Diagram of carrier drift/diffusion away from illumination point in a 2DEHG structure

response. In order to test this possibility, a substrate was fabricated consisting of 10um x 10um mesas on the sample without a Bragg reflector. The wafers were patterned and etched several hundred nanometers to create isolated regions of 2DEHG and investigate the photoluminescence on these structures. The mesa size was chosen to ensure that at least one mesa would be entirely illuminated by the incident laser during testing. Interestingly, these mesa structures are also comparable in size to the active area of the photodetector devices which was 40um x 40um.

Diffusion is created by the build up carriers in the illuminated area, drift can be caused by the band bending created by that carrier buildup, even a small change in the internal structure can create sufficient potentials to create drift within the material. An SEM micrograph the mesa-etched wafer is shown in 3.58.

Fig 3.59 provides plots of different peak heights in the photoluminescence spectra at different focal positions on these structures. For this set of data, the GaAs peaks

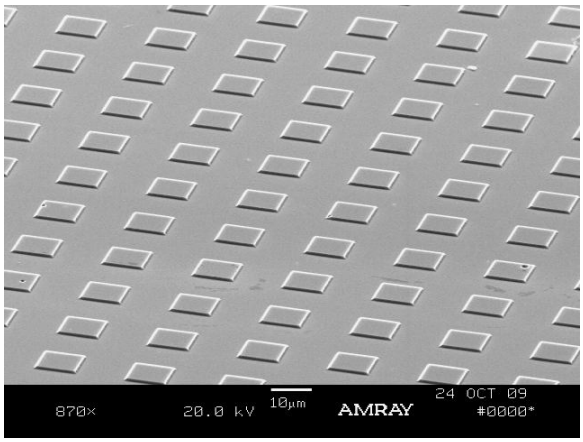

Figure 3.58: SEM Micrograph of Mesa etched wafer without Bragg reflector

were fitted to one exponential Gaussian function due to difficulties obtaining a reasonable fit at certain focal points. This combined fit provides important information on the photoluminescence results.

Using the spectrometer we are able to collect a set of photoluminescence spectra as the focal point is changed. The precision of the focal steps is low but we can take roughly equal steps through the focus and collect spectra at each point. In Fig 3.59b, the mesa-etched structure shows results indicative of a change in the incident power, a fairly uniform increase in peak height as the focal position changes. The GaAs substrate does not appear to provide an appreciable signal, making analysis simpler. In Fig 3.59b however, there is a very different behavior. As the focal point changes, each peak reaches a corresponding maximum signal intensity. The positions at which this happens however are different for each peak. The InGaAs peaks reach a maximum near focal position 15, P1 has a broad maximum spreading from 17 to 30. The GaAs peak hits a maximum near 30 and appears to saturate for the following focal position steps. The InGaAs peak then begin to decrease once the maximum is reached, while the GaAs peak increases, indicating this result is not due to saturation. These results

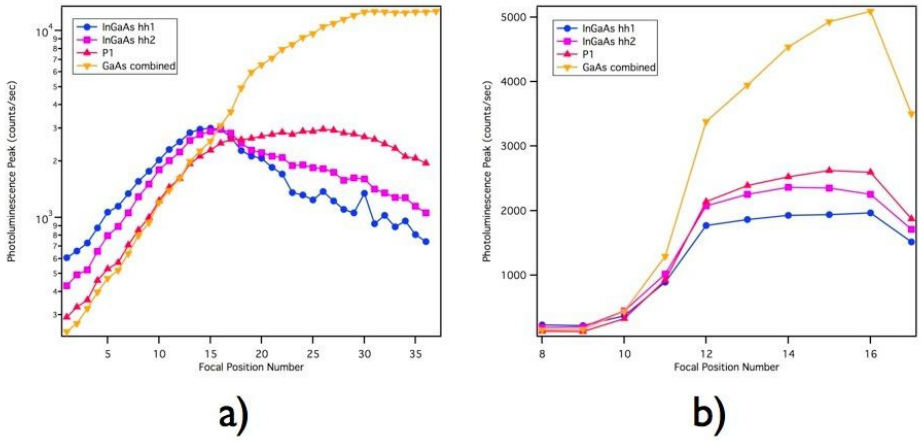

Figure 3.59: Peak heights for bulk wafer (pink) and mesa etched substrate (blue) as a function of focal position b)Peak energies in the bulk wafer (blue) and mesa etched wafer (pink) as a function of focal position

are not seen in 2DEG or 2DHG wafers, both of which were also tested. There are several possible mechanisms that may produce this behavior. The beam may be altering the internal band structure and rearranging the distribution of carriers in the material. This effect should be intensity dependent however and the observed results do not correlate well with photoluminescence taken as a function of power. Another possibility is diffusion occurring within the structure. With a wide beam, carriers are generated across a large area creating limited band bending and limited charge buildup. As the beam narrows, if a similar number of charges are generated, the generated carriers are in a more concentrated area increasing potential band bending and charge concentrations within the well. The narrow beam encourages electron-hole pairs to diffuse/drift away from the illumination point, thereby depleting the carriers recombining in the wells. At issue is why it appears the InGaAs wells are affected more than the GaAs well, though where the GaAs peak originates from is difficult to ascertain.

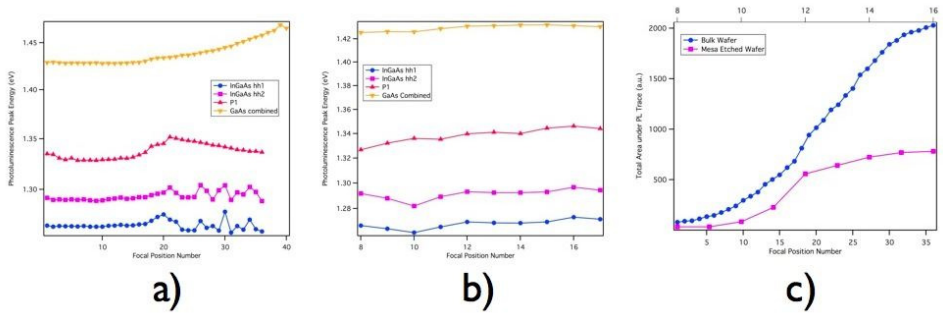

Figure 3.60: a) Peak energies as a function of focal position for the bulk wafer b) Peak energies as a function of focal point for the Mesa etched structure c) Total area beneath the photoluminescence trace as a function of focal point for both samples

Fig 3.60 a and b show the peak energies as a function of focal position. The mesa-etched structure (**??**b) shows little change across the full focus. The bulk sample however shows the peak energy of both P1 and GaAs shifting with focal position, corresponding to the regions of their peak amplitudes. As stated earlier, for these fits all GaAs related peaks were fitted to on exponential Gaussian function. The peak shift can then be seen as an indication of redistribution of energies amoung the GaAs related peaks. 3.60c shows the areas beneath the photoluminescence traces as a function of focal position. It is important to mention that the focusing effect was observed at all incident wavelengths. Though not mentioned previously, focusing also played a major role in the high speed photoresponse measurements. In the measurements the incident laser is focused by a lens a few centimeters above the sample. Prior to any photoluminescence measurements, it was observed that the time response was strongly effected by the laser focus. At the time of measurement the issue was not explored and focus was maximized for the fastest response. Incidentally, this position was noticeably different from the smallest beam size position. There are issues related to contacts that may be the cause of the focus issue seen in the

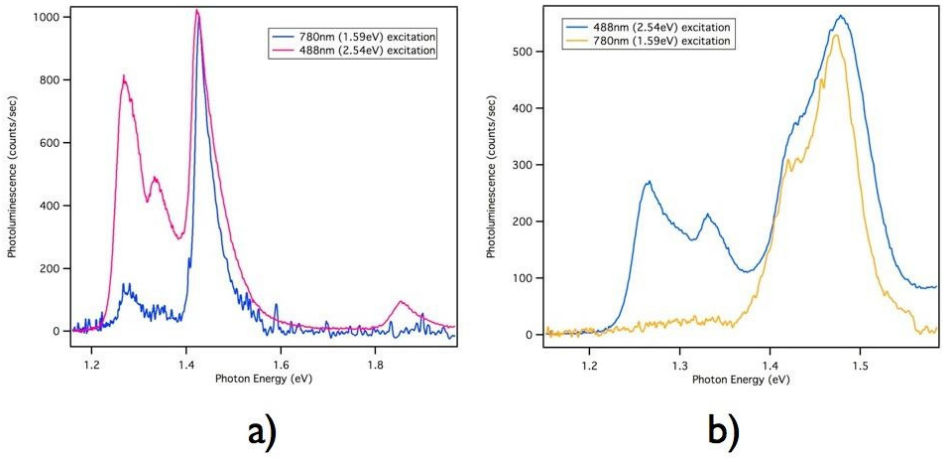

Figure 3.61: Photoluminescence spectrum at 488nm and 780nm for the a) Bragg substrate b)substrate without a Bragg reflector

high speed measurements. However, the results seen in the photoluminescence traces indicate that further exploration is needed to understand the observed effect and possibly utilize the behavior for device functionality.

3.10.9 Effects of Incident Wavelength

Thus far, only traces collected with 488nm incident wavelength have been discussed. The reason for this is two-fold. Initially, 488nm was the only available source for the measurements. Second, the 488nm wavelength is absorbed by AlGaAs providing more electron-hole pairs within the structure. Assuming that the internal fields redistribute the carriers to the wells and other points of higher carrier concentration, using this wavelength can greatly enhance the observed photoluminescence spectra by showing more peaks and therefore more transition energies.

For comparison the wafers were also investigated using longer wavelengths. Fig 3.61 shows a plot of photoluminescence taken using 488nm illumination and 780nm illumination at similar powers. A distinct difference is seen in the traces providing

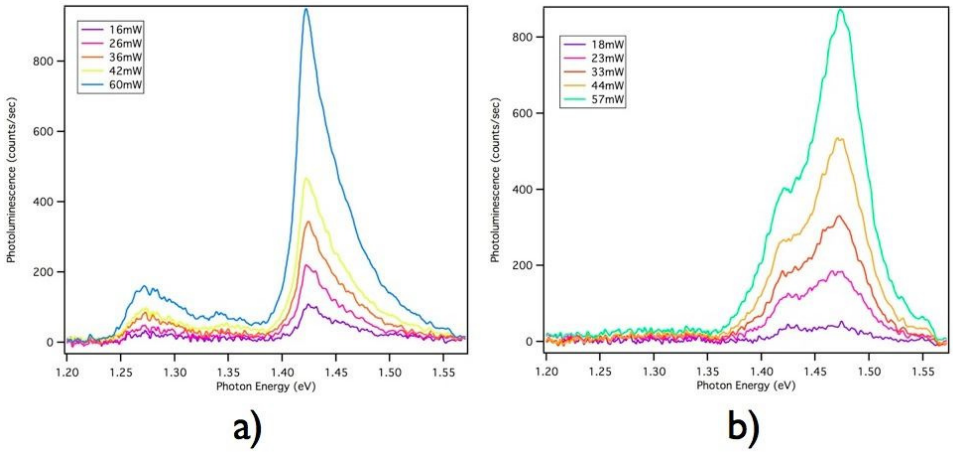

Figure 3.62: Photoluminescence response at varying incident powers for a)Wafer without a Bragg reflector b)Wafer with a Bragg reflector

some important information regarding the structures. The photoluminescence signal from the InGaAs region is almost entirely absent from the spectra from the Bragg wafer and strongly attenuated in the sample without a Bragg reflector. P1 is also absent in the Bragg and attenuated in the non-Bragg, providing more evidence that the P1 peak is tied to the InGaAs region.

Fig 3.62 shows the photoluminescence from both wafers at 780nm at different incident powers. Here again we see a complete absence of the InGaAs peak in the Bragg sample and a strong attenuated peak from the InGaAs and P1 in the non-Bragg sample. The results suggest that electrons needed for recombination in the InGaAs are supplied by the Lower Barrier and Bragg Reflector. A small amount of electrons may leak over the barrier, creating the small peaks seen in the sample without a Bragg reflector. These are completely blocked however in the sample with a Bragg, resulting in no InGaAs signal.

As seen in Fig 3.63a, the P1 peak is also seen in the photocurrent wavelength response. A comparison photoluminescence trace is shown in Fig 3.63b, both measure-

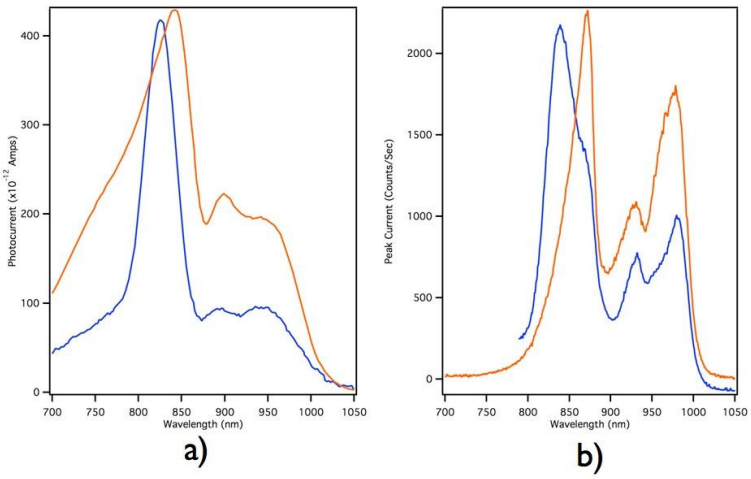

Figure 3.63: a) Photocurrent as a function of wavelength for the Bragg (blue) and No Bragg wafer(orange) b) photoluminescence response for the Bragg(blue) and No Bragg(orange) wafers at 50mW

ments provide a similar set of resulting peaks. The strong absorption may indicated that this peak is not a phonon-assisted one, as suggested earlier. All this factors, combined with the temperature independence make the origins of P1 (And P2 and the AlGaAs high energy shoulder) difficult to determine with confidence without additional measurements.

3.11 Future work

3.11.1 Device Design

The 2DEHG wafers have proven to be much more complex and rich in behaviors than initially expected. In order to understand more of the behaviors and possible uses for such a material platform, more complicated devices would enable more direct characterization of particular behaviors. In order to better understand the effects of the dual well structure, individual contacts to each well would allow more direct interrogation of their interactions. A device as simple as placing a Schottky contact

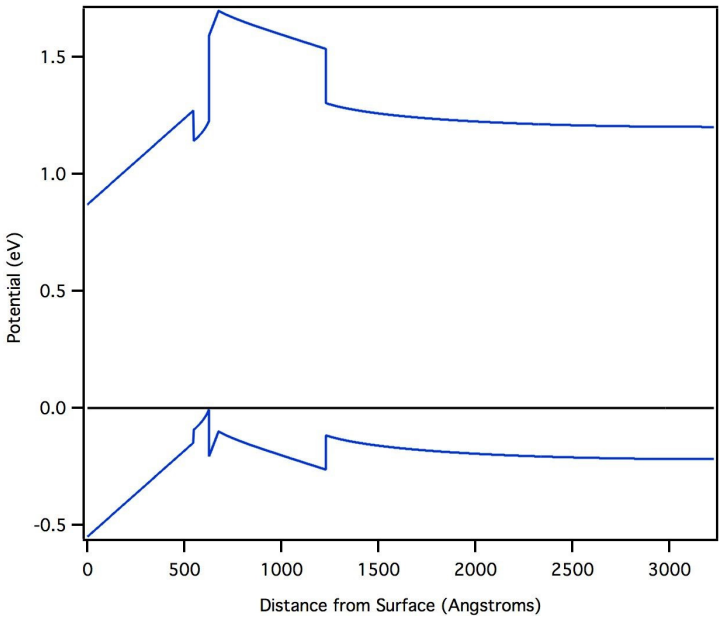

Figure 3.64: Simulated Band diagram for Schottky contact on the GaAs region of the 2DEHG, with the Upper Barrier and a portion of the GaAs layer etched away

onto the GaAs absorption layer, after etching though the AlGaAs upper barrier and Si delta doping region would allow a Schottky contact directly on the hole well structure. Fig 3.64 shows the band diagram from a resulting structure. It is a preliminary simulation that does not account for the lateral effects of the neighboring unetched substrate but allows a strong assumption that contact can be made directly to the hole well while maintaining it as a populated quantum well. It is important to note however that the lower band gap of both the GaAs and the lower Schottky barrier for holes would greatly increase the dark current of such a device.

3.11.2 Characterization

Using modified contacts to the substrate would allow several issues to be investigated. The asymmetry created would allow for easier extraction of the carriers participating in the photocurrent and the capacitance measurements. Under low bias

conditions, it would also be possible to separately extract electrons and holes from the structure during optical interrogation, in fact additionally adding a contact to the underlying substrate may illuminate the origin of several of the unidentified photoluminescence peaks by allowing extraction of generated electron-hole pairs in each region of the device. Finally, an asymmetric design offers the possibility to greatly enhancing the high-speed response of the device by collecting generated holes directly from the hole well instead of through the top contact.

4. GaAs-Based Nanowire Devices

4.1 GaAs Nanowires

Nanowires offer a platform for both studying the basic physics that govern the behavior of semiconducting structures, as well as the potential to build highly specialized electronic devices that react strongly to applied stimuli. By introducing finite dimensions within the structures that are commensurate with a length scale below which quantum effects begin to manifest themselves, nanowires can harness a previously inaccessible set of behaviors for device performance. Nano-structured materials in general allow for the design and fabrication of devices that can improve upon the performance of equivalent planar and bulk devices and occasionally introduce entirely new functionalities not possible at the bulk semiconductor level. Silicon and germanium nanowires have been well studied [90; 91], and an array of other nanowire types including indium-arsenide, gallium nitride, zinc-oxide and even conducting polymers [92; 93; 94; 95; 96; 97; 98; 99; 100]. GaAs, despite popularity in bulk devices, has received considerably less attention in the nanowire field, with respect to the characterization of the electronic properties and design of devices. This has been a factor of the difficulty of fabrication of contacts and the strong surface effects in GaAs and GaAs-based materials.

4.1.1 Growth and Optical Characterization

GaAs nanowires can be grown using several different methods including: molecular beam epitaxy, metal-orgainic chemical vapor deposition, metal-organic vapour phase epitaxy and chemical vapor deposition [101; 102; 103; 104]. The wires are typically grown on a GaAs or sapphire substrate using a gold catalyst for growth. These

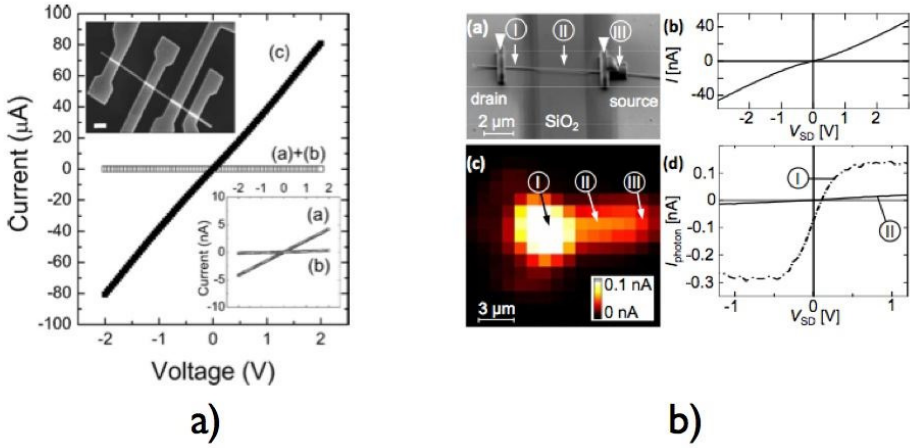

Figure 4.1: a) P-type doping results on single GaAs Nanowires [Reprinted with permission from [105]. Copyright 2008, American Institute of Physics] b)Optical response of single GaAs Nanowires [Reprinted with permission from [109]. Copyright 2008, American Institute of Physics]

structures have been interrogated extensively using optical techniques with many groups demonstrating growth of thin and defect free wires [105; 106; 107; 108; 109; 101; 102; 103; 104]. Several research groups have published work on the characterization and fabrication of doped GaAs nanowire devices. Fig 4.1a shows published work demonstrating p-type doping of GaAs wires using ion implantation and annealing [105]. The wires demonstrated high conductance values, comparable to bulk GaAs. The undoped wires, shown in the inset, demonstrated very small currents, 2nA at 2V bias for as-grown and 100pA at 2V after annealing, even for 150nm diameter wires. Another group demonstrated optical absorption in a GaAs nanowire MSM device, shown in 3.1b. The wire was p-type doped during growth. The device was fabricated using dielectrophoresis and focused ion beam deposition. The measurements indicated a strong photoresponse when the wire was illuminated near the contact. The use of focused ion beam deposition on the wire has been shown afterwards to greatly affect the wires behavior, making it even more p-type across the wire, even when the beam

is not incident on the wire [110].

A few other papers have also been published on GaAs nanowire devices, including the creation of a MESFET device [108] and other optical detectors [111]. Several groups have also fabricated top-down wires by etching bulk substrates in narrow channels [112]. Ideally in bulk devices, detectors are usually made with a region that is undoped, or unintentionally doped. Doping increases the carriers present in the material before any stimulation has been applied, decreasing the possible percentage change of conductivity. The signal is typically measured as a change in current under an applied voltage with incident light or other stimulation.

A high performance detector device should incorporate a undoped or low doping absorption area, to minimize noise and dark current. To date, no intrinsic GaAs nanowire devices with a thin diameter (¡ 50nm) have been reported. The reason for this is the difficulty in fabricating an ohmic contact to such a structure and controlling the surface states. Here we will present the results of designing and implementing ohmic contacts to intrinsic (or unintentionally doped) GaAs nanowires. Several different contact recipes were tested and the results presented. These recipes are then compared and the photoresponse measured. In some cases the devices were also gated to extract effective mobilities.

4.2 Growth and Characterization

The wires for this work were grown on GaAs substrates using gold nanoparticles and metal-organic vapour phase epitaxy at 400C. The ratio of column III (gallium and aluminum) to column V (arsenic) precursor gases during growth appeared to influence the level of unintentional dopants present in the wire. Full details of the growth of wires can be found in [113]. The wires were 2.3-5.4um long and had diameters of 70-80nm with very little tapering. Fig 4.2 contains 3 separate images for the as-grown

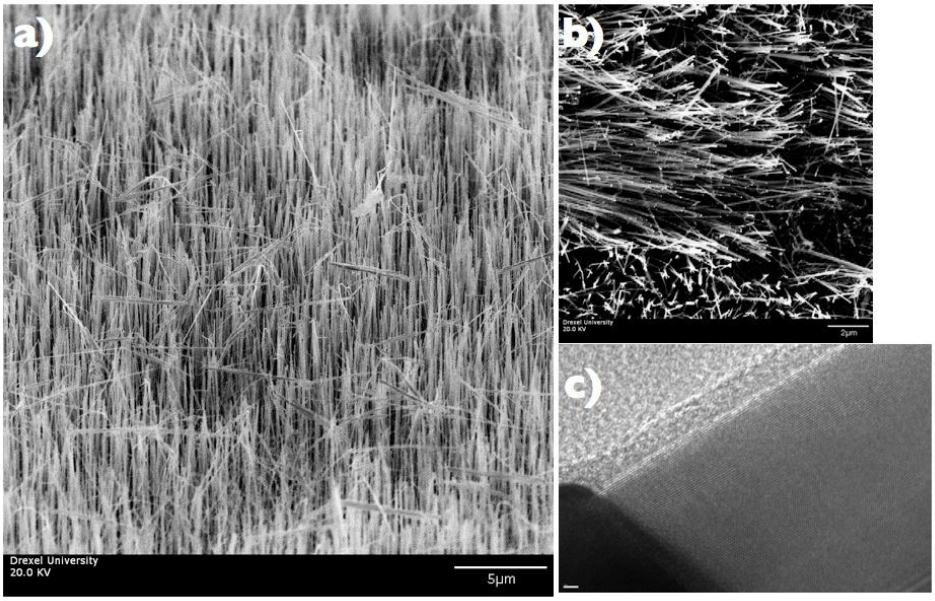

Figure 4.2: a) Scanning electron microscope secondary electron image of as-grown wires b)Back-scattered image of the as-grown wires c)Transmission electron microscope image of the interface between the gold catalyst and nanowire

wires. Fig 4.2a is an secondary electron image showing a large area of the as-grown chip, b) is a backscattered images revealing the gold catalysts (white dots) remaining at the end of the wires. Fig 4.2c is a transmission electron microscope(TEM) image revealing the interface with the catalyst, of interest is the thick oxide shell present on the wire.

4.3 Device Fabrication

Nanowires were sonicated off of the as-grown substrate and suspended in isopropyl alcohol. The sonication times varied from 1 second up to 15 seconds depending on the density of the growth chip. From this suspension, the nanowires were dispersed onto silicon dioxide/silicon substrates pre-patterned with alignment marks and bond pads. The silicon dioxide was thermally grown and 200nm thick, the underlying sil-

icon was degenerately doped p-type to be highly conductive. The isopropyl alcohol solvent is evaporated off, leaving a dispersion of nanowires covering the substrate. Fig 4.3 shows an scanning electron microscope image of wires dispersed and lying on the substrate in an alignment mark box. Using an scanning electron microscope, the wires are then located and imaged in relation to the alignment marks. Using these images, patterns for electrodes are then generated. The sample is coated in a tri-layer poly(methyl methacrylate) (PMMA) resist structure, each layer consisting of a different molecular weight solution (950K/100K/950K) for patterning. The tri-layer PMMA is used to create sharp sidewalls on the deposited metal electrodes by utilizing the different development rates of different molecular weight mixtures. The center layer, 100K PMMA, develops at a higher rate, leaving a notch in the resist sidewall after development and preventing the deposition of a continuous metal layer on the resist sidewall. After coating and a 30 minute bake out at 170°C, the samples are then electron beam patterned using the Nano Pattern Generation System (NPGS). NPGS automates the process of aligned patterning of the samples by allowing the user to open up and image small windows on the alignment marks and registering the patterns to the imaged marks. With this system we are able to achieve an alignment accuracy near 100nm. The samples are patterned, typically at a beam current of 50pA and dosage of $250\mu C/cm^2$. The patterns are then developed in an Methyl isobutyl ketone:isopropyl alcohol mixture (1:3) for 70 seconds, rinsed in isopropyl alcohol for 20 seconds, blown dry with nitrogen gas and finally de-scummed in oxygen plasma for 5 seconds to remove any residual resist. Just prior to placing the samples in the evaporator, the native oxide is removed in an hydrocholoric acid:deionized water solution (1:1). Metal deposition is done in an electron beam evaporator at a pressure of $5*10^{-6}$ Torr ($6 * 10^{-4}$ Pa)or below. Each metal is deposited sequentially without breaking vacuum in the chamber. Deposition rates are typically in the 0.5 to 1nm/sec range

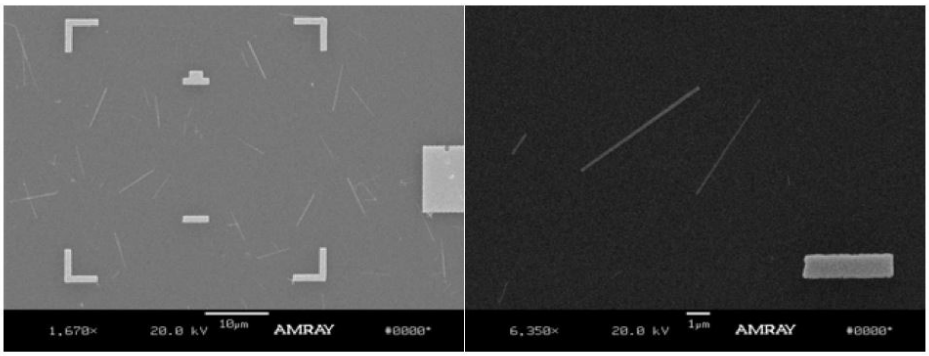

Figure 4.3: Scanning electron microscope image of wires dispersed on alignment marks for contacting

depending on the material, as measured with a quartz crystal balance. After deposition the substrates are placed in acetone for lift-off removal of the unwanted metal and resist and finally cleaned in oxygen plasma for 30 sec to remove all residual resist and organics. The samples are placed in the Lakeshore Cryogenics Probe Station, as described in Chapter 2. The fabrication had two goals in creating contacts to the nanowires: ohmic contacts and stable Schottky contacts. Ohmic contacts were used to investigate the conductivity of the wires and other intrinsic properties. Schottky contacts were intended to replicate the Schottky metal-semiconductor-metal photodetectors discussed in the previous chapter. Schottky contacts would be expected to provide a very low dark current on these materials and provide a strong light response as seen in bulk devices of similar structure It was proposed by the growers of GaAs nanowires that they may be lightly p-type due to unintentional carbon doping during growth. This carbon doping originates from the precursor gases used and is typically in the $10^{14}$to$10^{15}/\mathrm{cm}^3$ range for bulk growth of GaAs. This low carrier concentration presents an obstacle to contacting these wires, as ohmic contact to undoped GaAs is

difficult and not frequently reported in the literature. In typical devices, ohmic contacts are made using intentionally doped materials, this doping lowers barriers seen at the contact and aids in creating a ohmic contact. In standard ohmic contacts to GaAs, a metal layer is deposited that includes a dopant material, such as Ge. After deposition the device is annealed, usually between 350-500C. The annealing causes a reaction at the interface that can allow the dopant atom to diffuse into the material, creating a highly doped layer near the contact. This formation is assisted when the underlying material is already highly doped. Different dopant materials are used for different contact types, germanium for instance is an n-type dopant and zinc can be used as a p-type dopant. The issue of ohmic contacts to GaAs continues to receive considerable attention from research groups, as it is a difficult and highly variable process. The mechanisms governing the formation of these ohmic contacts is also not completely understood and continues to be an ongoing research. Published work tends to report on recipe results as opposed to an in-depth exploration of the physics behind the contact formation.

For conventional GaAs devices the industry standard for ohmic contact to GaAs is nickel/germanium/gold based contacts, with the sequence of materials starting with nickel making contact with the GaAs material first, though ratios of the materials appear to be of greater importance than deposition sequence [114]. In the formation of this ohmic contact the sample is annealed and the germanium spikes into the substrate at different points creating a strong ohmic connection to the underlying material. This recipe has produced the best and most reliable results for GaAs devices for the past few decades. The formation mechanism for ohmic contacts when applied to nanowires is very problematic in nanowire systems. In bulk devices the ohmic contact is actually an inhomogeneous mix of ohmic points and non-ohmic areas. The resulting ohmic contact is an average of all the points on the electrode and

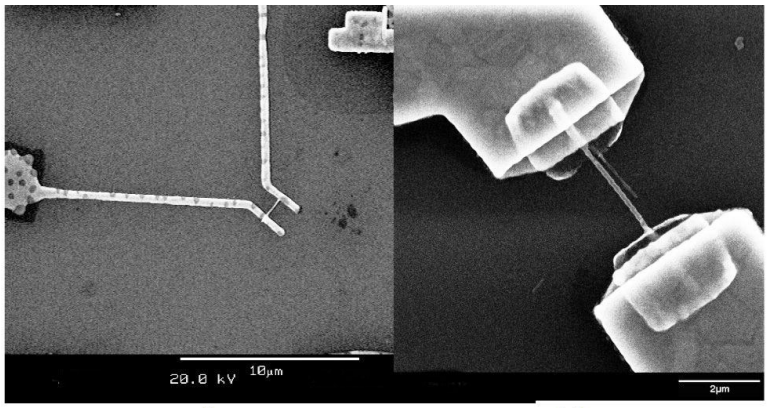

Figure 4.4: Scanning electron microscope image of nanowires contacted with a)nickel/germanium/gold b)palladium/zinc/palladium/titanium/gold. The nickel/germanium/gold contacts contain spots where the complexes needed for ohmic contact formation have formed, while the palladium/zinc/palladium/titanium/gold contacts become grainy, with a more uniform formation of palladium complexes within the annealed leads

is dominated by the small area that is actually making good contact. For nanowires, the small contact area and the size of the germanium spikes formed largely prevent ohmic points from being formed on the nanowire itself. In order for the contact to work a spiking region must form on either end of the wire, which has a very a low probability of occuring. Fig 4.4a shows a nanowire with these nickel/germanium/gold contacts after annealing. The small darker spots on the leads are the spike points where the nickel/germanium/gold has formed the complexes necessary for formation of an ohmic area. (Note that these leads are on silicon dioxide and no spiking occurs but the spots represent where the contact materials have combined in such a way that would form spikes on materials where the germanium was able to diffuse into the substrate). Of interest is the small percentage of area covered by these regions, limiting the probability of formation on either end of the nanowire. An alternative to the nickel/germinium/gold contact recipe is using palladium-based contacts

[115; 116; 117; 118; 119; 120; 121; 122; 123; 124; 125; 126]. The formation mechanism in palladium based contacts to GaAs is very different than for nickel/germanium/gold contact formation. The palladium reacts with the GaAs surface forming a Pd_xGaAs compound at low temperature. These compounds are not stable at higher temperatures and above 400C the Pd_xGaAs compound is consumed by the reaction between palladium and the included dopant material. The process removes the palladium, leaving the GaAs it reacted with originally. Once the palladium is fully consumed, the remaining dopant can regrow at the surface or diffuse into the defects created by the Pd_xGaAs formation or both. The presence of hydrogen can assist in the removal of oxygen on the surface by also reacting with the palladium. Depending on the dopant material used, palladium can either facilitate shallow diffusion into the underlying material by initiating defects in the crystal or it can facilitate regrowth of that material on the surface. In every case, the ohmic reaction and formation of the necessary complexes takes place more uniformly across the contact regions. Fig **??**b shows a nanowire contacted using palladium/zinc. The grain size of the post-anneal contact is visible but no segregation is seen of the compounds formed, as was the case for nickel/germanium/gold.

Fig 4.5 shows an transmission electron microscope image of a palladium/germanium contact on GaAs. In this case, the palladium and germanium mix creating a palladium-germanium compound. Once the palladium is exhausted, the remaining germanium regrows epitaxially on the surface of the GaAs, creating a small bandgap capping layer [116]. This new regrown layer present a significantly smaller barrier for carriers to overcome. Some of the germanium will also diffuse into the GaAs to create an additional shallow dopants. In the nickel/germanium/gold system the ohmic contacts were exclusively n-type, the palladium/germanium system can create a contact that has a lower barrier for both carriers if a significant amount of germanium does

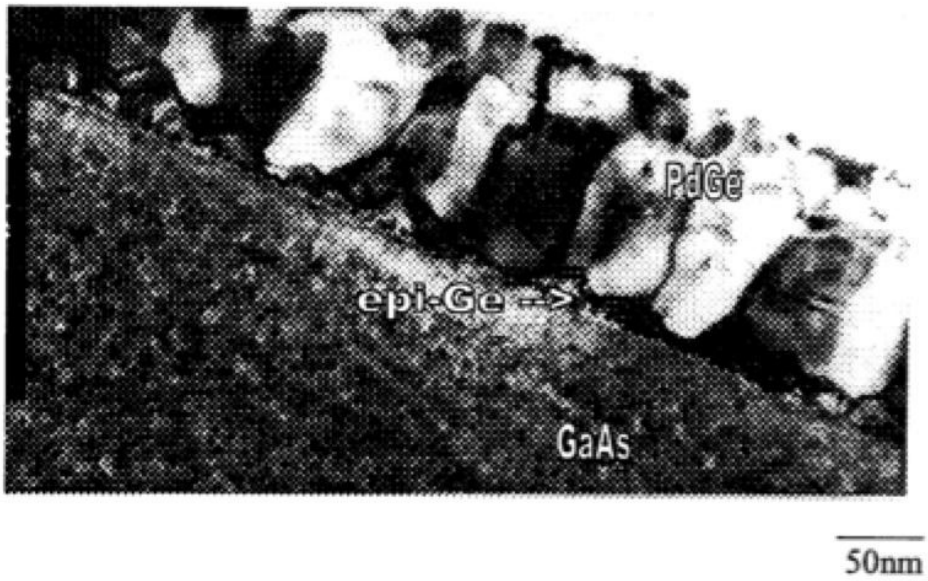

Figure 4.5: Transmission electron microscope image of regrown germanium at palladium/germanium-GaAs interface [116]

not diffuse into the underlying area. The germanium regrowth reduces the barrier to both electrons and holes, allowing electrons and holes to move through the contact with less energy. Fig 4.6 shows an scanning electron microscope image of completed devices.

Three separate recipes were used, two ohmic and one Schottky. The ohmic dopants were chosen as zinc for p-type and germanium for n-type. For the schottky devices a combination of palladium/titanium were used. It is expected that the palladium will improve the interface by removing the native oxide and the titanium provides a strong and stable Schottky contact to GaAs.

The wires are expected to be lightly p-type due to unintentional doping during growth, it is expected that palladium/zinc contacts should make the best contacts to the wires. The devices were fabricated as described earlier with a metal contact layer of palladium/zinc/palladium/titanium/gold. The initial palladium layer thickness

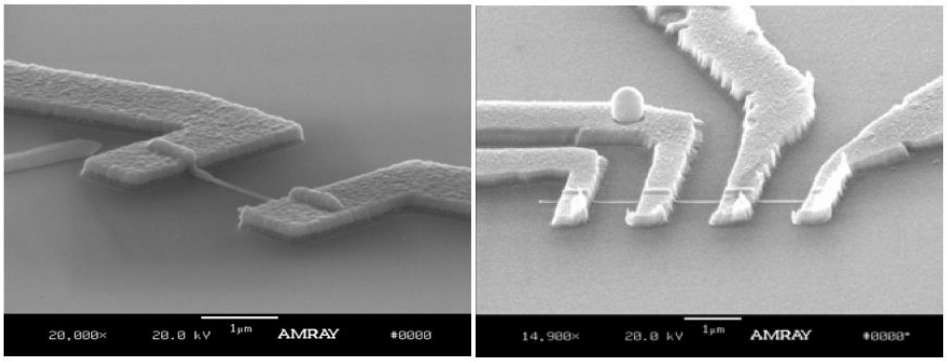

Figure 4.6: Scanning electron microscope image of GaAs nanowires contacted with palladium/zinc based contacts. The darker layer visible beneath the brighter upper gold layer is the palladium/zinc material

was varied, while the zinc layer and second palladium layer were 20nm thick each. The titanium layer, 10nm thick, serves to isolate the top gold layer from the underlying palladium/zinc and prevent intermixing. At high temperatures gold can also form a complex with GaAs that can change the resulting contact behavior. The final gold cap was typically 150nm to ensure that that no breaks or discontinuities occur between the contact on the wire and the surrounding metal electrode.

4.4 Electrical Characterization

Fig 4.7 shows the results from wires with a 10nm thick palladium initial layer. The devices were rapid thermal annealed in forming gas, hydrogen:nitrogen (5:95), for thirty seconds at 400°C. The samples were allowed to cool and then placed in the probe station. Eight wires devices were fabricated on the chip, seven of which were functional. The devices were measured in at a vacuum level of 10^{-6} Torr ($1.3 * 10^{-4}$ Pa) and 300K. The resulting IV traces are primarily linear, with a slightly increasing slope as voltage is increased. The observed conductance values vary almost two orders

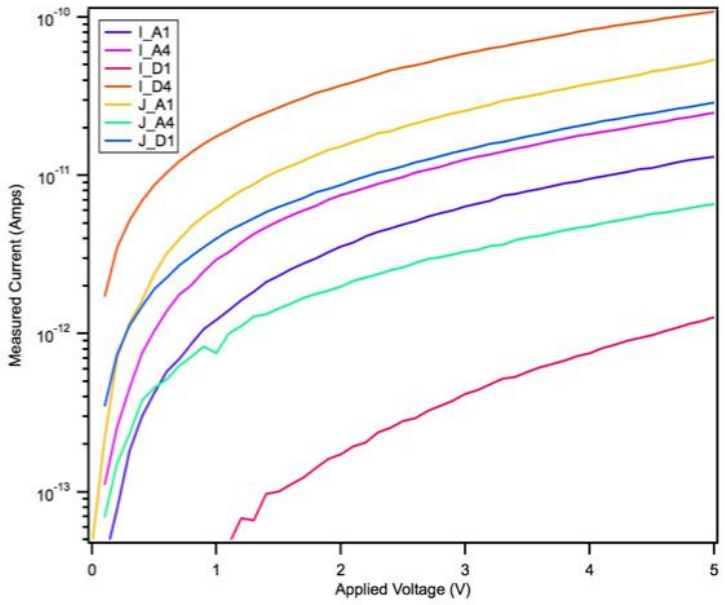

Figure 4.7: IV traces from GaAs nanowire contacted with palladium/zinc/palladium/titanium/gold contacts

of magnitude for wires fabricated on the same chip.

4.4.1 Figures of Merit

In order to extract more quantitative information from the current-voltage traces, a system of extraction for figures of merit was developed, the basics of which are shown in Fig 4.8. The slope between the bias of two and three volts was used to calculate conductivity and resistance values using a best fit line, the x-intercept was used as a measure of linearity of the traces, with a larger value of the x-intercept indicating a trace with increasing slope, while a negative value indicates a trace with decreasing slope. Conductivity was calculated treating the wire as a simple resistor. This system allows the evaluation to account for nanowire length and diameter. The peak current is defined as the current at three volts bias. All measurements reported

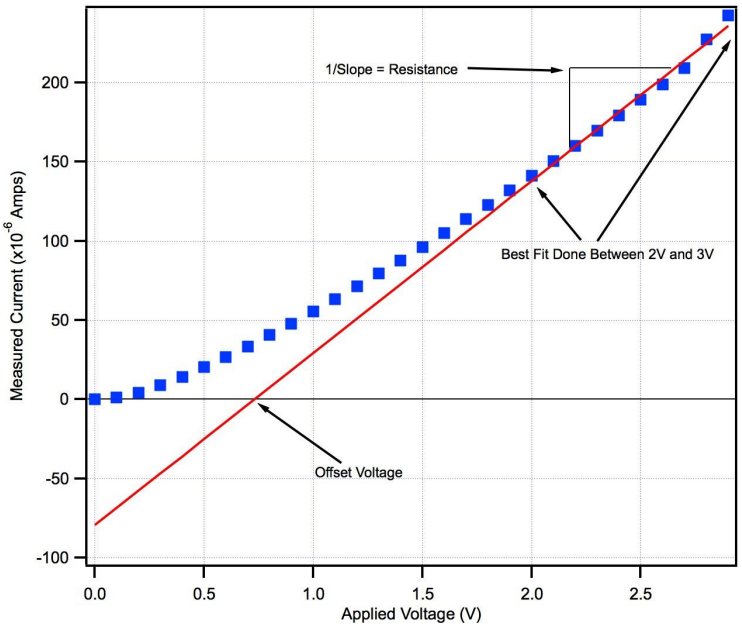

Figure 4.8: Diagram of the origins of figures of merit. Resistance is the inverse slope between 2 and 3V bias, offset is the x-intercept of the best fit line in this region

are two terminal measurements. Four-terminal measurements have limited meaning and usefulness at the nano-scale. The reason for this is outside the scope of the work but more information can be found in [37]. The contact resistances are also neglected due to the very large overall resistance. The reported figures of merit should not be taken as true values of resistance but as a means to quantitatively compare the results from different devices.

4.4.2 Recipe Comparison

Initially three separate contact recipes were attempted on the GaAs nanowires, an additional recipe that combined the first two was then added. All the recipes were annealed in a rapid thermal annealler in forming gas, hydrogen:nitrogen (5:95). Recipes using palladium/zinc, palladium/germanium, palladium/zinc/germanium and palladium/titanium were all fabricated and tested. For these palladium/zinc devices,

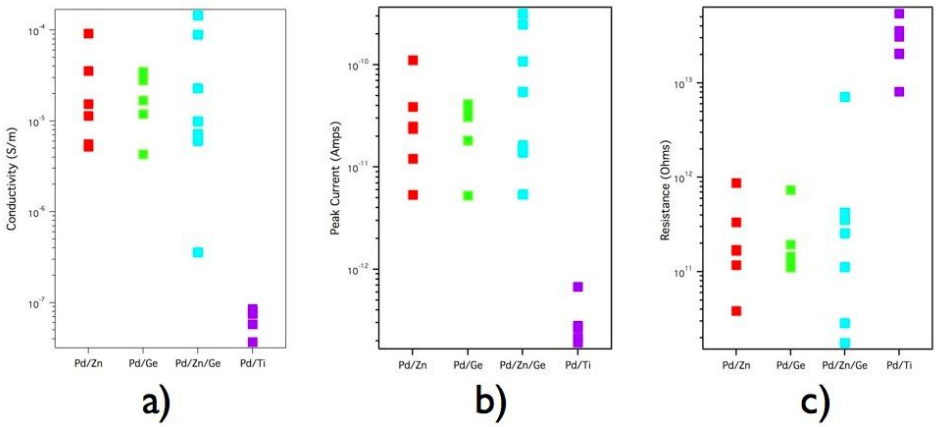

Figure 4.9: Calulated Parameters for different recipes a) Resistance b)Peak Current c)Conductance

an initial layer of 3nm of palladium was used, the anneal was done for 20 sec at 400C. For the palladium/germanium contacts the contact recipe was, starting from nanowire surface: 10nm palladium/40nm germanium/10nm palladium/10nm of titanium/150nm gold. The titanium and gold serve the same function as with the palladium contacts. These devices were also annealed for 20 sec at 400C. For the palladium/zinc/germanium contacts the recipe was 10nm palladium/10nm zinc/20nm palladium/115nm germanium/45nm titanium/100nm gold. Devices in this set were annealed at 400 and 425C for 30 sec with no noticeable difference attributable to anneal temperature. The final set was palladium/titanium with 10nm palladium/40nm titanium/40nm palladium/10nm titanium/150nm gold. These devices were annealed at 425C for 60 seconds. Fig 4.9 shows the resulting figures of merit extracted for each wire in each contact recipe. The palladium/titanium recipe showed the smallest currents, hundreds of femtoamps, and highest resistances, tens of gigaohms. The palladium/germanium contacts were the most consistent and provided the highest yield of functional devices. The palladium/zinc/germanium contacted devices showed the

best and worst results in terms of conductivity and resistance for the ohmic contacts. The palladium/zinc/germanium contacts attempt to make use of the benefits of both the zinc doping created in the palladium/zinc contacts as well as the germanium regrowth layer to lower the initial barrier seen by carriers. Interestingly, all three types of ohmic contacts provided strong but inconsistent results, with an order of magnitude difference in calculated conductivity after the diameter and length of each nanowire device had been accounted for. Ohmic contacts to undoped GaAs wires has not been reported in the literature to date.

To investigate further the initial palladium layer in the zinc based contacts was varied in thickness to attempt to optimize the contact recipe. Annealing temperature experiments were also conducted, with all results conclusively indicating the best annealing temperature to be near 400C for all ohmic recipes studied.

Additionally, samples annealed at 300C demonstrated ohmic response with smaller overall currents. A comparison of conductance before and after the 300C annealing revealed no significant change in current magnitude but the process created traces with significantly less hysteresis and noise. This same results was observed on contacted bulk GaAs as well. Annealing longer than four minutes at 300C resulted in a drop in conductance in both the nanowires and bulk devices as well.

4.4.3 Palladium Thickness Optimization

Published research on palladium based contacts has shown a strong dependence of the contact resistance on the thickness off the underlying palladium layer. This layer must be thick enough to react with the underlying GaAs and native oxide but thin enough to allow the dopant material to move though to the surface. Fig 4.10 shows a comparison of the calculated resistance, conductance and peak current values for four different palladium thicknesses. Again the results show some indication that

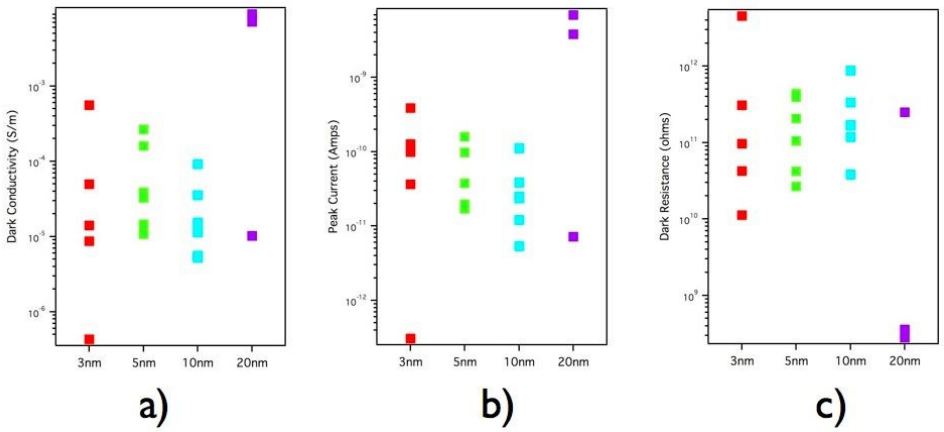

Figure 4.10: Extracted parameters for palladium/zinc devices with varying palladium thickness a)Conductivity b)Peak Current c) Resistance

the thicker palladium layers provide better contacts but the results continued to be fairly inconsistent with an order of magnitude difference in conductivity for a wire contacted in the same process run.

Several samples were annealed in stages in order to extract the best annealing time for the devices. Fig 4.11 shows the results from two wire sets contacted with the zinc recipe and an initial layer of 5nm of palladium. It appears that the contacts remain fairly stable with annealing longer than 20 secs, with 30 seconds yielding the most consistent results.

4.5 Light Response

GaAs is a popular material for optical detectors due to its band gap just below the optical range (room temperature band gap of 1.42eV) and its high electron mobility. GaAs photodetectors offer the possibility of high speed, high resolution imaging arrays. Several research groups have demonstrated the viability of nanowire based detectors, including GaAs nanowire optical detectors [127; 99]. These devices offer

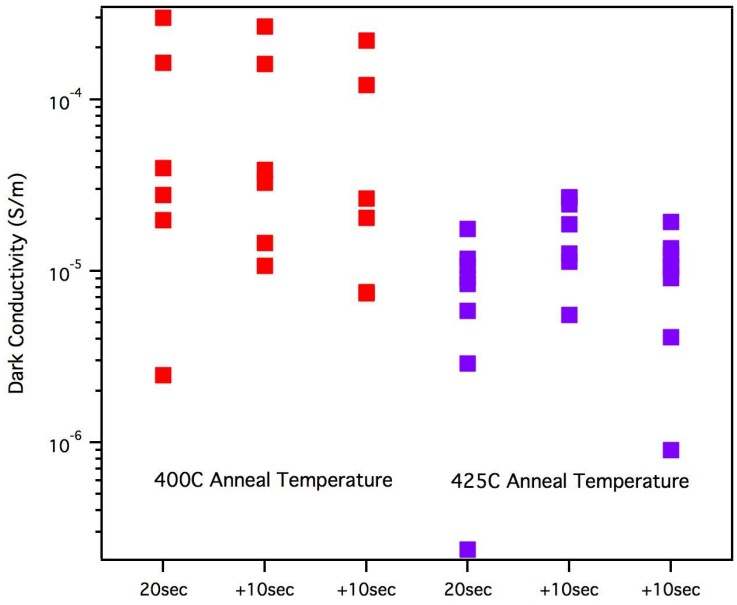

Figure 4.11: Conductivity of devices at different annealing stages for palladium/zinc contacted wires, palladium thickness is 5nm

several interesting applications such as on-chip optical interconnects. The ability to fabricate devices on a low leakage insulator also offers the possibility to remove many of the negative effects created by substrates in planar devices.

Following contact characterization, we then investigated the optical response of these wires. The source used was a broad spectrum lamp operating at 150W and diffused. Again the measurements were done under a vacuum level of 10^{-6} Torr ($1.3 * 10^{-4}$ Pa) and at 300K.

Fig 4.12 shows the comparison of the four recipes under light and in dark. The plots provide the ratios of the light current-voltage parameters to the dark current-voltage parameters. We see that where palladium/titanium had the lowest conductance in dark, it has the highest responsivity under light, with a maximum increase of conductance of 600%. The ohmically contacted wires show a ratio between one and two for conductance and less than a two-fold increase in peak current

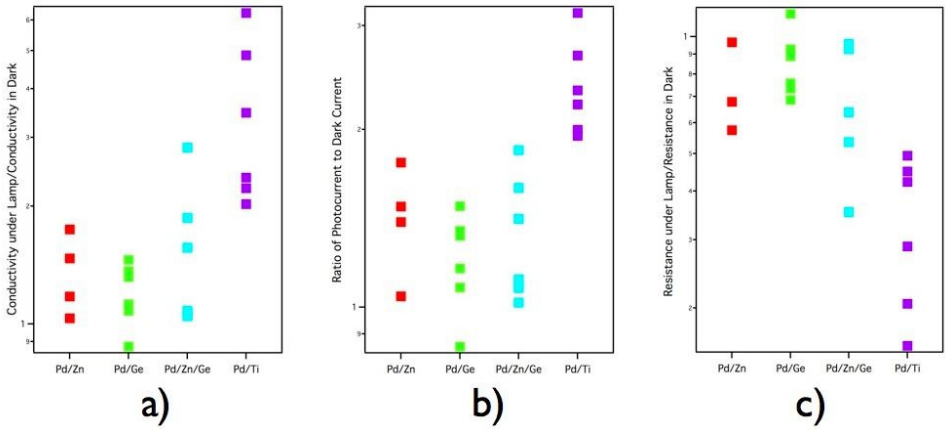

Figure 4.12: Light response parameters in wires contacted with different electrode recipes. Each parameter is a ratio of the value under light/value in dark. a)Conductivity b)Resistance c)Peak Current

4.6 Gate Response

Despite reporting on MSM devices, we can use a third terminal to extract some important parameters as far as the behavior of the nanowires. By using the substrate to gate the wires, we can clearly see that they are initially p-type. Gating across the 200nm silicon dioxide dielectric does not provide strong coupling but it can provide some information on the carriers within the device. We use a standard method to extract the mobility of carriers within the wire, with the understanding that this value is not a real measure of the mobility but more a good figure of merit to describe the gating effect that accounts for the nanowire diameter and length in the analysis. A simple analysis of the transconductance can provide information on the carrier mobility in the wire using the following:

$$C_{ox} = \frac{2\pi\epsilon_o\epsilon_r L}{cosh^{-1}(\frac{r+t_{ox}}{r})} and \mu = \frac{dI_{ds}}{dV_{gs}}\frac{L^2}{C_{ox}}\frac{1}{V_{ds}} \tag{4.1}$$

where L is the device length, t_{ox} is the oxide thickness, r is the nanowire radius

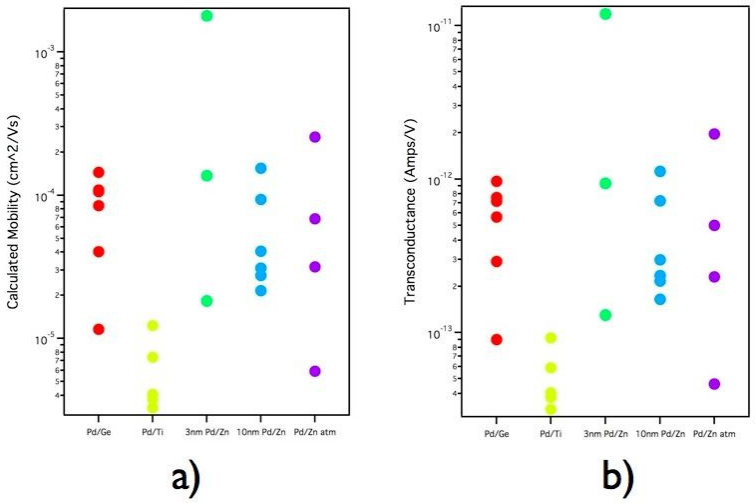

Figure 4.13: Gating Parameters for different recipes

[90]. This will not provide a true mobility in our case, it does not

account for surface states or many other complicating factors and has in fact been shown to only be a rough estimate of the mobility even in systems lending themselves to its use [128]. Fig 4.13 shows a plot of the calculated mobility and transconductance vs recipe. Here, the palladium/titanium shows smaller transconductance values providing more evidence that the device is a Schottky contacted MSM since the contacts dominate and the channel carrier concentration affects the conductance to a much smaller extent than with ohmic contacts. Ohmic wires have transconductances around $10^{-}12$ Amps/Volt and calculated mobilities between $10^{-}4$ $cm^2/V-s$, both very low values for these metrics. This plots show that the 10nm palladium/zinc contacts show a more consistent result in vacuum. However the final column in the plots is these same devices measured in atmosphere. In the next section, the second limiting factor in device fabrication will be explored. The large surface to volume ratio of these nanowires makes them particularly susceptible to defects and energy states created by dangling bonds at the surface. GaAs is well known to suffer greatly

due to these states in bulk devices. Controlling these states present a significant obstacle to the creation of high performance devices using nanowires.

4.7 Surface Effects

At this stage, an ohmic contact appears to have been fabricated on the GaAs nanowires. The contacts are fairly stable in temperature and air and only small differences can be extracted due to variations in palladium thickness, dopant material and anneal time. Anneal temperature however has shown itself to greatly affect the results, with devices annealed over 425C yielding primarily non-conducting wires. Wires were also annealed as low as 300C for several minutes with good results. To understand the source of the inconsistent results, we can examine other possible sources of differences in the nanowire devices. It is well known that surface effects can have a strong effect on device performance [129; 106; 130]. Researchers have studied the GaAs surface carefully and identified several compounds that can exist such as gallium oxide in different forms and arsenic oxides. The large surface to volume ratio of the wires makes them very susceptible to these surface contaminants. Initially the devices were measured in atmosphere to observe any possible differences with their behavior under vacuum. The motivation being that changing the surrounding atmosphere can drastically change the surface makeup and provide an indication of the effect it may be having. Surface depletion can extend deep into a undoped GaAs semiconductor. A simple calculation using:

$$R = \frac{L}{qp\mu_p\pi(r-d)^2} where d = \sqrt{\frac{2\epsilon_o\epsilon_r V_s}{qN_a}} \tag{4.2}$$

Shows that a slight offset of the pinned Fermi level value at the surface can deplete almost the entire wire. It has also been shown that due to the nanoscale nature of the surface, nanowires can have a critical radius that depletes the entire wire prior to

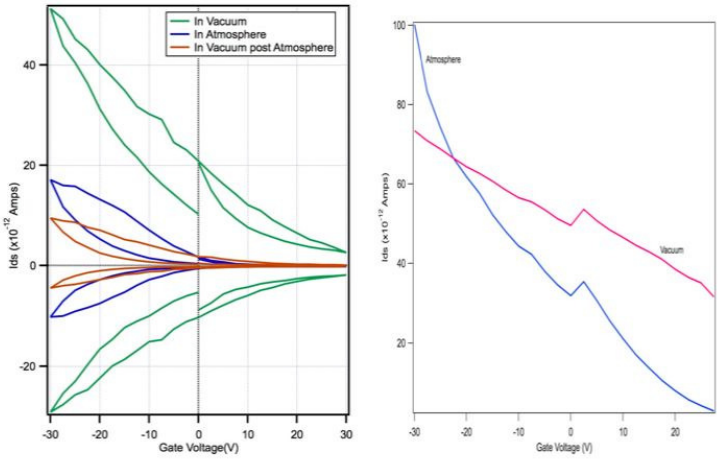

Figure 4.14: a) Device current as a function of gate voltage under different atmospheric conditions on a palladium/zinc contacted wires b) Simple comparison of gating of a nanowire under vacuum and in atmospheric conditions

the calculated depletion length reaching the radius [131].

Fig 4.14 shows a sequence of current vs gate voltage traces taken first in vacuum, then in atmospheric conditions and then again in vacuum conditions. The results show the strong effect that the surface and surrounding environment can have on the nanowire devices electrical properties. The peak current drops to less than half of its value in vacuum when exposed to air. Even more interesting is that a return to vacuum does not return the trace to its original levels and in fact the trace continued to decline. Characterization done several days later on this device, after remaining in vacuum the entire time, saw the currents increase once again. Fig 4.14b shows another nanowire's response in vacuum and atmosphere, what is interesting is the increased transconductance in air, an unexpected result for these devices based on measurements of other nanoscale devices. The surface issues present a serious problem to the ability to fabricate GaAs nanowire devices that perform consistently, they do however demonstrate strongly that these devices have strong possibilities in the world

of particle and pathogen detection.

4.7.1 Passivation

A method to further test the surface effects is to attempt to passivate the surface of the nanowire to prevent pinning by native oxides and other deposited material. The most common used passivation in GaAs is ammonium sulfide. Soaking in the ammonium sulfide solution removes the native oxide and replaces the oxygen molecules with sulfur atoms. The sulfur-gallium and sulfur-arsenic bonds coat the surface and unpin the Fermi level [132; 133; 134; 135; 136; 137]. This method has already been seen to be beneficial in indium-arsenide nanowires [138]. In order to test this technique, nanowire devices were passivated post fabrication and immediately tested to examine the effects of the passivation. The ohmic contacts presented react strongly with ammonium, so a new set of devices using only titanium/gold were fabricated to test the effects of sulfur. The samples were tested prior to passivation and after. As a test, the devices were also annealed at 400C in nitrogen to ensure that the annealing step in the passivation did not affect the contacts. The initial anneal showed only small changes in the current-voltage characteristics of the devices. The passivation was performed using 10% ammonium sulfide in water, several grams of elemental sulfur were added to the solution to saturate it. The solution was mixed at 40C and then filtered to remove the precipitate that forms from some of the excess sulfur. The nanowire devices were then dipped in an oxide removing solution of ammonium for 15 seconds and immediately placed in the passivation solution at 40C and under lamp light. The heat and lamp light are known to assist in the surface reaction by creating carriers within the material. The sample is soaked for 10 minutes, rinsed in deionized water and blown dry with nitrogen. To complete the reaction, the sample is then annealed for 20 sec at 400C in nitrogen. The anneal is used to harden the

passivation. Temperatures of 400C and above are known to transfer the sulfur bonds from arsenic to gallium and remove the elemental arsenic from the surface, leaving a stronger coating of gallium-sulfide material. After annealing, the device is measured in atmosphere. Fig 3.15 shows the results of the passivation on a representative wire. The bottom two traces show the same device before passivation measured in vacuum and in atmosphere. The top trace is the result of passivation. The passivation increased the peak current by almost one hundred times. This result also remained for several days after the passivation was complete. All wires passivated showed an increase in conductivity. However, the traces while much larger, also become considerably noisier and inconsistent. These results have also been seen in palladium/zinc based contacts but with more varied results. Charging effects could also be seen as hysteresis developed between the increasing voltage and decreasing voltage traces. The effect of the passivation on the contacts is relatively unknown and ideally the nanowires would be passivated prior to device fabrication. There are several levels of complications to accomplishing this however. The preliminary results make the goal of developing a recipe that allows pre-passivation that does not deteriorate over time an attractive one for GaAs nanowires.

4.8 Core-Shell Nanowires

The sulfur passivation provides an excellent method to passivate the surface and remove the effects of surface depletion. An even stronger method is the growth of a passivation layer in the form of aluminum gallium arsenide (AlGaAs) creating a core-shell wire material. An AlGaAs layer can serve to remove the depletion formed by the surface and also to confine carriers to the core. It also creates a heterostructured wire, with the possibility of enjoying many of the benefits seen in bulk devices. Core-shell wire devices have been reported on extensively in the literature [139; 140; 107; 96; 97;

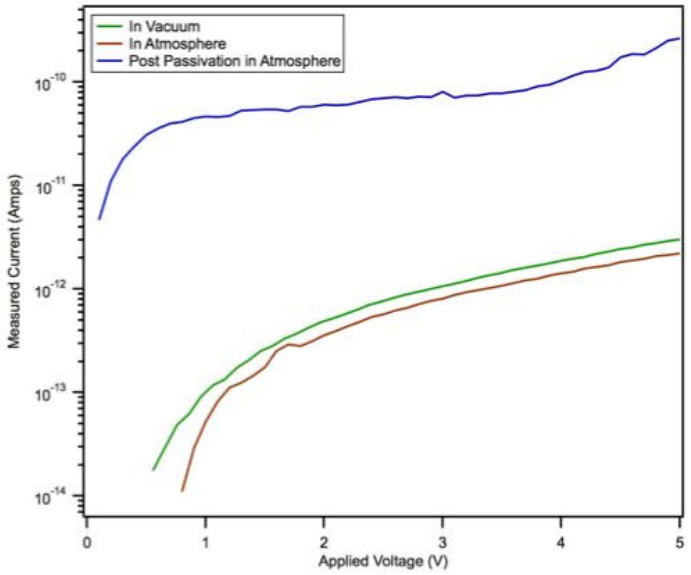

Figure 4.15: IV traces under in vacuum, in atmosphere and post passivation treatment in atmosphere on a titanium/gold contacted nanowire

141; 142]. Some of these devices have shown ballistic conduction and demonstrated transistor properties comparable to some of the best performing bulk devices. In the case of AlGaAs/GaAs wires, there is again a large published body of work on the photoluminescence properties but little work on using these structures as devices. Here we will attempt to apply the same techniques used on the GaAs wires to the core shell wires in hopes of improving the light responsivity and electrical properties of nanowire devices. Previous GaAs based core-shell electrical investigations have centered on creating p-type:intrinsic:n-type structures in GaAs, with an n-doped core, an intrinsic inner shell and a p-type outer shell. This device have been demonstrated as a strong photodetectors [111]. The core-shell nanowires described here were grown in the same manner as the GaAs nanowires described previously [143]. The shell is grown by standard metal-organic vapour phase epitaxy on the GaAs nanowires as described previously at 650C. The resulting nanowires have a GaAs core of 50 60nm

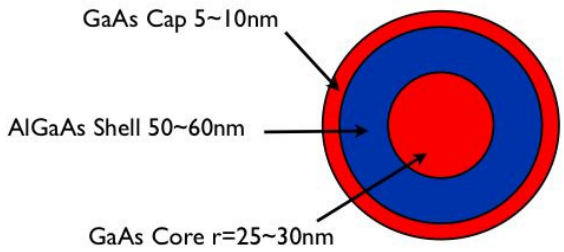

Figure 4.16: Diagram of core shell nanowire structure

in diameter with an AlGaAs shell with thickness 50 60nm and a thin GaAs capping layer of 5 10nm to prevent oxidation of the AlGaAs and defect formation in the core as shown in Fig 4.16. Fig 4.17 shows transmission electron microscope image of the core shell wires taken. The aluminum content is the shell is estimated at 30%

Devices made using the core-shell nanowires were fabricated with the same methods outlined for GaAs nanowires. The contact recipes were kept the same and annealing conditions were also maintained. For some samples, described later the nanowire shell was patterned etched prior to metal deposition in order to remove the capping layer and a portion of the shell. This was done using a mild piranha etch of $H_2SO_4/H_2O_2/H_2O$ (1:8:1000) providing an easily controllable slow etch rate. After

calibration of the etch, the rate was determined to be about 60-80nm/min and the etched wires were etched for 30 sec to partially remove the cap and shell. The etch solution operates by creating an oxide using the hydrogen peroxide and then removing it with the sulfuric acid. For this reason the wires are still dipped in oxide removing solution just prior to metal deposition, since the etching solution leaves an oxide layer on the etched region.

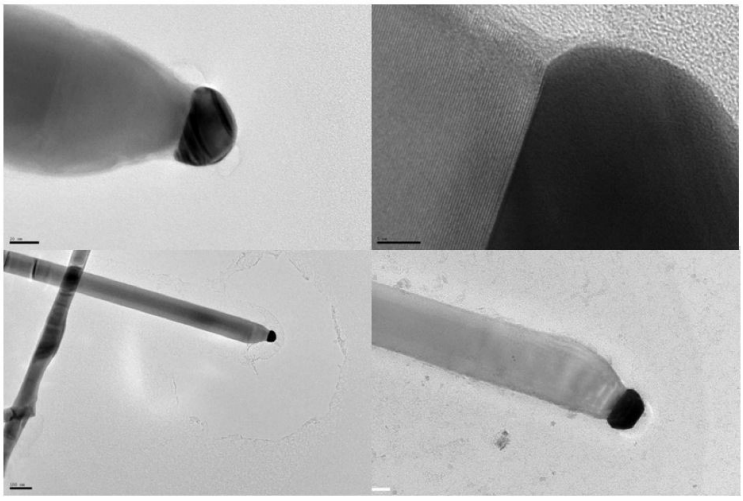

Figure 4.17: Transmission electron microscope images of core shell nanowires

4.8.1 Unetched Core-Shell Devices

Fig 4.18 shows the results of contacting the coreshell nanowires with the different recipes used in the GaAs nanowire devices. For these devices the unetched palladium/zinc contacts showed considerably more consistent results, with peak currents at three volts in the picoamp range and resistances again near one gigaohm. The resistances for the palladium/germanium contacted wires were consistently higher, possibly owing to the larger bandgap of the AlGaAs shell. The palladium/titanium and etched palladium/zinc devices showed very low dark currents.

4.8.2 Light Response

Core-shell nanowires offer many of the benefits for light detection mentioned in Chapter 2 and have already shown themselves to be excellent candidates for a wide array of high performance detectors [144; 142; 145] Fig **??** plots the light response ratios for the core shell devices. Here we see a considerable increase in the light response of the devices. It must be considered that the incident light contains wavelengths that

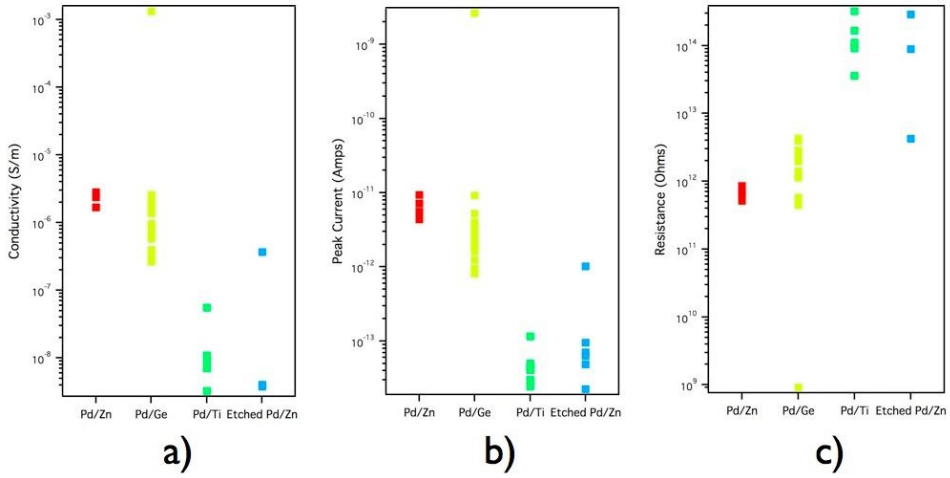

Figure 4.18: Extracted parameters for core-shell nanowires contacted by different electrode recipes

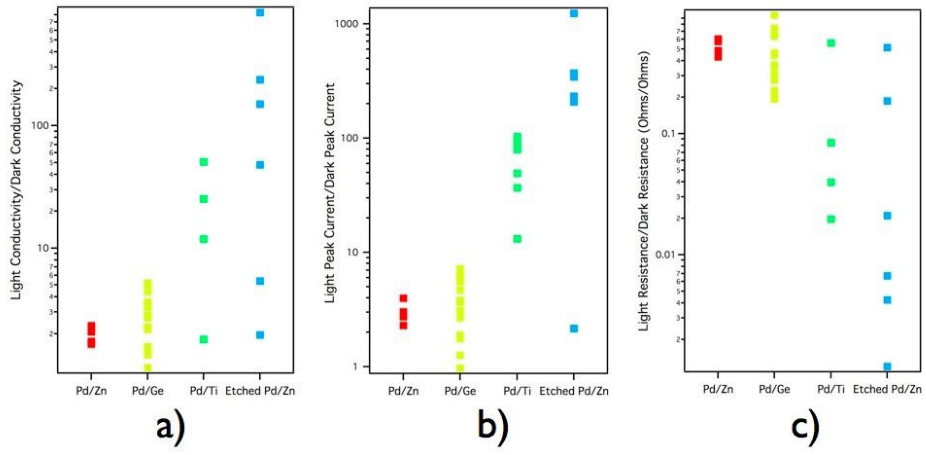

Figure 4.19: Light response parameters for core shell nanowires, all plots are of the ratio of the value under light/value in dark

will also be absorbed by the AlGaAs layer, so part of the improved light response can simply be attributed to an increase in the absorbing area with the addition of the AlGaAs shell. This factor can account for the somewhat improved response of the unetched palladium/zinc and the palladium/germanium devices but not the tremendous increase in responsivity seen in the palladium/titanium and etched palladium/zinc devices. The palladium/titanium devices show a change of conductivity in the range of thirty times the dark value. The etched palladium/zinc devices, while very inconsistent show peak values larger than 500 times dark current under light. The difference in the etched and unetched palladium/zinc contacts is striking and worthy of further discussion. Current-voltage traces of the palladium/titanium devices in light demonstrated two distinct behaviors, with representative traces shown in Fig 4.20. In a) we see what might be the expected result from a typical bulk schottky contacted AlGaAs/GaAs detector, in fact the voltage knee seen is close to 2V, the same as that seen in the 2DEHG devices discussed previously. In the b) we see a much more surprising effect, negative differential resistance. This effect was clearly seen in two of the devices with palladium/titanium contacts and investigations into its origins are ongoing. These devices show

promising results and possibilities for use as high speed photodetectors similar to the devices presented in Chapter 2. The nanowire devices have several advantages over bulk devices. With no substrate, the long tail often generated by carriers generated deep within the material would be eliminated. The nanowires could also easily be placed on top of a Bragg reflector and also be encased in an anti-reflecting coating for both improved absorption and passivation and protection of the surface of the material. The devices also demonstrate a strong effect associated with the surrounding environment, with conductance values changing with changes in the pressure at which they are measured. Substrate gating was also performed on the Core Shell wires, with

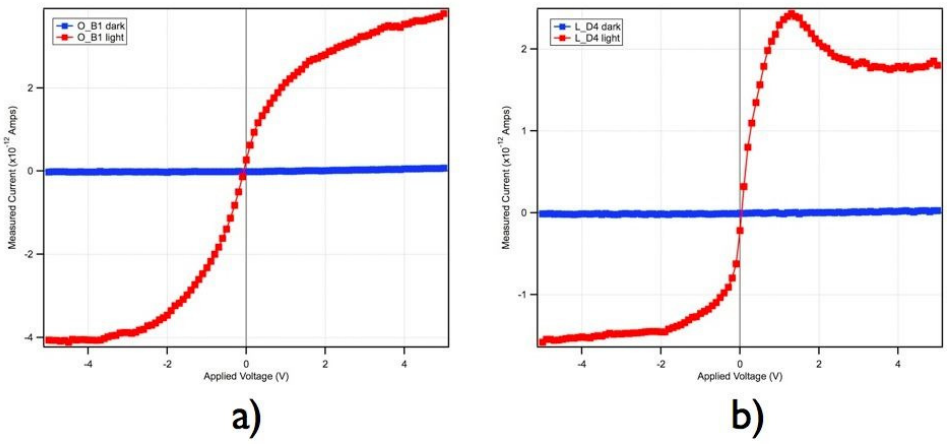

Figure 4.20: Representative current-voltage traces of palladium/titanium contacted core shell wires in dark and under light

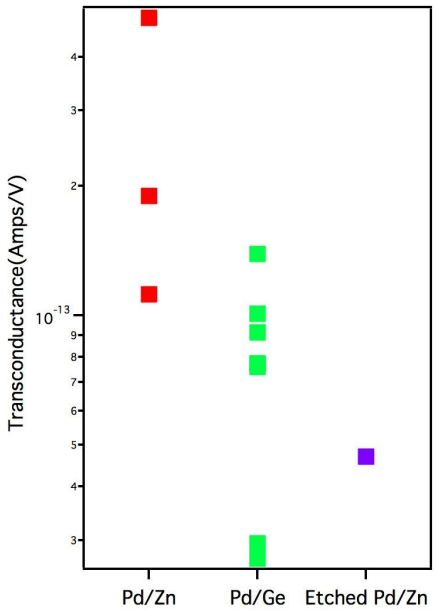

Figure 4.21: Transconductance extracted from core shell nanowires of different contact recipes

the unetched palladium/zinc contacts again showing the highest transconductance, in the low 10-13A/V range, as shown in Fig 4.21. The etched palladium/zinc showed only a slight gate dependence, similar to the palladium/titanium contacts on GaAs.

4.8.3 Etched Devices

The etching was intended to remove the GaAs cap and some of the underlying shell to place the contact closer to the core and allow zinc diffusion to move through the AlGaAs and into the core, creating an ohmic contact. The result obtained was quite different than that expected. The devices showed a very small, at times unmeasurable dark current and a large photoresponse. The reason for this behavior is still being explored but there are several possibilities to consider. The simplest is that the GaAs cap provides a lower barrier for carriers to enter the wire and conduction may take place in the cap layer or carriers may then move into the core. When the cap is etched, the larger barrier created by the AlGaAs blocks carriers. This explanation while possible, must assume that conduction takes place in the GaAs cap which passivation experiments indicate should be strongly depleted. The growth of the AlGaAs shell is done at several different precursor pressures. It has been shown with optical characterization, that the ratio of III-V precursor present during growth can change the observed photoluminescence spectra obtained from the wires. Our collaborators have proposed that silicon contaminants in the aluminum precursor can dope the shell n-type when the III-V precursor ratio is low, creating

an n-type AlGaAs shell. Assuming this is true, when the palladium/zinc contacts are placed on the etched wire, the zinc that diffuses into the shell will begin to compensate dope the shell and reduce its conductivity instead of increasing it. This possibility may explain the behavior observed, the zinc compensates the unintentional dopants and the palladium then acts as a Schottky contact to low conductivity Al-

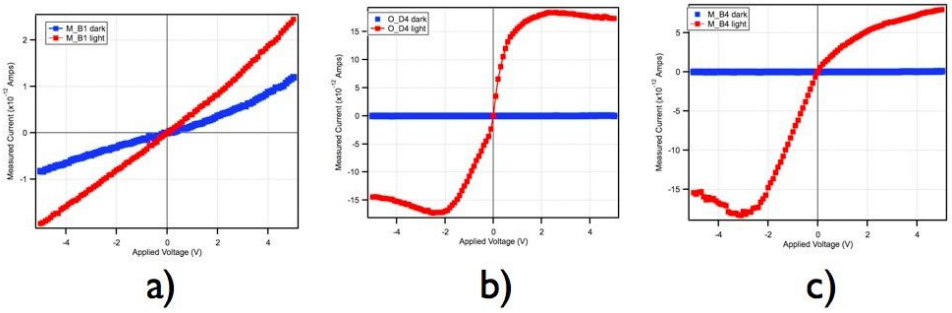

Figure 4.22: Representative current-voltage traces in dark and under light of core shell nanowires contacted with palladium/zinc contacts and cap etched prior to contact deposition

GaAs. Fig 4.22 shows a set of etched core shell current-voltage traces in dark and under light. There is a wide variety of behaviors, as seen in the conductivity and resistance plots earlier. Trace a) shows similar behavior to an unetched core shell nanowire. The remaining traces show behavior more similar to the unetched palladium/titanium devices. Several traces exhibit the negative differential resistance also seen in the palladium/titanium contacts. This result has proven to be repeatable with several chips of similar nanowires fabricated in the same manner and demonstrating similar results. In order to understand the behavior of these devices more completely local excitation techniques are being used to study the potential profile within the wire.

4.8.4 Ambipolar Transport in a Core-Shell Nanowire

The unetched palladium/zinc core shell nanowires were patterned with hafnium oxide dielectric to add strong coupled gates to the devices [146; 147]. The hafnium oxide was deposited using low temperature atomic layer deposition in a Cambridge Nanotech system. The gate electrodes were patterned to overlap the contacts slightly to provide gating to the entire wire. Fig 4.23 shows the patterned dielectric material

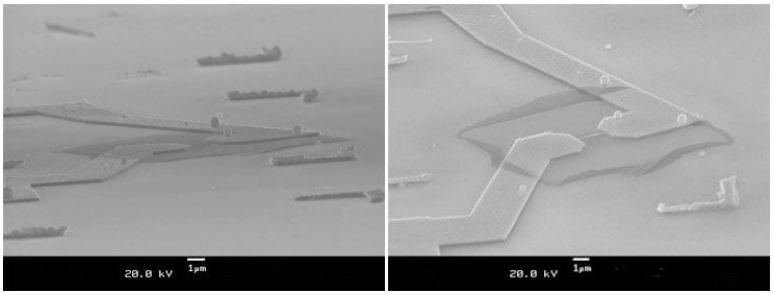

Figure 4.23: Scanning electron microscope image of hafnium oxide deposited as gate dielectric on core-shell nanowire devices

after lift-off. The low temperature process allows the use of PMMA to pre-pattern the substrate prior to deposition. Lift-off is done in acetone. The gate metal is titanium/gold. Ambipolar gating in wide bandgap material is unusual. The gate coupling must be strong enough to move the Fermi level from slightly p-type to n-type. The transconductance for this device in the p-type region is $8.53 * 10^{-13}$A/V and in the n-type region is $5.86 * 10^{-13}$A/V. These results are preliminary and work continues on fabricating these three terminal devices to test these nanowires as high performance transistors, similar to high electron mobility transistors devices in bulk.

4.9 Future Work

To further improve these devices, methods of passivation and encapsulation are being developed to control the surface state of the wire. A candidate technique for this is using a combination of silicon dioxide and hafnium oxide. This would allow optimization of the device, prevent surface level pinning and ease the optimization of device contact recipes. The devices are also being further characterized using local excitation techniques such as scanning gate measurements and electron beam induced current [94; 148; 149; 150]. Utilizing the same capacitance-voltage characterization techniques shown in Chapter 2 is also a powerful tool for gaining insight into the

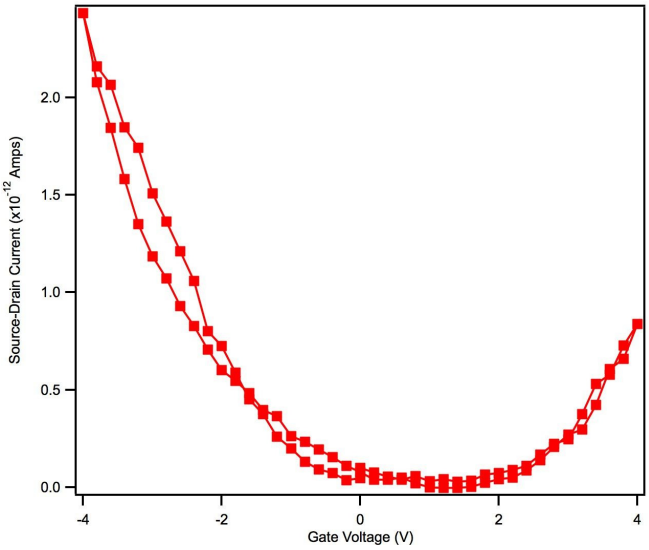

Figure 4.24: Device current as a function of gate voltage for hafnium oxide coated core shell nanowire at 3V electrode bias

nanowire properties and has been accomplished on nanowires in recently published work [151].

5. Conclusions and Contributions

The exploration into the two included GaAs-based material systems in the context of devices, particularly optical detectors revealed many important and useful features for future designs.

5.1 Two-dimensional Electron-Hole Gas Devices

The two dimensional electron hole gas was successfully implemented into an MSM optical detector with performance superior to single well devices demonstrated previously. The combination of the underlying Bragg reflector and the dual quantum well structure successfully eliminated the long tail in the high speed optical response that had plagued previous high speed devices. The devices also demonstrated a high wavelength selectivity and linear operation at larger incident powers. The Bragg devices in particular had very low dark current, generating a large signal to noise ratio.

Aside from demonstrating excellent properties for a high speed photodetector, the material also shows potential to be a useful varactor. The unique and interesting low frequency response of the devices showed a dual plateau structure, potentially allowing higher precision in switching capacitance. The development of 'wings' under large incident intensities was evidence that the channel itself can participate in capacitance, which is typically determined solely by the contact and the area directly beneath.

Photoluminescence measurements revealed a rich and complex potential landscape within the material. A strong, Bragg enhanced photoluminescence peak emitted from the substrate with an underlying Bragg reflector was observed. The results also confirmed the simulated band diagram, establishing that the layered structure designed produced the desired results. Several peaks emerged from the photoluminescence data

that are as yet unidentified. These unidentified peaks demonstrated a very low temperature dependence, a feature not often seen in semiconductor photoluminescence.

The optical interrogation also revealed the possible role that diffusion may play in the behavior of devices. The dual quantum well structure offers an excellent environment for charge carrier diffusion by providing wells that separate carriers and inhibit recombination, as well as high mobility channels for carriers to travel in. Large carrier buildup at the point of illumination or due to a fabricated interface may create opportunities for carriers to quickly diffuse away, possibly traveling long distances before recombining.

5.2 GaAs-based Nanowire Devices

The issues related to fabrication of ohmic contacts were overcome and the first known ohmic contacts to undoped GaAs nanowires were fabricated. This was accomplished by utilizing shallow ohmic contact recipes that were modified and studied to find the lowest resistance contact reported. Optimization was explored in terms of contact recipe, ratio of materials in the contacts, annealing temperature and annealing time. The wires revealed a strong tolerance for post-processing, providing a large window for producing quality contacts.

Several different recipes were explored, resulting in ohmically contacted wires and stable Schottky contacts. The Schottky contacted devices revealed a strong light dependence, providing evidence that these nanowires will make high performance photodetectors.

The effects of the surface of the nanowires was also explored, demonstrating that sulfur passivation of the surface of an already contacted device increased the current almost two orders of magnitude. The devices however had significantly increased noise levels and large levels of hysteresis in the current-voltage characteristics.

To further explore and optimize the devices, core-shell nanowires were investigated. The shell serving as a strong passivation layer for the inner GaAs core. These devices were contacted with the recipes used for the single GaAs nanowires. Several device configurations were explored, including an attempt to make contact directly to the core by etching the shell on either end of the nanowire. The strongly blocking contacts obtained were unexpected, as the palladium/zinc contact had produced the best ohmic contacts on the bare GaAs wires and on the unetched core-shell wires as well. Under light however, a large signal was generated. These devices, along with the wires contacted with palladium/titanium directly on the shell produced a large photoresponse. Several of the devices also demonstrated negative differential resistance, a behavior that is presently under investigation.

Finally, the gate response of wires, using hafnium oxide as a gate dielectric, was investigated. Ohmically contacted core-shell wires showed ambipolar transport in gate voltage sweeps. This was an unexpected but interesting result. Ambipolar transport in wide band gap materials is difficult to produce. These results provided some insight into the internal potential landscape and the density of unintentional dopants within the wires.

Both material systems explored demonstrated strong potential as viable optical detectors. The dual well structure holds promise as a monolithically integratable high speed optical detection, as well as showing potential applications in varactor devices. Nanowire devices were demonstrated as potential nanoscale optical detectors, possibly for on-chip optical interconnects. The also demonstrated strong potential for electronic components when ohmic contacts are fabricated.

Bibliography

[1] S.Heinze, J.Tersoff, R.Martel, V.Derycke, J.Appenzeller, and Ph.Avouris, "Carbon nanotubes as schottky barrier transistors," *Physical Review Letters*, vol. 89, no. 10, 2002.

[2] S.J.Tans, M.H.Devoret, H.Dai, A.Thess, R.E.Smalley, L.J.Geerligs, and C.Dekker, "Individual single-wall carbon nanotubes as quantum wires," *Nature*, vol. 386, 1997.

[3] K.S.Novoselov, A.K.Geim, S.V.Morozov, D.Jiang, Y.Zhang, S.V.Dubonos, I.V.Grigorieva, and A.A.Firsov, "Electric field effect in atomically thin carbon films," *Science*, vol. 306, no. 5696, pp. 666–669, 2004.

[4] Ph.Avouris, "Carbon nanotube electronics," *Chemical Physics*, vol. 28, no. 2-3, 2002.

[5] P.L.McEuen, M.S.Fuhrer, and H.Park, "Single-walled carbon nanotube electronics," *IEEE Transactions on Nanotechnology*, vol. 1, no. 1, 2002.

[6] D.C.Olson, J.Piris, R.T.Collins, S.E.Shaheen, and D.S.Ginley, "Hybrid photovoltaic devices of polymer and zno nanofiber composities," *Thin Solid Films*, vol. 496, no. 1, 2006.

[7] N.J.Pinto, A.T.Johnson, A.G.MacDiarmid, C.H.Mueller, N.Theofylaktos, D.C.Robinson, and F.A.Miranda, "Electrospun polyaniline/polyethylene oxide nanofiber field-effect transistor," *Applied Physics Letters*, vol. 83, no. 4244, 2003.

[8] A.N.Aleshin, "Polymer nanofibers and nanotubes: Charge transport and device applications," *Advanced Materials*, vol. 18, no. 1, pp. 17–27, 2005.

[9] J.Goldberger, D.J.Sirbuly, M.Law, and P.Yang, "Zno nanowire transistors," *Journal of Physical Chemistry B*, vol. 109, no. 1, pp. 9–14, 2005.

[10] H.Shirakawa, "Nobel lecture: The discovery of polyacetylene film - the dawning of an era of conducting polyers," *Reviews of Modern Physics*, vol. 73, 2001.

[11] A.Heeger, "Nobel lecture: Semiconducting and metallic polymers: The fourth generation of polymeric materials," *Reviews of Modern Physics*, vol. 73, no. 3, 2001.

[12] A.MacDiarmid, "Nobel lecture: "synthetic metals": A novel role for organic polymers," *Reviews of Modern Physics*, vol. 73, no. 3, 2001.

[13] S.Virji, J.Huang, R.B.Kaner, and B.H.Weiller, "Polyaniline nanofiber gas sensors: Examination of response mechanism," *Nano Letters*, vol. 4, no. 3, pp. 491–496, 2004.

[14] D.Aussawasathien, J.-H.Dong, and L.Dai, "Electrospun polymer nanofiber sensors," *Synthetic Metals*, vol. 154, no. 1-3, pp. 37–40, 2005.

[15] V.V.Sysoev, B.K.Button, K.Wepsiec, S.Dmitriev, and A.Kolmakov, "Toward the nanoscopic "electronic nose": Hydrogen vs carbon monoxide discrimination with an array of individual metal oxide and mesowire sensors," *Nano Letters*, vol. 6, no. 8, pp. 1584–1588, 2006.

[16] R.F.C.Farrow, ed., *Molecular beam epitaxy: applications to key materials*. Noyes Publications, 1995.

[17] L. Pfeiffer, K.W.West, H.L.Stormer, and K.W.Baldwin, "Electron mobilities exceeding 1e7 cm2/v-s in modulation-doped gaas," *Applied Physics Letters*, vol. 55, no. 18, 1989.

[18] S.M.Sze, ed., *High-Speed Semiconductor Devices*. John Wiley and Sons Inc, 1990.

[19] "World's fastest transistor approaches goal of terahertz device," *ScienceDaily*, 2006.

[20] T.Mimura, S.Hiyamizu, T.Fujii, and K.Nanbu, "A new field-effect transistor with selectively doped gaas/n-alxgaxas heterojunctions," *Japanese Journal of Applied Physics*, vol. 19, no. 5, 1980.

[21] T.Mimura, "Development of high electron mobility transistor," *Japanese Journal of Applied Physics*, vol. 44, 2005.

[22] A.D.Holland, A.D.T.Short, and T.Cross, "X-ray detection using bulk gaas," *Nuclear Instruments and Methods in Physics Research Section A*, vol. 346, no. 1-2, 1994.

[23] D.Walker, E.Monroy, P.Kung, J.Wu, M.Hamilton, F.J.Sanchez, J.Diaz, and M.Razeghi, "High-speed, low-noise metal-semiconductor-metal ultraviolet photodetectors based on gan," *Applied Physics Letters*, vol. 74, no. 762, 1999.

[24] X.Chen, B.Nabet, F.Quaranta, A.Cola, and M.Currie, "Resonant-cavity-enhanced heterostructure metal-semiconductor-metal photodetector," *Applied Physics Letters*, vol. 80, no. 17, 2002.

[25] V.V.Popov, T.V.Teperik, G.M.Tsymbalov, X.G.Peralta, S.J.Allen, N.J.M.Horing, and M.C.Wanke, "Tunable terahertz detection based on a grating-gated doule-quantum-well fet," *Semiconductor Science and Technology*, vol. 19, pp. S71–S73, 2004.

[26] Y.Huo and G.W.Taylor, "Analysis of terahertz detection with a 2d hot-electron quantum well detector," *Microwave and Optical Technology Letters*, vol. 37, no. 4, 2003.

[27] F.Teppe, D.Veksler, V.Yu.Kachorovski, A.P.Dmitriev, X.Xie, X.-C.Zhang, S.Rumyantsev, W.Knap, and M.S.Shur, "Plasma wave resonant detection of femtosecond pulsed terahertz radiation by a nanometer field-effect transistor," *Applied Physics Letters*, vol. 87, no. 022102, 2005.

[28] M.I.Dyakonov and M.S.Shur, "Plasma wave electronics: Novel terahertz devices using two dimensional electron fluid," *IEEE Transactions on Electron Devices*, vol. 43, no. 10, 1996.

[29] W.Knap, Y.Deng, S.Rumyantsev, J.-Q.Lu, M.S.Shur, C.A.Saylor, and L.C.Brunel, "Resonant detection of subterahertz radiation by plasma waves in a submicron field-effect transistor," *Applied Physics Letters*, vol. 80, no. 3433, 2002.

[30] A.Juozapavisius, L.Ardaravicius, A.Suziedelis, A.Kozic, J.Gradauskas, J.Kundrotas, D.Seliuta, E.Sirmulis, S.Asmontas, G.Valusis, H.G.Roskos, and K.Kohler, "Microwave sensor based on modulation-doped gaas/algaas structure," *Semiconductor Science and Technology*, vol. 19, pp. S436–S439, 2004.

[31] E.Myers, "Electron beam induced current detection of sub-surface two-dimensional charge reservoir," Master's thesis, Drexel University, 2008.

[32] S.M.Luber, K.Adlkofer, U.Rant, A.Ulman, A.Golzhauser, M.Grunze, D.Schuh, M.Tanaka, M.Tornow, and G.Abstreiter, "Liquid phase sensors based on chemically functionalized gaas/algaas heterostructures," *Physica E*, vol. 21, pp. 1111–1115, 2004.

[33] D.Gassull, S.M.Luber, A.Ulman, M.Grunze, M.Tornow, G.Abstreitera, and M.Tanaka, "ph sensitivity of gallium arsenide (gaas) electrodes functionalized with methyl-mercaptobiphenyl monolayers," *Journal of Physical Chemistry*, vol. 111, pp. 12414–12419, 2007.

[34] S.M.Sze, D. Jr., and A.Loya, "Current transport in metal-semiconductor-metal (msm) structures," *Solid-State Electronics*, vol. 14, pp. 1209–1218, 1971.

[35] G.Zhu, X.Zhou, T.S.Lee, L.K.Ang, G.H.See, S.Lin, Y.-K. Chin, and K.L.Pey, "A compact model for undoped silicon-nanowire mosfets with schottky-barrier source/drain," *IEEE Transactions on Electron Devices*, vol. 56, no. 5, 2009.

[36] Z.Y.Zhang, C.H.Jin, Z.L.Liang, Q.Chen, and L.-M.Peng, "Current-voltage characteristics and parameter retrieval of semiconducting nanowires," *Applied Physics Letters*, vol. 88, no. 073102, 2006.

[37] D.K.Schroder, *Semiconductor Material and Device Characterization*. Wiley Interscience, third edition ed., 2006.

[38] X. Zhao, *Carrier transport in high-speed photodetectors based on two-dimensional-gas*. PhD thesis, Drexel University, 2007.

[39] J.Bardeen, "Surface states and rectification at a metal semi-conductor contact," *Physical Review*, vol. 71, no. 10, 1947.

[40] R.Tung, "Recent advances in schottky barrier concepts," *Materials Science and Engineering: R*, vol. 35, no. 1-3, 2001.

[41] D.K.Ferry, *Semiconductors*. Macmillian Publishing Company, 1991.

[42] W.P.Leroy, K.Opsomer, S.Forment, and R. Meirhaeghe, "The barrier height inhomogeneity in identically prepared au/n-gaas schottky barrier diodes," *Solid-State Electronics*, vol. 49, no. 6, 2005.

[43] J.P.Sullivan, R.T.Tung, M.R.Pinto, and W.R.Graham, "Electron transport of inhomogeneous schottky barriers: A numerical study," *Journal of Applied Physics*, vol. 70, no. 12, 1991.

[44] A.Bengi, S.Altindal, S.Ozcelik, and T.S.Mammadov, "Gaussian distribution of inhomogeneous barrier height in al0.24ga0.76as/gaas structures," *Physica B*, vol. 396, pp. 22–28, 2007.

[45] F.A.Padovani and R.Stratton, "Field and thermionic-field emission in schottky barriers," *Solid-State Electronics*, vol. 9, pp. 695–707, 1966.

[46] G.D.J.Smit, S.Rogge, and T.M.Klapwijk, "Scaling of nano-schottky-diodes," *Applied Physics Letters*, vol. 81, no. 20, 2002.

[47] G.D.J.Smit, S.Rogge, and T.M.Klapwijk, "Enhanced tunneling across nanometer-scale metal-semiconductor interfaces," *Applied Physics Letters*, vol. 80, no. 2568, 2002.

[48] J.Appenzeller, M.Radosavljevic, J.Knock, and Ph.Avouris, "Tunneling versus thermionic emission in one-dimensional semiconductors," *Physical Review Letters*, vol. 92, no. 4, 2004.

[49] S. N. Mohammad, "Contact mechanisms and design principles of (schottky and ohmic) metal contacts to semiconductor nanowires," *Journal of Applied Physics*, vol. 108, no. 034311, 2010.

[50] E.-S.Liu, N.Jain, K.M.Varahramyan, J.Nah, S.K.Banerjee, and E.Tutuc, "Role of metal-semiconductor contact in nanowire field-effect transistors," *IEEE Transactions on Nanotechnology*, vol. 9, no. 2, pp. 237–242, 2010.

[51] J.Guo, J.Wang, E.Polizzi, S.Datta, and M.Lundstrom, "Electrostatics of nanowire transistors," *IEEE Transactions on Nanotechnology*, vol. 2, no. 4, 2003.

[52] R.T.Tung, "Chemical bonding and germi level pinning at metal-semiconductor interfaces," *Physical Review Letters*, vol. 84, no. 26, 2000.

[53] R.T.Tung, "Schottky-barrier formation at single-crystal metal-semiconductor interfaces," *Physical Review Letters*, vol. 52, no. 6, 1984.

[54] R.T.Tung, "Formation of an electric dipole at metal-semiconductor interfaces," *Physical Review B*, vol. 64, no. 205310, 2001.

[55] Y.Cui, Q.Wei, H.Park, and C.M.Lieber, "Nanowire nanosensors for highly sensitive and selective detection of biological and chemical species," *Science*, vol. 293, 2001.

[56] S.Liang, H.Sheng, Y.Liu, Z.Huo, and H.Shen, "Zno schottky unltraviolet photodetectors," *Journal of Crystal Growth*, vol. 225, pp. 110–113, 2001.

[57] S.Y.Chou, Y.Liu, T.Y.Hsiang, and S.Alexandrou, "Ultrafast nanoscale metal-semiconductor-metal photodetectors on bulk and low-temperature grown gaas," *Applied Physics Letters*, vol. 61, no. 7, 1992.

[58] X.Zhao, A.Cola, A.Tersigni, F.Quaranta, E.Gallo, J.E.Spanier, and B.Nabet, "Optically modulated high-sensitivity heterostructure varactor," *IEEE Electron Device Letters*, vol. 27, September 2006.

[59] M.I.Dyakonov and M.S.Shur, "Plasma wave electronics: Novel terahertz devices using two dimensional electron fluid," *IEEE Transactions on Electron Devices*, vol. 43, no. 10, 1996.

[60] X.Zhao, A.Cola, A.Tersigni, F.Quaranta, E.Gallo, J.E.Spanier, and B.Nabet, "Optically modulated high-sensitivity heterostructure varactor," *IEEE Electron Device Letters*, vol. 27, September 2006.

[61] A.Anwar, B.Nabet, R.Ragi, J.E.Manzoli, and M.A.Romero, "Gate controlled 2-deg varactor for vco applications in microwave circuits," *Microelectronics Journal*, vol. 33, pp. 495–500, 2002.

[62] X.Melique, A.Maestrini, R.Farre, P.Mounaix, M.Favreau, O.Vanbesien, J.-M.Goutoule, F.Mollot, G.Beaudin, T.Narhi, and D.Lippens, "Fabrication and performance of inp-based heterostructure barrier varactors in a 250ghz waveguide tripler," *IEEE Transactions on Microwave Theory and Techniques*, vol. 48, no. 6, 2000.

[63] H.L.Stormer, A.Pinczuk, A.C.Gossard, and W.Wiegmann, "Influence of an undoped (alga)as spacer on mobility enhancement in gaas-(alga)as superlattices," *Applied Physics Letters*, vol. 38, no. 9, 1981.

[64] M.S.Shur, W.C.Peatman, H.Park, W.Grimm, and M.Hurt, "Novel heterodimensional diodes and transistors," *Solid-State Electronics*, vol. 38, no. 9, 1995.

[65] X.Zhao, M.Currie, A.Cola, F.Quaranta, E.Gallo, J.E.Spanier, and B.Nabet, "Time response of a two-dimensional gas-based vertical field metal-semiconductor-metal photodetectors," *IEEE Transactions on Electron Devices*, vol. 55, no. 7, 2008.

[66] A.Anwar and B.Nabet, "Barrier enhancement mechanisms in heterodimensional contacts and their effect on current transport," *IEEE Transactions on Microwave Theory and Techniques*, vol. 50, no. 1, 2002.

[67] K. D. Gupta, "Transport measurements on electron hole bilayers," *Lecture*, 2009.

[68] U.Sivan, P.M.Solomon, and H.Shtrikman, "Coupled electron-hole transport," *Physical Review Letters*, vol. 68, no. 8, 1992.

[69] J.A.Koegh, K. D. Gupta, H.E.Beere, D.A.Ritchie, and M.Pepper, "Fabrication of closedly spaced, independently contacted electron-hole bilayers in gaas-algaas heterostructures," *Applied Physics Letters*, vol. 87, no. 202104, 2005.

[70] K.Takashina, N.Nishiguchi, Y.Ono, A.Fujiwara, T.Fujisawa, Y.Hirayama, and K.Muraki, "Electrons and holes in a 40nm thick silicon slab at crogenic temperatures," *Applied Physics Letters*, vol. 94, no. 142104, 2009.

[71] M.Pohit, M.Lynass, J.G.S.Lok, W.Dietsche, K.v.Klitzing, K.Eberl, and R.Muhle, "Closely spaced and separately contacted two-dimensional electron and hole gases by in situ focused-ion implantation," *Applied Physics Letters*, vol. 80, no. 12, 2002.

[72] J.A.Seamons, D.R.Tibbetts, J.L.Reno, and M.P.Lilly, "Undoped electron-hole bilayers in gaas/algaas double quantum well," *Applied Physics Letters*, vol. 90, no. 052103, 2007.

[73] S.Glasberg, H.Shtrikman, and I.Bar-Joseph, "Optical generation of spatially separated electron and hole gases in intrinsic gaas/alxga1-xas double quantum wells," *Physical Review B*, vol. 63, no. 113302, 2001.

[74] E.H.Hwang and S. D. Sarma, "Transport and drag in undoped electron-hole bilayers," *Physical Review B*, vol. 78, no. 075430, 2008.

[75] A.F.Croxall, K. D. Gupta, C.A.Nicoll, M.Thangaraj, H.E.Beere, I.Farrer, D.A.Ritchie, and M.Pepper, "Anomalous coulomb drag in electron-hole bilayers," *Physical Review Letters*, vol. 101, no. 246801, 2008.

[76] S.Shapira, E.H.Linfield, and M.Pepper, "A simple lateral transport device of strongly interacting electron and hole layers," *Applied Physics Letters*, vol. 74, no. 11, 1999.

[77] G.J.Kalman, P.Nartmann, Z.Donko, and K.I.Golden, "Collective excitations in electron-hole bilayers," *Physical Review Letters*, vol. 98, no. 236801, 2007.

[78] K.Flensberg and B.Y.-K.Hu, "Plasmon enhancement of coulomb drag in double-quantum-well systems," *Physical Review B*, vol. 52, no. 20, 1995.

[79] H.Rubel, A.Fischer, W.Dietsche, K.v.Klitzing, and K.Eberl, "Fabrication of independently contacted and tuneable 2d-electron-hole systems in gaas/algaas double quantum wells," *Materials Science and Engineering*, vol. B51, pp. 207–211, 1998.

[80] G. Snider, *1D Poisson Solver*. University of Notre Dame, 2010.

[81] J.Woodhead, F.Gonzalez-Sanz, P.A.Claxton, and J.P.R.David, "On the band gap of ingaas/gaa strained quantum wells," *Semiconductor Science and Technology*, vol. 3, pp. 601–604, 1988.

[82] P.W.Yu, B.Jogai, T.J.Rogers, P.A.Martin, and J.M.Ballingall, "Temperature dependence of photoluminescence in modulation-doped pseudomorphic high electron mobility transistor alxga1-xas/inyga1-yas/gaas structures," *Journal of Applied Physics*, vol. 76, no. 11, 1994.

[83] C.Liao, M.Houng, and Y.Wang, "Highly selective etching of gaas on algaas using citric acid/h2o2/h2o etching system," *Electrochemical and Solide-State Letters*, vol. 7, no. 11, 2004.

[84] G.C.DeSalvo, C.A.Bozada, J.L.Ebel, D.C.Look, J.P.Barrette, C.L.A.Cerny, R.W.Dettmer, J.K.Gillespie, C.K.Havasay, T.J.Jenkins, K.Nakano, C.I.Pettiford, T.K.Quach, J.S.Sewell, and G.D.Via, "Wet chemical digital etching of gaas at room temperature," *Journal of The Electrochemical Society*, vol. 143, no. 11, 1996.

[85] A.Anwar, B.Nabet, and J.Culp, "An electrically and optically gate-controlled schottky/2deg varactor," *IEEE Electron Device Letters*, vol. 21, no. 10, 2000.

[86] X.Zhao, A.Cola, A.Tersigni, F.Quaranta, E.Gallo, J.E.Spanier, and B.Nabet, "Optically modulated high-sensitivity heterostructure varactor," *IEEE Electron Device Letters*, vol. 27, September 2006.

[87] M.Ryzhii, M.Willander, I.Khmyrova, and V.Ryzhii, "Terahertz response of metal-semiconductor-metal photodetectors," *Journal of Applied Physics*, vol. 84, no. 6419, 1998.

[88] B.Nabet, A.Cola, X.Chen, and F.Quaranta, "Photodetectors based on heterostructures for opto-electronic applications," *IEEE Transactions on Microwave Theory and Techniques*, vol. 51, no. 10, 2003.

[89] X.Chen, *Novel heterostructure metal-semiconductor-metal (HMSM) photodetectors with resonant cavity for fiber optic communication.* PhD thesis, Drexel University, 2002.

[90] D.Wang, Q.Wang, A.Javey, R.Tu, H.Dai, H.Kim, P.C.McIntyre, T.Krishnamohan, and K.C.Saraswat, "Germanium nanowire field-effect transistors with sio2 and high-k hfo2 gate dielectrics," *Applied Physics Letters*, vol. 83, no. 2432, 2003.

[91] K.Byon, D.Tham, and J.E.Fischer, "Synthesis and postgrowth doping of silicon nanowires," *Applied Physics Letters*, vol. 87, no. 193104, 2005.

[92] C.Thelander, M.T.Bjork, M.W.Larsson, A.E.Hansen, L.R.Wallenberg, and L.Samuelson, "Electron transport in inas nanowires and heterostructure nanowire devices," *Solid State Communications*, vol. 131, pp. 573–579, 2004.

[93] E.Stern, G.Cheng, E.Cimpoiasu, R.Klie, S.Guthrie, J.Klemic, I.Kretzschmar, E.Steinlauf, D.Turner-Evans, E.Broomfield, J.Hyland, R.Koudelka, T.Boone, M.Young, A.Sanders, R.Munden, T.Lee, D.Routenberg, and M.A.Reed, "Electrical characterization of single gan nanowires," *Nanotechnology*, vol. 16, pp. 2941–2953, 2005.

[94] W.Gu, H.Choi, and K.Kim, "Universal approach to accurate resistivity measurment for a single nanowire: Theory and application," *Applied Physics Letters*, vol. 89, no. 253102, 2006.

[95] Y.Cui, X.Duan, J.Hu, and C.M.Lieber, "Doping and electrical transport in silicon nanowires," *Journal of Physical Chemistry B*, vol. 104, no. 22, 2000.

[96] J.Xiang, W.Lu, Y.Hu, Y.Wu, H.Yan, and C.M.Lieber, "Ge/si nanowire heterostructures as high-performance field-effect transistors," *Nature*, vol. 441, pp. 489–493, 2006.

[97] X.Jiang, Q.Xiong, S.Nam, F.Qian, Y.Li, and C.M.Lieber, "Inas/inp radial nanowire heterostructures as high electron mobility devices," *Nano Letters*, vol. 7, no. 10, pp. 3214–3218, 2007.

[98] P.T.Blanchard, K.A.Bertness, T.E.Harvey, L.M.Mansfield, A.W.Sanders, and N.A.Sanford, "Mesfets made from individual gan nanowires," *IEEE Transactions on Nanotechnology*, vol. 7, no. 6, 2008.

[99] A.Maharjan, K.Pemasiri, P.Kumar, A.Wade, L.M.Smith, H.E.Jackson, J.M.Yarrison-Rice, A.Kogan, S.Paiman, Q.Gao, H.H.Tan, and C.Jagadish, "Room temperature photocurrent spectroscopy of single zincblend and wurtzite inp nanowires," *Applied Physics Letters*, vol. 94, no. 193115, 2009.

[100] M.Scheffler, S.Nadj-Perge, L.P.Kouwenhoven, M.T.Borgstrom, and E.P.A.M.Bakkers, "Diameter-dependent conductance of inas nanowires," *Journal of Applied Physics*, vol. 106, no. 124303, 2009.

[101] C.Soci, X.-Y. Bao, D.P.R.Aplin, and D.Wang, "A systematic study on the growth of gaas nanowires by metal-organic chemical vapor deposition," *Nano Letters*, vol. 8, no. 12, pp. 4275–4282, 2008.

[102] X.Duan, J.Wang, and C.M.Lieber, "Synthesis and optical properties of gallium arsenide nanowires," *Applied Physics Letters*, vol. 76, no. 9, 2000.

[103] P.Piccin, G.Bais, V.Grillo, F.Jabeen, S. D. Francesche, E.Carlino, M.Lazzarino, F.Romanato, L.Businaro, S.Rubini, F.Martelli, and A.Franciosi, "Growth by molecular beam epitaxy and electrical characterization of gaas nanowires," *Physica E*, vol. 37, pp. 134–137, 2007.

[104] S.-G.Ihn, J.-I.Song, Y.-H.Kim, J.Y.Lee, and I.-H.Ahn, "Growth of gaas nanowires on si substrates using molecular beam epitaxy," *IEEE Transactions on Nanotechnology*, vol. 6, no. 3, 2007.

[105] D.Stichtenoth, K.Wegener, C.Gutsche, I.Regolin, F.J.Tegude, W.Prost, M.Seibt, and C.Ronning, "P-type doping of gaas nanowires," *Applied Physics Letters*, vol. 92, no. 163107, 2008.

[106] A.D.Schricker, F. III, Ro.J.Wiacek, and B.A.Korgel, "Space charge limited currents and trap concentrations in gaas nanowires," *Nanotechnology*, vol. 17, pp. 2681–2688, 2006.

[107] J.Noborisaka, J.Motohisa, S.Hara, and F.Fukui, "Fabrication and characterization of freestanding gaas/algaas core-shell nanowires and algaas nanotubes by using selective-area metalorganic vapor phase epitaxy," *Applied Physics Letters*, vol. 87, no. 093109, 2005.

[108] S.A.Fortuna and X.Li, "Gaas mesfet with a high-mobility self-assembled planar nanowire channel," *IEEE Electron Device Letters*, vol. 30, no. 6, 2009.

[109] S.Tunich, L.Prechtel, D.Spirkoska, G.Abstreiter, A. i Morral, and A.W.Holleitner, "Photocurrent and photoconductance properties of a gaas nanowire," *Applied Physics Letters*, vol. 95, no. 083111, 2009.

[110] G.Chen, E.M.Gallo, J.Burger, B.Nabet, A.Cola, P.Prete, N.Lovergine, and J.E.Spanier, "On direct-writing methods for electrically contacting gaas and ge nanowire devices," *Applied Physics Letters*, vol. 96, 2010.

[111] C.Columbo, H.Heib, M.Gratzel, and A. i Morral, "Gallium arsenide p-i-n radial structures for photovoltaic applications," *Applied Physics Letters*, vol. 94, no. 173108, 2009.

[112] B.E.Kane, G.R.Facer, A.S.Dzurak, N.E.Lumpkin, R.G.Clark, L.N.Pfeiffer, and K.W.West, "Quantized conductance in quantum wires with gate-controlled width and electron density," *Applied Physics Letters*, vol. 72, no. 26, 1998.

[113] P.Prett, N.Lovergine, I.Miccoli, F.Marzo, J.Burger, G.Salviati, and L.Lazzarini, "Photoluminescence properties of gaas-algaas core-shell nanowires and their dependence on movpe growth conditions," in *13th European workshop on MOVPE*, (Ulm, Germany), 7-10 June 2009.

[114] O.Goktas, J.Weber, J.Weis, and K.v.Klitzing, "Alloyed ohmic contacts to two-dimensional electron system in algaas/gaas heterostructrures down to submicron length scale," *Physica E*, vol. 40, pp. 1579–1581, 2007.

[115] H.-Y.Nie and Y.Nannichi, "Pd-on-gaas schottky contact: Its barrier height and response to hydrogen," *Japanese Journal of Applied Physics*, vol. 30, no. 5, pp. 906–913, 1991.

[116] A.N.MacInnes, R.Morton, F.Radulescu, and J.McCarthy, "Processing and properties of pdge ohmic conctacts to gaas," *GaAs MANTECH*, 2000.

[117] J.S.Kwak, H.NKim, H.K.Baik, J.-L.Lee, H.Kim, H.M.Park, and S.K.Noh, "Thermally stable, low-resistance pdge-based ohmic contacts to high-low doped n-gaas," *Applied Physics Letters*, vol. 67, no. 17, 1995.

[118] L.C.Wang, S.S.Lau, E.K.Hsieh, and J.R.Velebir, "Low-resistance nonspiking ohmic contact for algaas/gaas high electron mobility transistors using ge/pd scheme," *Applied Physics Letters*, vol. 54, no. 26, 1989.

[119] Y.-T.Kim, J.-L.Lee, J.K.Mun, and H.Kim, "Pd/ge/ti/au ohmic contact to algaas/ingaas pseudomorphic high electron mobility transistor with an undoped cap layer," *Applied Physics Letters*, vol. 71, no. 18, 1997.

[120] J.J.Thompson, S.P.Beaumont, A.H.Kean, and C.R.Stanley, "Germanium-palladium ohmic contacts to n-type gaas," *Semiconductor Science and Technology*, vol. 5, pp. 596–599, 1990.

[121] Y.-T. Kim, J.-L.Lee, and B-T.Lee, "Microstructural and electrical investigation of pd/ge/ti/au ohmic contact to pseudomorphic high electron mobility transistor with undoped cap layer," *Journal of Applied Physics*, vol. 84, no. 2, 1998.

[122] E.F.Chor, D.Zhang, H.Gong, W.K.Chong, and S.Y.Ong, "Electrical characterization, metallurgical investigation, and thermal stablility studies of (pd,ti,au)-based ohmic contacts," *Journal of Applied Physics*, vol. 87, no. 5, 2000.

[123] P.Ressel, P.H.Hao, M.H.Park, Z.C.Yang, L.C.Wang, W.Osterle, P.Kurpas, E.Richter, and E. ad H.L.Hartnagel, "Pd/sb(zn) and pd/ge(zn) ohmic contacts on p-type indium gallium arsenide: The employment of the solid phase regrowth principle to achieve optimum electrical and metallurgical properties," *Journal of Electronic Materials*, vol. 29, no. 7, 2000.

[124] V.Malina, K.Vogel, P.Ressel, B.Pecz, and L.Dobos, "Related electrical and metallurgical properties of pd/zn/pd/ge and pd/zn/pd/au contact systems to p-ingap," *Phys. Stat. Sol. (a)*, vol. 184, no. 1, pp. 139–144, 2001.

[125] R.Bruce, D.Clark, and S.Eicher, "Low resistance pd/zn/pd au ohmic contacts to p-type gaas," *Journal of Electronic Materials*, vol. 19, no. 3, 1990.

[126] R.C.Brooks, C.L.Chen, A.Chu, L.J.Mahoney, J.G.Mavroides, M.J.Manfra, and M.C.Finn, "Low-resistance ohmic contacts to p-type gaas using zn/pd/au metallization," *IEEE Electron Device Letters*, vol. EDL-6, no. 10, 1985.

[127] C.Soci, A.Zhang, X.-Y. Bao, H.Kim, Y.Lo, and D.Wang, "Nanowire photodetectors," *Journal of Nanoscience and Nanotechnology*, vol. 10, pp. 1–20, 2010.

[128] O.Wunnicke, "Gate capacitance of back-gated nanowire field-effect transistors," *Applied Physics Letters*, vol. 89, no. 083102, 2006.

[129] D.Wang, Y. Chang, Q.Wang, J.Cao, D.B.Farmer, R.G.Gordon, and H.Dai, "Surface chemistry and electrical properties of germanium nanowires," *Journal of the American Chemical Society*, vol. 126, pp. 11602–11611, 2004.

[130] S.A.Dayeh, C.Soci, X.-Y.Bao, and D.Wang, "Advances in the synthesis of inas and gaas nanowires for electronic applications," *Nano Today*, vol. 4, pp. 347–358, 2009.

[131] J.H.Luscombe and C.L.Frenzen, "Depletion lengths in semiconductor nanostructures," *Solid-State Electronics*, vol. 46, pp. 885–889, 2002.

[132] P.-H.Lai, C.-W.Chen, C.-I. Kao, S.-I. Fu, Y.-Y. Tsai, C.-W.Hung, C.-H.Yen, H.-M.Chuang, S.-Y.Cheng, and W.-C.Liu, "Influences of sulfur passivation on temperature-dependendent characteristics of an algaas/ingaas/gaas phemt," *IEEE Transactions on Electron Devices*, vol. 53, no. 1, 2006.

[133] V.N.Bessolov and M.V.Lebedev, "Chalcogenide passivation of iii-v semiconductor surfaces," *Semiconductors*, vol. 32, no. 11, 1998.

[134] V.N.Bessolov, M.V.Lebedev, N.M.Binh, M.Friedrich, and D.R.T.Zahn, "Sulphide passivation of gaas: the role of sulphur chemical activity," *Semiconductor Science and Technology*, vol. 13, pp. 611–614, 1998.

[135] Y.Dong, X.M.Ding, X.Y.Hou, Y.Li, and X.B.Li, "Sulfur passivation of gaas metal-semiconductor field-effect transistor," *Applied Physics Letters*, vol. 77, no. 23, 2000.

[136] P.-H.Lai, R.-C.Liu, S.-I. Fu, Y.-Y. Tsai, C.-W.Hung, T.-P.Chen, and W.-C.Liu, "Effect of formal passivations on temperature-dependent characteristics of high electron mobility transistors," *Journal of The Electrochemical Society*, vol. 154, no. 3, 2007.

[137] H.H.Lee, R.J.Racicot, and S.H.Lee, "Surface passivation of gaas," *Applied Physics Letters*, vol. 54, no. 8, 1989.

[138] D.B.Suyatin, C.Thelander, M.T.Bjork, I.Maximov, and L.Samuelson, "Sulfur passivation for ohmic contact formation to inas nanowires," *Nanotechnology*, vol. 18, no. 105307, 2007.

[139] T.B.Hoang, L.V.Titova, H.E.Jackson, L.M.Smith, J.M.Yarrison-Rice, Y.Kim, J.Joyce, and C.Jagadish, "Imaging and optical properties of single core-shell gaas-algaas nanowires," in *IEEE-Nano 2006*, 2006.

[140] S.Perera, M.A.Fickenscher, H.E.Jackson, L.M.Smith, J.M.Yarrison-Rice, H.J.Joyce, Q.Gao, H.H.Tan, C.Jagadish, X.Zhang, and J.Zou, "Nearly intrinisic exciton lifetimes in single twin-free gaas/algaas core-shell nanowire heterostructures," *Applied Physics Letters*, vol. 93, no. 053110, 2008.

[141] N.Skold, L.S.Karlsson, M.W.Larsson, M.-E.Pistol, W.Seifert, J.Tragardh, and L.Samuelson, "Growth and optical properties of strained gaas-gaxin1-xp core-shell nanowires," *Nano Letters*, vol. 5, no. 10, pp. 1943–1947, 2005.

[142] J.Caram, C.Sandoval, M.Tirado, D.Comedi, J.Czaban, D.A.Thompson, and R.R.LaPierre, "Electrical characteristics of core-shell p-n gaas nanowire structures with te as the n-dopant," *Nanotechnology*, vol. 21, no. 134007, 2010.

[143] P.Prete, F.Marzo, P.Paiano, N.Lovergine, G.Salviati, L.Lazzarini, and T.Sekiguchi, "Luminescence of gaas/algaas core-shell nanowires grown by movpe using tertiarybutylarsine," *Journal of Crystal Growth*, vol. 310, 2008.

[144] Y.Dong, B.Tian, T.J.Kempa, and C.M.Lieber, "Coaxial group iii-nitride nanowire photovoltaics," *Nano Letters*, vol. 9, no. 5, pp. 2183–2187, 2009.

[145] H.Pettersson, J.Tragardh, A.I.Persson, L.Landin, D.Hessman, and L.Samuelson, "Infrared photodetectors in heterostructure nanowires," *Nano Letters*, vol. 6, no. 2, pp. 229–232, 2006.

[146] M.J.Biercuk, D.J.Monsma, C.M.Marcus, J.S.Becker, and R.G.Gordon, "Low-temperature atomic-layer-deposition lift-off method for microelectronic and nanoelectronic applications," *Applied Physics Letters*, vol. 83, no. 12, 2003.

[147] Y.Xuan, H.-C.Lin, and P.D.Ye, "Simplified surface preparation for gaas passivation using atomic layer-deposited high-k dielectrics," *IEEE Transactions on Electron Devices*, vol. 54, no. 8, 2007.

[148] X.Zhou, A.Dayeh, D.Wang, and E.T.Yu, "Analysis of local carrier modulation in inas semiconductor nanowire transistors," *Journal of Vacuum Science and Technology B*, vol. 25, no. 4, 2007.

[149] E.Koren, Y.Rosenwaks, J.E.Allen, E.R.Hemesath, and L.J.Lauhoh, "Nonuniform doping distribution along silicon nanowires measured by kelvin probe force microscopy and scanning photocurrent microscopy," *Applied Physics Letters*, vol. 95, no. 092105, 2009.

[150] A.Bachtold, M.S.Fuhrer, S.Plyasunov, M.Forero, E.H.Anderson, A.Zettl, and P.L.McEuen, "Scanned probe microscopy of electronics transport in carbon nanotubes," *Physical Review Letters*, vol. 84, no. 26, 2000.

[151] Y.-C.Tseng and J.Bokor, "Characterization of the junction capacitance of metal-semiconductor carbon nanotube schottky contacts," *Applied Physics Letters*, vol. 96, no. 013103, 2010.